On the study of volcanic explosions using thermal IR and visible image

Freddy Vasconez Alban

UNIVERSITE CLERMONT-AUVERGNE

Collegium des Sciences Fondamentales

ECOLE DOCTORALE DES SCIENCES FONDAMENTALES

Thèse de doctorat

Présentée en vue de l'obtention du grade de

DOCTEUR D'UNIVERSITE

Spécialité : Terre Solide : géodynamique des enveloppes supérieures / paléobiologie

par

Freddy VASCONEZ ALBAN

Titulaire du Master Sciences et Technologie, Mention Sciences de l'Univers, Environnement, Écologie
Spécialité Géosciences

On the study of volcanic explosions using thermal IR and visible image

Soutenu publiquement le 09 juin 2023 devant un jury composé de :

Prof. Silvana Hidalgo	IGEPN, Escuela Politécnica Nacional	Présidente du Jury
Dr. Letizia Spampinato	Istituto Nazionale di Geofisica e Vulcanologia	Rapporteur
Dr. Talfan Barnie	Icelandic Meteorological Office	Rapporteur
Dr. Karim Kelfoun	LMV, Université Clermont Auvergne	Examinateur
Prof. Andrew Harris	LMV, Université Clermont Auvergne	Directeur de thèse
Prof. Yves Moussallam	LDEO, Columbia University	Co-directeur de thèse

« I vulcani sono la più grande scuola
di Fisica del Gobo ».

L. Pilla.

[From Mercalli G., 1907]

Acknowledgements

I acknowledge support from the Region Auvergne Rhone Alpes through its call for projects Pack Ambition Recherche 2018 (project OROVOLC, PI: Y.M.). I also want to express my gratitude to Escuela Politécnica Nacional, my alma mater, and the Institut de Recherche pour le Développement, France (IRD, Ecuador office), with special mention to Jean-Luc Le Pennec and Pablo Samaniego for their collaboration and support for the installation of the instruments. Fieldwork for the research in second chapter was conducted as part of the "Trail by Fire" expedition (PI: Y.M.) supported by the Royal Geographical Society (with the Institute of British Geographers) through the Land Rover Bursary; the Deep Carbon Observatory DECADE Initiative; Ocean Optics; Crowcon; Air Liquide; Thermo Fisher Scientific; Cactus Outdoor; Turbo Ace and Team Black Sheep. Thanks to the administrative staff of LMV, specially to Nathaly El Aydi for her patience and efficiency in all administrative formalities.

I am grateful for the constructive feedback provided by Sylvie Vergniolle, the Associate Editor of the topical collection "Open Vents" of Bulletin of Volcanology, and the anonymous reviewers of the manuscripts corresponding to chapters one and two, which undoubtedly improved the quality of the papers. This work is part of an Ecuadorian-French cooperation programme carried out between the IGEPN and the IRD through a "Laboratoire Mixte International" program entitled "Séismes et Volcans dans les Andes du Nord". Part of this work is also a contribution to Laboratory of excellence *ClerVolc*.

I would like to extend my heartfelt thanks to all the members of the jury for accepting the responsibility of reviewing and discussing this work. Your commitment to the true essence of science and your valuable contributions have greatly enhanced the quality of this report.

A special appreciation goes to my advisors, **Yves Moussallam**, **Andrew Harris**, **Philipson Bani** and **Jean-Luc Le Pennec**. I am immensely grateful not only for your technical and scientific guidance, but also for the enormous amount of patience, trust and energy you have invested in working with me. Your dedication and unwavering support have been invaluable.

Yves, none of this would have been possible without your genius. Your intelligence, optimism, discipline, and confidence are truly inspiring: you are a role model for me. I deeply appreciate everything you have done for me, especially your advice, your questions and your sense of humour. I admire you greatly and look forward to working with you on future projects.

Silvana, haría falta un libro completo para expresar solo una parte de mi agradecimiento por todo lo que me has aportado. Gracias por todas las acciones y comunicación que permitió concretar este proyecto (y todos los demás). Gracias por la confianza, las explicaciones, los cuestionamientos, la curiosidad… en fin, ¡gracias por estar siempre!

Quiero expresar mi agradecimiento a todo el personal del IGEPN. Además, a **Pablo Samaniego, Jean Battaglia y Benjamin Bernard**, quienes siempre han brindado su apoyo y optimismo en las diferentes etapas de este proyecto. Sus comentarios han sido enormes aportes que han mantenido en movimiento los engranajes de la curiosidad.

Many thanks to all my LMV colleagues, especially **Guillaume**, **Roxane**, **Paul**, **Masa** and **Sophie**, who provided a lot of interesting information and shared pleasant moments of laughter and discussion. Special thanks to **Oryaëlle** for reminding me the important details of life in this world, and to **Taidy** ¡¿qué sería de la vida sin risa?!

A **Joselito Amaguay** y **Rosa Alulema** les debo un enorme agradecimiento porque han mantenido abiertas las puertas de la Hostería Reventador y siempre están dispuestos a dar una mano sin importar la tarea o el requerimiento que fuera.

Gracias, **Diego**, por las conversaciones técnicas y personales, por tu sinceridad y realismo (aunque no fue suficiente para llegar a Catania). También quiero agradecer al "Presea Team" en sus diferentes versiones (incluyendo la mafia ecuatoriana): **Antonio**, **Imane** (Emmy), **Anshika**, **Cynthia**, **Henry**, **Marco**, **Evelyn**, **Mike** y **Nicole**, gracias por todas las risas, comidas, bailes y bonitos recuerdos que hicieron de Clermont Ferrand nuestro hogar. **Yuly** y **Jorge**, gracias por las conversaciones, la confianza y todas las experiencias compartidas (incluyendo los virus).

A todos los que estuvieron pendientes desde lejos: a la familia en Ecuador y en España. Gracias a mis padres, **Byron** y **Esperanza**, ustedes son la inspiración y el ejemplo. **Carlos**, **David** y **Javier** (Dennis), les siento como una extensión de mí mismo; gracias por toda su ayuda, por los viajes al Reventador, las sugerencias y el enorme esfuerzo y entusiasmo con el que cuidaron del VIGIA.

Evidentemente, no hice este camino solo. **Luciana**, tú has sido la persona más importante y siempre estuviste a mi lado, aún antes del inicio oficial. Te agradezco infinitamente por los hermosos momentos, las experiencias, por todo el amor y por celebrar conmigo las alegrías, descubrir cosas, soportar los momentos de cansancio y estrés… en otras palabras, gracias por compartir esta etapa y complementar mi vida día a día.

Abstract

This work focuses on the characteristics and dynamics of Strombolian and Vulcanian explosions occurring at the Reventador volcano, using thermal and visible images of the explosions.

The first part of this work describes the instrument developed to monitor and record volcanic explosions. The instrument is called VIGIA and it is installed ~7 km away from the active crater of the Reventador volcano. VIGIA's features include volcano detection, event triggering, automatic sending of periodic reports, among others.

In the second part, the volcanic explosions are characterised on the basis of their thermal signal, which is then compared with the corresponding seismic and SO_2 flux signals. The aim of this section is to describe the short-term explosive activity of Reventador volcano. The results show that, in February 2017, the activity of the volcano presented four phases that repeated twice, including the change of eruptive style in an observation period of about two hours.

Finally, the dynamics of the eruptive plumes is studied in a group of 80 explosions. A typical explosion from the Reventador volcano is analysed in detail, and it is found that the main explosions are a sequence of secondary bursts that occur in different parts of the vent or in separate vents. This sequence of secondary bursts can provide information about the structure of the vent. In addition, we find some dependence relationships of dynamic parameters, such as the initial temperature of the material in the explosion compared to the height at which the plume entered the buoyancy regime.

Résumé

Ce travail se concentre sur les caractéristiques et la dynamique des explosions Stromboliennes et Vulcaniennes qui se produisent sur le volcan Reventador (Équateur), en utilisant l'analyse d'images thermiques et visibles des explosions.

La première partie de ce travail comprend la description de l'instrumentation développée pour la surveillance et l'enregistrement des explosions volcaniques. Il s'agit de VIGIA, un instrument installé à environ 7 km du cratère actif du volcan Reventador. Les caractéristiques de VIGIA comprennent la reconnaissance du volcan, l'enregistrement des événements pour déclenchement, la création et l'envoi de rapports périodiques automatiques, entre autres.

Dans la deuxième partie, les explosions volcaniques sont caractérisées sur la base de leur signal thermique, qui est ensuite comparé aux signaux sismiques et de flux de SO_2 correspondants. L'objectif de cette section est de décrire l'activité explosive à court terme du volcan Reventador. Les résultats montrent qu'en février 2017, l'activité du volcan a présenté quatre phases qui ont été répétées deux fois, y compris le changement de style éruptif dans une période d'observation d'environ deux heures.

Finalement, nous étudions la dynamique des panaches éruptifs dans un groupe de 80 explosions stromboliennes et volcaniques. Une explosion typique du volcan Reventador est analysée en détail et nous constatons que les explosions sont une séquence d'explosions secondaires se produisant dans différentes parties de l'évent ou dans des évents séparés. Cette séquence d'explosions secondaires peut fournir des informations importantes sur la structure de l'évent. En outre, certaines relations entre les paramètres de la dynamique du panache ont été trouvées. Par exemple, la température maximale du panache comparée à la hauteur à laquelle le panache atteint le régime de flottabilité.

Resumen

El presente trabajo se enfoca en las características y la dinámica de las explosiones estrombolianas y vulcanianas que se producen en el volcán Reventador (Ecuador), usando análisis de imagen térmica y visible de las explosiones.

La primera parte de este trabajo incluye la descripción de la instrumentación desarrollada para la vigilancia y registro de las explosiones volcánicas. Se trata de VIGIA, un instrumento instalado a unos 7 km del cráter activo del volcán Reventador. Las características de VIGIA incluyen el reconocimiento del volcán, la grabación de eventos por disparo, la creación y envío de reportes periódicos automáticos, entre otras.

En la segunda parte, las explosiones volcánicas son caracterizadas en base a su señal térmica, la que es comparada con las correspondientes señales sísmicas y de flujo de SO_2. El objetivo de esta sección es describir la actividad explosiva del volcán Reventador en el corto plazo. Los resultados muestran que, en febrero de 2017, la actividad del volcán presentó cuatro fases que se repitieron dos veces, incluyendo el cambio de estilo eruptivo en un periodo de observación cercano a dos horas.

Finalmente, estudiamos la dinámica de las plumas eruptivas en un grupo de 80 explosiones estrombolianas y vulcanianas. Una explosión típica del volcán Reventador se analiza en detalle encontrando que las explosiones son una secuencia de explosiones secundarias ocurriendo en distintas partes del vento o en ventos separados. Esta secuencia de explosiones secundarias puede aportar información importante acerca de la estructura del vento. Adicionalmente, se encontraron algunas relaciones entre los parámetros de la dinámica de las plumas. Por ejemplo, la temperatura máxima de la pluma comparada con la altura a la que la pluma alcanza el régimen de flotación.

Table of Contents

General introduction

Motivation and context

0.1 Explosive activity

Volcanic explosions are widely recognized as the most dangerous of all volcanic processes, since they represent large amounts of energy released in short periods of time. They produce a series of phenomena, including the generation of mechanical and acoustic waves, the expulsion of hot material as a jet, and the ascent of a column composed of gas and ash (e.g., Mercalli 1907; Self et al. 1979; Clarke et al. 2015). The classification of volcanic eruptions based on their power exhibits variations among different authors, resulting in conventional names that may differ slightly. Nevertheless, a commonly encountered categorization includes ultra-plinian eruptions denoting the highest level of intensity, followed by Plinian, Vulcanian, Strombolian, and finally, Hawaiian eruptions represent the lower end of the scale (e.g., Newhall and Self 1982). The consequences of volcanic eruptions also tend to align, to some extent, with this classification. Ultra-plinian eruptions, with their immense power, can have global impacts, affecting vast regions beyond the immediate vicinity of the volcano. On the other hand, Vulcanian and Strombolian eruptions typically have more localized impacts, affecting specific areas near the volcano. Understanding and discerning these classifications are essential for assessing the potential hazards and mitigating the risks associated with volcanic activity.

Strombolian explosions are intermittent events involving relatively low masses of pyroclastic material compared to the mass of gas. They are associated with low-viscosity magmas such as basaltic to basaltic andesite. Strombolian explosions produce the expulsion of ballistics, which may be composed by semi-molten lava chunks, or ash plumes reaching heights of the order of hundreds of metres to a few kilometres (e.g., Fagents et al. 2009; Ishii et al. 2019; Calvari et al. 2021). The generation of such explosions has been explained by the combination of two models. The first model proposes the formation of a sort of foam in the roof of a volcanic chamber that collapse into a gas slug that rises through a relatively narrow conduit and explodes upon reaching the surface (Jaupart and Vergniolle 1988; Parfitt and Wilson 2008). The second model considers the growth of gas bubbles that originally ascended with a rising magma column. Depending on the rate of ascent and the viscosity of the magma, the bubbles may interact with each other to form a slug that will burst at the surface (Wilson 1980; Parfitt and Wilson 2008). Patrick et al. (2007) examined in detail a group of Strombolian explosions at the Stromboli volcano using thermal imaging. They found two types of explosions, which they called Type 1 (ballistic-dominated) and Type 2 (ash-dominated). Previously, Chouet et al. (1974) had studied the dynamics of ballistics using long exposure pictures of Type 1 explosions, and Blackburn et al. (1976) had described the dynamics of the ash plumes produced during Type 2 explosions using analogic video records (Patrick et al. 2007).

On the other hand, based on his observations, Mercalli (1907) determined that the explosions on the island of Vulcano, in Italy, are essentially different from Strombolian and Plinian explosions (e.g., Formenti et al. 2003). He designated this type of explosions as *Vulcanian*. Vulcanian explosions are short-lived but generally more energetic than Strombolian involving the ejection of large ballistics and, commonly, pressure waves of variable intensities. They produce a dark, mushroom-shaped column that can rise several kilometres above the crater level and usually include an important portion of non-juvenile material (Self et al. 1979; Formenti et al. 2003; Clarke et al. 2015). The ash column often collapses into pyroclastic density currents. The mechanism by which Vulcanian explosions occur consists of the sudden decompression of gas trapped under a rock cap or dome. The failure of the barrier that kept the gas at overpressure produces a decompression wave that reaches the shallowest magma, favouring the exsolution of gas, with which the expelled material can reach velocities of up to 400 m s-1 (e.g., Woods 1995a; Fagents et al. 2009; Clarke et al. 2015).

0.2 Thermal Imaging

Thermal imaging relies on the utilisation of electromagnetic radiation emitted by objects, which is directly influenced by their temperature. Throughout history, several authors have made significant contributions to the study of electromagnetic radiation. Among them, we can name Isaac Newton, who decomposed a ray of white light in its monochromatic components using a prism in 1666 (Newton 1672); William Hershel characterised infrared radiation calling it “heat rays” in 1800 (Herschel 1800), followed by Johann Ritter, who tried to discover the opposite effect to the other side of the visible spectrum, finally finding “chemical rays” which afterwards would be called ultraviolet radiation (e.g., Davidson 2014); and James Maxwell, who formalized the electromagnetic theory with his set of equations in the early 1860s (Maxwell 1865).

To address the issue of electromagnetic radiation emitted by objects, Kirchhoff (1860) proposed the concept of a black body as a perfect radiator, leaving the question of power distribution with respect to radiation wavelength unanswered. Max Planck resolved this problem by enunciating his law of black body radiation (e.g., Planck and Masius 1914), which asserts that radiant exitance depends on the body's temperature and the wavelength of the radiation (Figure 1), thus

$$M(\lambda, T) = \frac{2\pi hc^2}{\lambda^5 \left(e^{\frac{hc}{\lambda kT}} - 1 \right)} \qquad (0.1)$$

Where[1] M is the spectral radiant exitance in [W m^{-2} m^{-1}]

h is Plank's constant [6.626 x 10^{-34} J s]

c is the speed of light [2.9979 x 10^{8} m s^{-1}]

k is the Boltzmann constant [1.38 x 10^{-23} J K^{-1}]

T is the absolute temperature of the body [K]

λ is the wavelength of radiation [m]

Additionally, Wilhelm Wien recognized that the wavelength at which a black body emits the highest amount of energy varies inversely with the body's temperature, as reflected in his displacement law (Figure 1).

$$\lambda_m = \frac{A}{T} \qquad (0.2)$$

Where A is Wien's constant [2898 μm K]

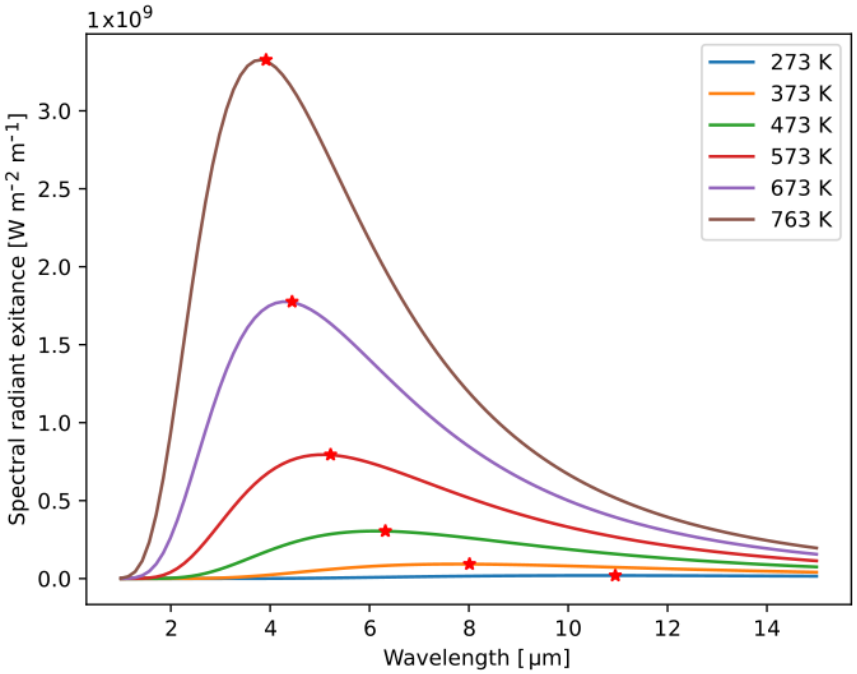

Figure 1 Plank curves were computed using equation 0.1 for temperatures ranging from 0°C to 500°C. The red stars indicate the wavelengths at which maximum power radiation occurs for each temperature, in accordance with Wien's displacement law.

Moreover, the contribution of Josef Stephan, alongside Ludwig Boltzmann, resulted in the formulation of the law that bears their names, establishing a relationship between the total radiation (across all wavelengths) emitted by a black body and its temperature.

[1] The nomencalture used in this section is the same used by Harris (2013)

$$M_{rad} = \sigma T^4 \qquad (0.3)$$

In which M_{rad} is the radiant flux density [W m^{-2}], resulting from the integration of the spectral radiant exitance over the entire spectrum.

These results provide the theoretical basis for using the radiation emitted by objects to determine their temperature quantitatively. The value of the temperature reported in this stage is called *brightness temperature*. Some considerations are needed to convert brightness temperature into real temperature.

0.2.1 Graybodies and emissivity

The description of radiation discussed so far is based on a perfect radiator. However, the ideal conditions of a blackbody are only found in few situations. In most cases, bodies emit only a fraction of the energy emitted by a blackbody. This fraction is characterised by the emissivity coefficient, $\varepsilon(\lambda)$. We can express the emissivity of a surface as the ratio between the spectral exitance of the surface, $M(\lambda,T)$, and that of a blackbody at the same wavelength and temperature, $M_{BB}(\lambda,T)$.

$$\varepsilon(\lambda) = \frac{M(\lambda,T)}{M_{BB}(\lambda,T)} \qquad (0.4)$$

Note that the emissivity is a function of the wavelength, in other words, an object can behave as blackbody in some portion of the spectrum and emit low radiation in other part. This general variation of the emissivity with wavelength is a characteristic of *selective radiators*. In the case that the emissivity is less than 1, but the same for all the wavelengths then it is a *graybody*.

In the case of a blackbody, all the radiation received (α) is reemitted. In the case of real objects, a fraction ρ of the energy received is reflected and a fraction τ is transmitted. Respecting the conservation of the energy, it can be expressed that

$$\varepsilon(\lambda) + \rho(\lambda) + \tau(\lambda) = 1 \qquad (0.5)$$

Where ρ is the reflectance and τ is the transmittance; both depend on the wavelength. For an opaque object, equation 0.5 reduces to:

$$\varepsilon(\lambda) + \rho(\lambda) = 1 \qquad (0.6)$$

When measuring radiation from objects on the Earth's surface, it is important to consider that the atmosphere is not opaque. The reflectance and transmittance of the atmosphere depend on factors such as aerosol content, relative humidity, among others.

0.3 Reventador volcano

The Reventador volcano is a stratovolcano located in the limit between the Andean cordillera and the Amazonian basin, around 100 km to the east of Quito, in Ecuador (Figure 2a). Its currently active cone was built within the amphitheatre formed by the collapse of the ancient edifice ~20 ka (INECEL 1987) that is 4 km wide (north-south) and 6 km long (northwest – southeast) and open to the southeast (Figure 2b). More than 20 eruptions were identified since 1541 (Siebert et al. 2011; Naranjo et al. 2016), of which seven occurred in the twentieth century. The first and the longest episode of the twentieth century took place from 1898 to 1912, and subsequent eruptive episodes had variable durations of up to 3 years, each separated by periods of around 12 years of quiescence. The last eruptive episode of the twentieth century ended in 1976. All of these eruptive episodes were “moderate” to “moderate-large” in scale (i.e., VEI 2-3), with Strombolian to Vulcanian eruptive styles (cf. Newhall and Self 1982), and produced blocky lava flows, small-volume pyroclastic and debris flows, and ash fallout (Hall et al. 2004; Samaniego et al. 2008).

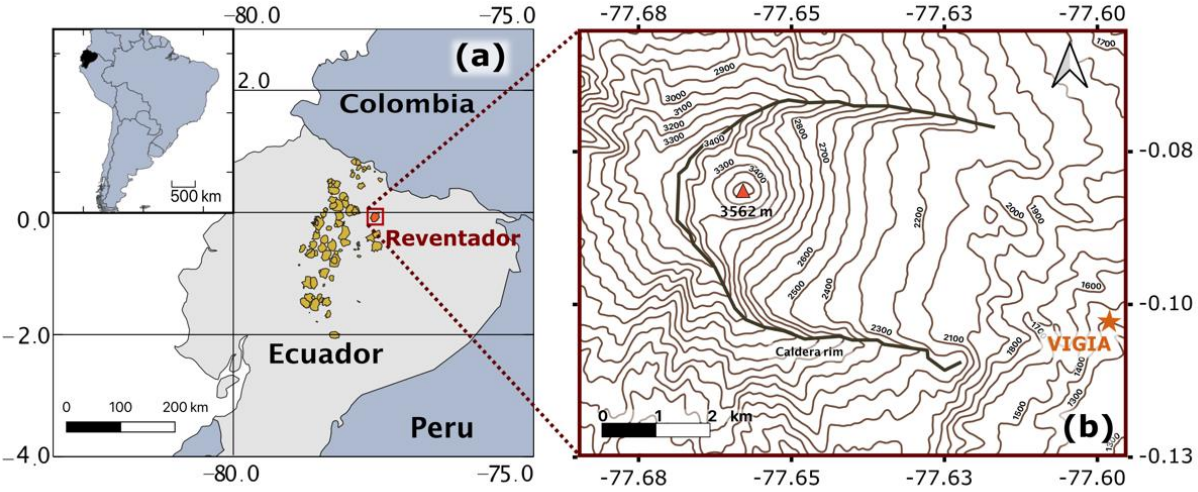

Figure 2 (a) Reventador volcano is located in the limit between the Andean cordillera and the Amazon basin in Ecuador. (**b**) The current active cone is located inside a 4 km wide U-shaped debris avalanche scar. VIGIA is installed within the property of Hostería Reventador, 7 km eastward from the active cone.

On 3 November 2002, after 26 years of quiescence and with minimal warning indicators, the Reventador volcano abruptly awakened with a VEI4 explosion (cf. Newhall and Self 1982). This event resulted in the destruction of the summit, which stood at an elevation of 3650 m at the time (Hall et al. 2004; Almeida et al. 2019), leaving deep notches on the northern and southern margins of the summit. Moreover, it generated a towering eruptive column reaching a height of 17 km, accompanied by the formation of at least five pyroclastic flows that cascaded down towards the Coca River, located 8 km eastward. The impact of these

pyroclastic flows included the destruction of two oil pipelines and the main road leading to the eastern side of the country. The lower section of the ash cloud reached Quito, Ecuador's capital city, as well as the Interandean Valley, while the upper portion of the ash cloud travelled to the east reaching southern Colombia and north-western Brazil (Hall et al. 2004). As a result of the intense ash fall on November 3, Quito was compelled to close its international airport for eight consecutive days to facilitate the necessary clean-up operations that required removal of ash layer, ranging 1-2 mm in thickness (Hall et al. 2004).

During the first year after the paroxysmal eruption, a lava flow poured out from the notch left in the southern part of the crater and another lava flow from a lateral vent opened in the south-eastern cone flank (Hall et al. 2004; Samaniego et al. 2008; Naranjo et al. 2016). Afterwards, a period of low activity, mainly consisting in gas emissions, that lasted around one year was followed by new lava flows emplaced in 2004, and these followed by alternating periods of effusive and mildly explosive activity characterized by Strombolian activity and short-lived Vulcanian explosions (Lees et al. 2008; Ortiz et al. 2020). By 2015, the volcanic cone was similarly shaped as it was before 2002 (Ortiz et al. 2020). Almeida et al. (2019) documented a series of morphologic changes in the upper part of the cone occurred between 2016 and 2018, including the existence of two active vents in January 2016, a lateral eruption in June 2017, and a partial summit collapse in April 2018. By February 2017, five effusive episodes had been identified by Naranjo et al. (2016) and Arnold et al. (2017) showing a variable discharge rate within each of the effusive periods, with a general decreasing trend from one period to the next.

Ortiz et al. (2020) analysed the records from an infrasound array located 124 km away from the crater of the Reventador volcano, in the period between 2006 to 2013, finding 11375 impulsive transient signals that can be associated to explosive events. In this period, the average was 5 detections per day, showing a maximum of 147 detections in May 2006 (Ortiz et al. 2020). These readings are considered to be underestimates due to the large distance between the instruments and the volcano. From 2012 through 2020, and continuing during effusive episodes, a variable number of explosions (up to 50 per day) were recorded by the local monitoring network operated by the Instituto Geofísico of Escuela Politécnica Nacional (IGEPN) (cf. Ramon et al. 2021). These transient explosions typically produced ash columns of variable ash content and height, ascending up to 2 km above the summit crater (e.g., Instituto Geofísico 2010, 2018, 2019). Similar activity has been observed at other open-vent andesitic through dacitic systems as, for example Sangay in Ecuador (Johnson and Lees 2000), Karymsky in Kamchatka (Johnson and Lees 2000) and Santiaguito in Guatemala (Johnson et al. 2008; Sahetapy-Engel et al. 2008; Sahetapy-Engel and Harris 2009). Models proposed to explain the generation of such explosions include accumulation of gas under a near-surface

structure, i.e., a plug or a viscoelastic lava dome acting as pressure valve, that is released by the mechanical failure of the blocking structure (Johnson and Lees 2000; Johnson et al. 2008). A second model explains ash eruptions at such open-vent system as being generated by slip events to cause shear-induced magma fragmentation at the conduit boundaries around the ascending dacite plug (Gonnermann and Manga 2003; Bluth and Rose 2004; Sahetapy-Engel et al. 2008).

0.4 Structure and contents

This study aims to understand the mechanisms and dynamics underlying Strombolian and Vulcanian explosions. Specifically, it focuses on observing volcanic explosions at Reventador volcano in Ecuador, using both infrared and visible-range images. The research employs computer vision and various other techniques to analyse and describe the dynamics of the resulting eruptive columns. The document comprises three chapters. Chapter one provides details of the observation methods and instrumentation, while Chapter two presents a description of explosive events and their immediate effects. Chapter three explores the dynamics of the eruptive column. It is important to note that each chapter has been written with the intention of being published in scientific journals. Therefore, certain pieces of information may appear repetitious, and formatting may not be consistent across the chapters.

Chapter one presents a description of the instrumentation and methods employed throughout this study. The instrument, named VIGIA (Visible and Infrared Ground-based Imagery Analyser), was designed for the permanent and real-time observation of volcanic explosive events in both visible and thermal infrared wavelengths, the output of which can be fully synchronised with ancillary monitoring data. VIGIA follows an edge computing approach whereby information is processed on-site, and periodic reports are sent to the local observatory and the system “decides” when to acquire high-temporal resolution data so as to capture key explosive events. As a permanent installation, VIGIA enables the continuous, long-term and time-synchronised observation of volcanic activity while reducing power consumption and data volumes. This instrument was installed at the Reventador volcano and its description was published in the journal Remote Sensing. Following the publication of the paper, VIGIA underwent further advancements, with ongoing efforts aimed at its continuous improvement. It has already become an integral part of the monitoring network operated by the Instituto Geofísico of Escuela Politécnica Nacional (IGEPN), providing valuable data for monitoring tasks and offering potential for future scientific research.

In the second chapter, I have employed a combination of high temporal resolution thermal infrared imaging, seismic recordings, and DOAS-derived SO2 fluxes to investigate a specific period of Vulcanian-style activity occurring on 22-23 February 2017. Through thermal

imagery, I captured and analysed the emission and ascent dynamics of 26 plumes that manifested during the observation period, including those originating from explosive events and degassing episodes. While most explosions exhibited associated seismic signals, a few instances stood out with the absence of measurable seismic activity. Likewise, degassing episodes demonstrated minimal seismic signals. These findings suggest a sequential pattern of explosions and degassing events, which can be elucidated by changes in conduit permeability due to the rapid rheological stiffening of magma in the uppermost section of the conduit. This stiffening process reduces degassing efficiency. Consequently, periods of open vent outgassing alternate with intervals of conduit capping, resulting in system pressurization and subsequent Vulcanian explosions that re-establish conduit connectivity, enabling the resumption of outgassing processes.

Chapter three contains the study of the dynamics of the jet zone and convective zone in a series of Strombolian to Vulcanian explosions at El Reventador volcano. By analysing thermal records, I extract key parameters such as plume exit velocity, maximum temperature, ascending front velocity, and volume. Theoretical models are employed to calculate the bulk density of the plume, as well as the mass of ejected material and the gas mass fraction at the explosion's origin. Through the analysis of 80 explosions, I identify patterns in eruptive behaviour and establish correlations among various eruption parameters. Additionally, I provide a detailed review of a typical Reventador explosion, highlighting its development and characteristic features. The findings reveal that the volcanic plumes generated during these explosions are the cumulative result of sequentially generated small plumes. I also observe that the vent configuration exhibits complexity, with sections activating in a sequential manner, and that these sections may operate independently in terms of gas permeability.

Chapter One: Instrumentation and methods

VIGIA: A Thermal and Visible Imagery System to Track Volcanic Explosions

1.1 Introduction

Explosive volcanic eruptions can have damaging consequences over a wide range of scales, from the global scale, as seen in the 1991 eruption of Pinatubo in the Philippines (e.g., Newhall and Punongbayan 1995); the regional scale such as the 2010 eruption of Eyjafjallajökull in Iceland (e.g., Saltykovskii 2012); to the local scale such as the 1999–2017 Tungurahua and 2002 Reventador eruptions (e.g., Hall et al. 2004; Eychenne et al. 2012). The dynamics of volcanic explosions have been studied from two different perspectives: to constrain the parameters of the eruptive regime (e.g., Morton et al. 1956; Wilson et al. 1978; Wilson and Self 1980; Sahetapy-Engel and Harris 2009; Harris et al. 2012) and to model the dispersion of pyroclasts (e.g., Bonadonna and Phillips 2003; Costa et al. 2006; Parra et al. 2016). Describing the dynamics of volcanic explosive eruptions at the local level is key for the volcanic observatories' aim of estimating the associated risk. Video cameras have been used for several decades to monitor and study explosive eruptions (e.g., Wilson and Self 1980; Formenti et al. 2003); more recently, the use of infrared thermal imaging has been added as remote and ground-based surveillance (e.g., Ramsey and Harris 2013). Airborne- and ground-based thermal infrared imagery has proved to be an efficient and powerful tool to monitor volcanic activity. It has been used to observe superficial changes around volcanic craters (e.g., Carter et al. 2007; Calvari et al. 2016; Mothes et al. 2017), locate and track lava flows (e.g., James et al. 2006; Kelfoun and Vallejo Vargas 2015; Di Traglia et al. 2018), identify pyroclastic density current deposits (e.g., Hall et al. 2015; Calvari et al. 2020), estimate lava effusion rates (e.g., Harris et al. 2003, 2007), study lava domes' growth and collapse (Kelfoun et al. 2021), monitor lava lakes (e.g., Oppenheimer and Yirgu 2002; Patrick et al. 2016), characterise explosive eruptions (e.g., Patrick et al. 2007; Calvari et al. 2021) and describe plume shape and dynamics (e.g., Patrick et al. 2005; Lopez et al. 2015; Wood et al. 2019). Most of these results have been obtained during measurement campaigns, either with fixed instruments or mounted on manned or autonomous aircraft (including unmanned aerial vehicles, UAVs). Thermal and visual video observations of eruptive phenomena, and their correlation with data from deformation, acoustic and seismic networks, however, are often limited by technical constraints. Limitations include time synchronisation, data volumes and power consumption. Although these constraints can all be addressed (e.g., Yokoo 2009; Patrick et al. 2014), there are still few observatories that use permanent stations for long-term studies.

In this work, we present VIGIA, an instrument based on thermal and visible imagery intended to serve as a permanent observation station that follows an edge computing approach whereby information is processed on site. We use the Reventador volcano in Ecuador (Figure 1b) as a case study to prove the capabilities of the instrument, which decides when to acquire high-temporal resolution data so as to capture key explosive eruptions and sends periodic

reports to the Instituto Geofísico of the Escuela Politécnica Nacional (IGEPN), the local observatory.

1.2 Brief, Non-Exhaustive, History of Permanently Deployed Instrumentation for Thermography

One of the earliest remote temperature measurements in the study of volcanoes (see Figure 2) was documented by Thomas A. Jaggar in his investigation at Kilauea (Hawaii, USA; Jaggar 1917b). Although Jaggar used Seger cones, commonly employed in pottery, to determine the temperature gradient in the uppermost 15 m of the Halema'uma'u lava lake (Hawaii, USA; Jaggar 1917a), he also mentioned that Daly, in 1909, and Day and Shepherd, in 1912, used optical pyrometers to measure the temperature of active lava fountains in the same lava lake. Several authors followed this schema and carried out measurement campaigns to obtain the volcano-feature's surface temperature from several kilometres away; for example, the temperature of the dacitic dome's surface at Santiaguito volcano (Quetzaltenango, Guatemala) was measured by Zies (1941), who used an optical pyrometer calibrated in the range of 550 to 950 °C to obtain lava temperatures of 700 ± 25 °C. It was in 1967, that Zettwoog and Tazieff promoted the use of permanently installed instrumentation, deployed at Etna (Sicily, Italy), to measure vent temperatures (Zettwoog and Tazieff 1972). In the same context, in his 1971 report for UNESCO (Moxham 1971), Robert M. Moxham presented the state-of-the-art possibilities for permanent deployments, which included portable direct-reading radiometers with optional recorders, and aerial radiometric systems. The main challenges at that time were the harsh environmental conditions and equipment bulk (Harris 2013). Moxham et al. (1972) conducted an experiment in which temperature data from fumaroles at Mount Rainier (Washington, USA) were received in Washington via a satellite link. In this experiment, an insulated plywood box contained the instruments including the main power supply battery which was replenished by a solar-cell panel. The box was heated by a system connected to a wind generator. Although some of the instruments were destroyed after five weeks, the results were optimistically reported, confirming the feasibility of using satellites for the telemetry of volcanic temperatures. Another attempt to implement instrumentation to measure volcanic temperature was executed in 1978 by Brivio and Tomasoni (1980), who modified a commercial radiometer and installed it on a 2.5 m high pillar overlooking the fumarolic field at Vulcano (Aeolian Islands, Italy). The data were transmitted by a 5 km radio link back to Lipari (Aeolian Islands, Italy). Once again, environmental conditions, high salinity, humidity, wind, and rain eventually caused the system to fail after a few months.

A significant step in increasing the durability of instruments deployed in the harsh environment that often characterise volcanic landscape was achieved by Carl R. Thornber (1997), who successfully installed a remote video telemetry system (RVTS) for the surveillance

of Kilauea, transmitting visible images of the Pu'u O'o eruptive vent to the Hawaiian Volcano Observatory (HVO). Despite not having pursued temperature measurements, this RVTS was the basis for the development of the thermal monitoring system for Kilauea volcano, which was named DUCKS, designed and built in 1999 by Harris et al. (2005). The DUCKS system was a low-cost robust modular system based on thermal infrared thermometers that used radio transceivers to transmit thermal data to the HVO. The system was modified to be installed at Stromboli volcano in 2002, where its robustness was severely tested during the paroxysmal eruption of 5 April 2003. The instrument recorded good, unsaturated data during the whole eruption (Harris et al. 2008). Based on the idea of robustness, Aster et al. (2004) installed an integrated surveillance instrumental network at Mount Erebus volcano (Ross Island, Antarctica) which included dual-frequency GPS receivers, broadband seismometers, digital radiometers, video cameras and radio transceivers for data transmission. The RVTS was also the starting point for the development of volcano monitoring systems based on thermal imaging. Camcorder-style thermal cameras appeared in the market from 1995 (FLIR Systems 2004), but it took some years until they evolved to fulfil the necessary characteristics to function as parts of permanent deployed stations. In 2004, two thermal cameras were added to the existing video surveillance system at Etna volcano (Andò and Pecora 2006), allowing the implementation of real-time analysis of the images to discriminate the type of activity (between gas emission, lava effusion and absence of activity) and thus change the storing rate of the images and provide statistics of volcanic phenomena. The deployment of this system resulted in the detailed study of the 2011–2013 Etna lava fountaining episode (e.g., Calvari et al. 2011; Scollo et al. 2014). In 2006, Lodato et al. (2008) installed a thermal camera at Vulcano to monitor the fumarolic field. Delle Donne et al. (2006) used a permanently installed thermal camera to automatically evaluate the volcanic explosion rate, the magnitude of the explosions, the maximum height above the crater rim reached by the ejecta, the maximum velocity of the pyroclastic material and gas, and the distribution of the thermal activity along the active vents at Stromboli (Aeolian Islands, Italy). Many equipment features have improved over the last few years, allowing equipment to be interconnected, sampling rates to be increased and image resolution to be boosted. Another example of permanent deployment based on thermal cameras for volcanic surveillance was described by Patrick et al. (2014), who installed thermal cameras between 2010 and 2012 at Kilauea and Mauna Loa (Hawaii, USA) in order to monitor lava lakes, intracrater vents, fissure eruptions, lava flows and fumarolic activity. During the subsequent years, image processing algorithms using visible images were implemented to calculate plume heights (Scollo et al. 2014; Pailot-Bonnétat et al. 2020) and to estimate mass eruption rates (Dürig et al. 2018). In 2014, a team from Laboratoire Magmas et Volcans (LMV) and the Observatoire de Physique du Globe de Clermont Ferrand (OPGC) implemented an integral system based on thermal and visible imagery to monitor the lava dome dynamics at

the Merapi volcano (Central Java-Yogyakarta, Indonesia; Kelfoun et al. 2021). The system includes four stations, placed in pairs, so that they produce stereoscopic images that allow objects to be spatially located and their trajectories reconstructed. Each station contains a digital single lens reflex camera (DSLR), an infrared thermal camera and one or two webcams. The instrument presented in this paper is based on the central idea of the instrument developed for Merapi.

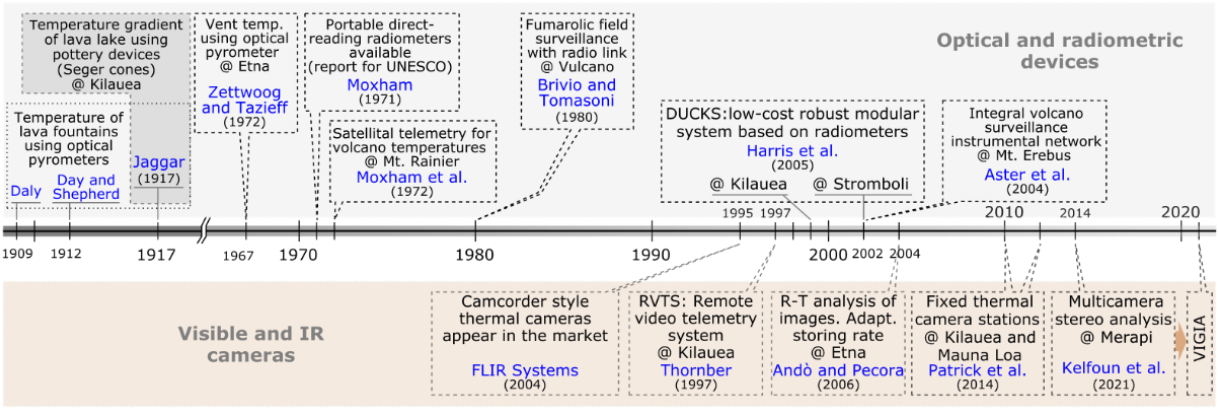

Figure 3 A brief (non-exhaustive) chronology of the evolution of permanently installed instrumentation for measuring temperature at volcanoes. Each milestone is defined by a scientific publication: the author is indicated in blue letters and the year of publication in parentheses. The pins show the installation time, some of the above systems remain operational at the time of writing (2022).

1.3 Materials and Methods

Our instrument, VIGIA (visual and infrared ground-based imagery analyser; named in honour of the Vigia network of local observers during the Tungurahua 1999–2017 eruption; Stone et al. 2014; Mothes et al. 2015), was developed to record and analyse thermal and visible images at a high sampling rate (32 images per second) during volcanic explosive eruptions. The main components of this instrument are grouped as depicted in the diagram of Figure 3a, into four groups: (1) the power supply system; (2) the computing unit, which includes the timing module, the external pressure–temperature–relative-humidity (P-T-RH) sensor, the Ethernet port and the storage drive; (3) the cameras, consisting of the thermal module and the visible module; and (4) the communications module. VIGIA was conceived to work permanently, thus the power supply and communications were designed to keep the instrument running continuously and to optimize the amount of data transmitted. The computing unit, hereinafter referred to simply as the *central computer*, is the backbone of the instrument, having the function of controlling the cameras, retrieving the images and processing them. It is based on a Raspberry Pi 4 as the hardware core running Raspberry OS (previously Raspbian) which is an operating system based on the Debian Linux distribution. Although the instrument can operate autonomously, there is also the possibility to control it

remotely. The complete set of configuration files and scripts can be found as Supplementary Material.

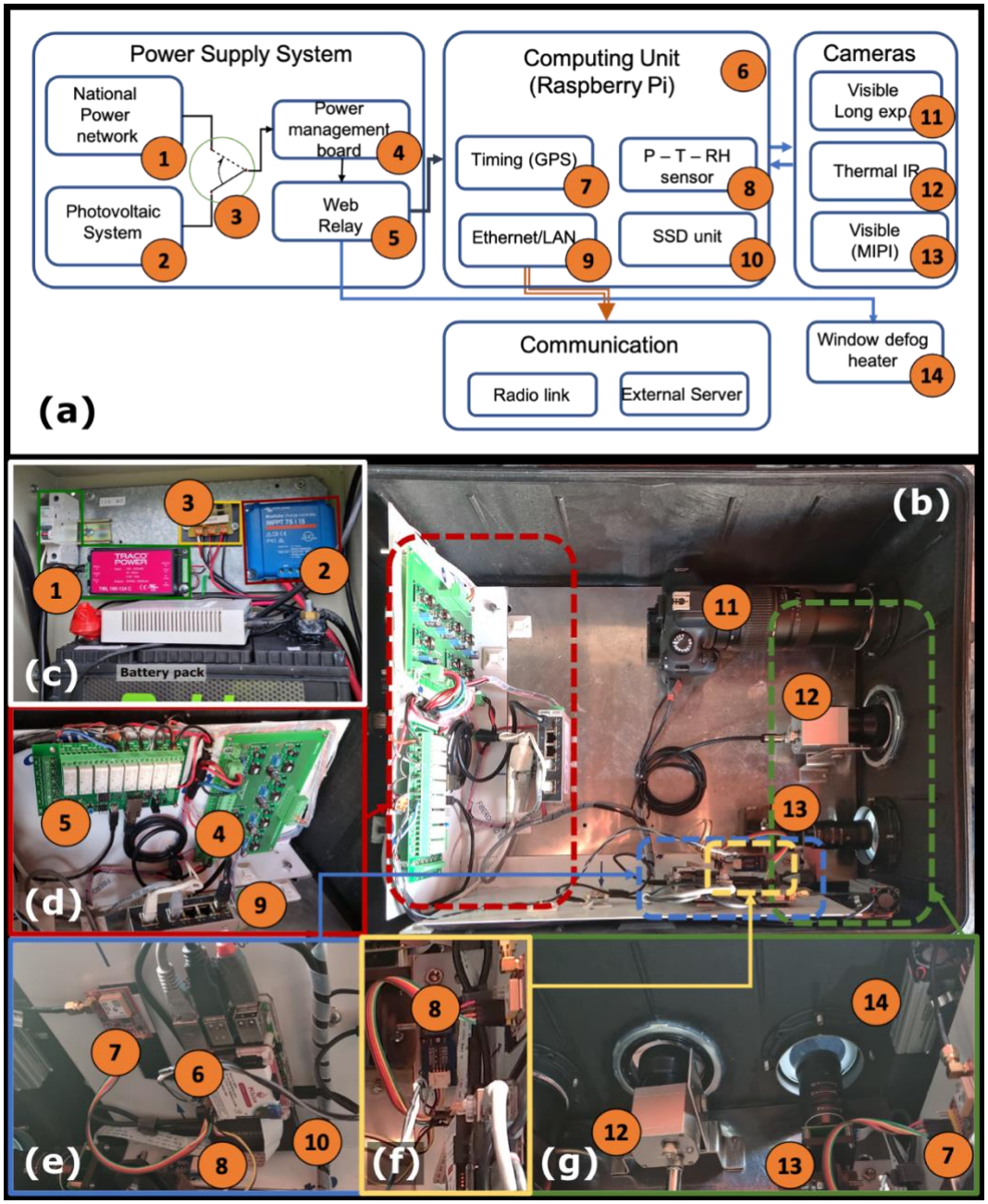

Figure 4 (**a**) Block diagram of the components of VIGIA. The physical disposition of the elements inside the case is shown in (**b**). Most of the elements composing the power system are physically placed out of the main case (**c**); those that remain inside are the power management board (4) and the web relay (5), shown in panel (**d**). Panel (**e**) contains the central computer (6) and its peripheric devices: (7) GPS module, (8) pressure–temperature–relative humidity (P-T-RH) sensor, (9) Ethernet hub and (10) solid state drive (SSD). A zoomed view of the P-T-RH sensor is displayed in panel (**f**). Panel (**g**) shows the disposition of the thermal camera (12), the visible camera (MIPI CSI) (13) and the window defogging heater (14).

1.3.1 *Power System*

VIGIA is powered by a backed-up 24 VDC power supply (Figure 3c) in which the main source is the national power grid (110 VAC-60 Hz in Ecuador, Figure 3c-1) and the backup source is a stand-alone photovoltaic power system (Figure 3c-2) consisting of two 50 W solar panels that recharge a battery bank of two 70 Ah lead-acid batteries. A diode-based circuit (Figure 3c-3) that was designed at the Division of Control Systems LRS of the Technische Universität Kaiserslautern and built at the IGEPN, allows the system to be connected to the power source with the highest voltage. Figure 4 depicts the schematics of the diode-based circuit, which uses Schottky diodes with low internal resistance and very low reverse current. In case of failure in the national power network, the photovoltaic system provides the energy necessary for the instrument to run normally and, in case the solar panels get covered or disconnected, external lead-acid batteries provide an autonomy of up to 72 h. The instrument's components receive the power they need to operate from a power management board (Figure 3d-4), designed and built at the OPGC, which ensures that the voltage delivered to each component is stable. A web relay (Figure 3d-5) controls individually the power of the central computer (Figure 3e-6), the DSLR camera (see Visual Module section below) (Figure 3b-11), the window defogging heater (Figure 3g-14) and includes the possibility to send signals remotely for a soft reboot, shutdown and a hard reboot of the central computer.

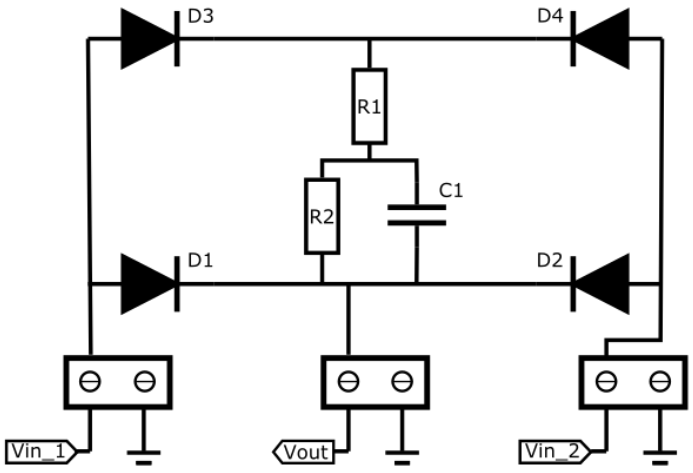

Figure 5 This diode-based circuit allows the implementation of a dual power supply system, switching between Vin_1 and Vin_2 depending on the higher voltage. It uses Schottky diodes with low dynamic resistance and very low reverse current to minimize the power transfer between the two power sources.

1.3.2 *Computer Unit*

The computer unit is responsible for data acquisition, processing and communication. It counts with a GPS module (Figure 3e-7) to ensure that all data recorded by the VIGIA is

UTC time stamped to microsecond accuracy. The GPS module used is based on the L80–39 chip, which uses a serial port for communication and needs a GPIO pin to send the pulse-per-second signal. The system synchronises its own clock with the GPS time using standard Linux utilities (gpsd, pps-tools and ntp). An external sensor (P-T-RH) (Figure 3f-8) measures ambient pressure, ambient temperature and relative humidity to check the possible influence of these parameters on the thermal data (script included within the Supplementary Material). The transmission of the data processing results takes place mainly via the Ethernet connection (Figure 3b,d-9). The communication process is described in more detail below. The raw data, as well as the processed results are stored on a solid-state drive (SSD) (Figure 3e-10). The SSD was chosen instead of a hard disk drive (HDD) because of its reliability against shock, vibration and extreme temperatures, not to mention write and read speed.

1.3.3 Thermal Module

We used an 8–14µm Optris PI 640 thermal camera (Figure 3b,g-12) to record static 640 × 480 pixel images and 32 frames-per-second (fps) video. Evocortex provides a Software Development Kit (SDK) called IRImagerDirect SDK (Evocortex) which includes the PI imager library to control the camera and the documentation. The library can be integrated into C++ programs and also in Python scripts to connect to the camera and retrieve images including metadata. VIGIA has different modes for recording thermal data, depending on the status of the volcano. If the volcano is clouded, the instrument remains in a *waiting state*, just checking periodically whether the volcano becomes clear or not (see Volcano Recognition section below). Once the volcano becomes unclouded, the crater is identifiable, then the system goes into an *acquisition state* in which it acquires periodic static thermal pictures and, by obtaining the maximum temperature within a region of interest (ROI) located just above the crater rim, it generates a thermal timeseries with the maximum temperature in the ROI at 32 samples per second (sps). The central computer applies a triggering system on the thermal timeseries to identify explosive eruptions. Every time an explosion is detected, the system records a thermal video.

For computers, a thermal image is an array of floating-point numbers (32 or 64 bits) representing the temperature of each pixel, plus an array of integers containing the metadata (time stamp, camera identifier, among other information). Optris, the thermal camera manufacturer, uses lossless compression algorithms to change the representation to 16-bit integers. We used the Python module *Numpy* to manage and store data with its conventional *.npz* extension. Each thermal file has an identifier in the name telling the type of data contained. Examples of thermal filenames are VIGIA_IR_<date>_<time>.npz for still thermal infrared picture, VIGIA_THVID_<date>_<time>.npz for thermal infrared video frames and VIGIA_METAD_<date>_<time>.npz for thermal video metadata.

1.3.4 *Visible Module*

The visible module of the VIGIA includes a 5-megapixel visible camera (Figure 3b,g-13) rendering images through the MIPI Camera Serial Interface (MIPI CSI) connection provided by the Raspberry Pi, and an 18-megapixel DSLR Canon camera (Figure 3b-11) connected using the USB port. A python script, written by the OPGC technical team, retrieves videos from the 5-megapixel camera when an explosion is triggered. The video recorded includes a five-second pre-trigger period and its length is set to 1.5 min. At night, all images and videos from the 5-megapixel camera are dark, the DSLR camera is used then in bulb mode to capture long exposure pictures rendering the volcano visible. During the daytime, the DSLR camera captures a series of 10 individual shots. Both visual cameras are triggered by the thermal module.

1.3.5 *Volcano Recognition*

Most volcanoes have their summit at least occasionally obstructed from view by cloud cover. At volcanoes such as Reventador, located in the sub-Andean region where the Amazonian Forest environment is very humid, the periods in which the volcano is clear from cloud cover can be as small as ten hours in a week. In order to optimize the amount of disk space and transmission bandwidth, VIGIA counts with an algorithm to recognize whether the volcano is clear or clouded (Figure 5). This algorithm uses the contours of the crater in good conditions (i.e., no clouds or gas in the surroundings) as a template that the computer searches for in each picture (Figure 5a). The algorithm also uses a weighted mask to enhance the importance of the flanks of the volcano over the upper rim (Figure 5b). The mask was defined based on the rapid changes of the morphology observed at the upper rim (Almeida et al. 2019). We applied a normalised 2D cross-correlation algorithm included in OpenCV API to search for the template and locate the point with the highest correlation coefficient between the image and the template. As a result of this operation, we have the normalised cross-correlation coefficient and the location of the pattern in row and column coordinates from the origin; in the particular case shown in Figure 5, from the lower left corner. We used this coefficient to discriminate if the volcano appears in the image by simply comparing it to a predefined threshold; if the volcano is clouded, the coefficient is very low, and the location is reported as the origin. We tested the volcano recognition procedure in three stages. During the first stage, we used 80 images acquired at different times of the day to adjust the threshold value above which the image is defined as clear or cloudy. In the second stage we used 780 images from different months in which the volcano appears in different locations inside the frame, showing that the result of the recognition is indifferent to changes in position caused by wind, vibrations or slight displacements of the camera. The third test was performed on a sample of 2600 images taken at different times of the day, on different days of different seasons. Each new

image obtained has a probability of success independent of the result of the previous ones. In these tests we have defined a *hit* or *success* as the coincidence between the label resulted from the recognition script and the rating that a volcanologist assigned to the image.

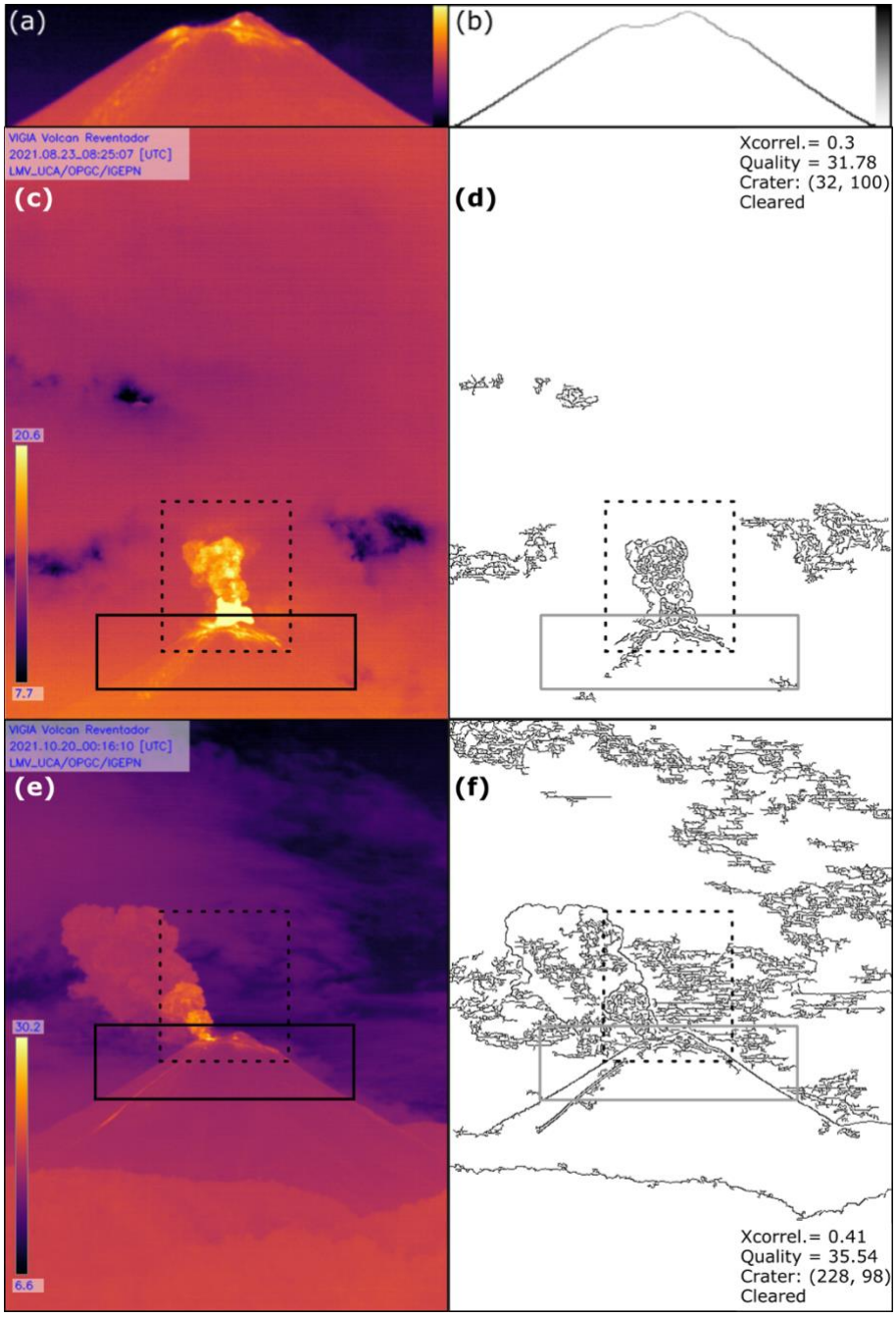

Figure 6 From a clear image of the upper cone (**a**), we extracted the outline of the volcano and used it to recognize the volcano in each captured image. Panel (**b**) shows the mask used in the normed 2D cross-correlation algorithm that determines whether or not the volcano appears in each new captured image. The colour scale in panel (**a**) represents the temperature and the grayscale in panel (**b**) represents the weight (importance) of the template pixels. In each captured image (**c,e**), the volcano recognition algorithm obtains the contours (**d,f**) and cross-correlates them with the masked template (**b**). The solid-line squares show the position of the volcano found. The normalised cross-correlation coefficient, the quality, the location of the crater as a row-column pair from the lower left corner, and the result of the recognition are

shown for an image of the Reventador volcano in August 2021 (**c,d**) and in October 2021 (**e,f**), after the camera was moved slightly downwards. The algorithm is independent of the displacement of the cone within the image. The quality factor is calculated from the number of features (contours) and the range of temperature inside the dashed-line square.

1.3.6 Communication Module

The communication module of the VIGIA instrument works on the physical communication components of the central computer, i.e., on the Ethernet interface. It is through this interface that we have access to the different components and data generated by the instrument. Several communication protocols allow us to remotely control the central system, such as SSH and VNC connections, and remote desktop applications such as AnyDesk (Weiser et al. 2021) or DWService (DWSNET OÜ 2022). Access to the graphical environment of the host computer is necessary specifically to observe the images from the cameras in real time in the process of framing and focusing during field installation.

The logic part of the communications module is in charge of delivering the results of the measurements and processing. We created a series of scripts that allow VIGIA to deliver periodic reports about the volcano (see Supplementary Material). Each time a thermal image is acquired, the volcano recognition script appends to a daily log file the date and time, the normalised cross-correlation coefficient, the image quality, the position of the volcano summit pattern, and a “Clear” or “Clouded” label. At the end of the day, a script is dedicated to obtaining statistical data from the log file; more specifically the portion of the day observed, the portion of that period when the volcano was unclouded, and the time when the volcano was last seen to be clear. These data are included in a report together with the thermal image with the best quality factor of the day and VIGIA distributes it using a telegram bot.

1.4 Results

We deployed the instrument and installed it as a permanent station at Reventador volcano, Ecuador. All the code scripts are available at https://github.com/fvasconez/VIGIA.git (accessed on 10 February 2022). Our instrument is located 7 km away from the active cone, within the property of the Hostería Reventador. It has been regularly recording data since August 2021. Figure 6 show examples of still images, in infrared and visible spectra, during the beginning (Figure 6a) and the second pulse (Figure 6b) of an explosion; it also shows a false event triggered by a simple-threshold triggering algorithm.

In the first phase, we setup VIGIA to record still thermal images every five minutes. We used these images to define the threshold that allows the instrument to discriminate whether the volcano appears in the image or not. In the second phase, the trigger frequency was increased to one shot every two minutes. During this phase, we were able to experiment with

the impact of noise on the thermal images on the recognition procedure, and to adjust the parameters of the denoising procedure to increase the success rate of volcano recognition. In the third phase, the image capture frequency was dynamically adjusted to the visibility conditions, capturing one image per minute under clear conditions and one image every five minutes under cloudy conditions.

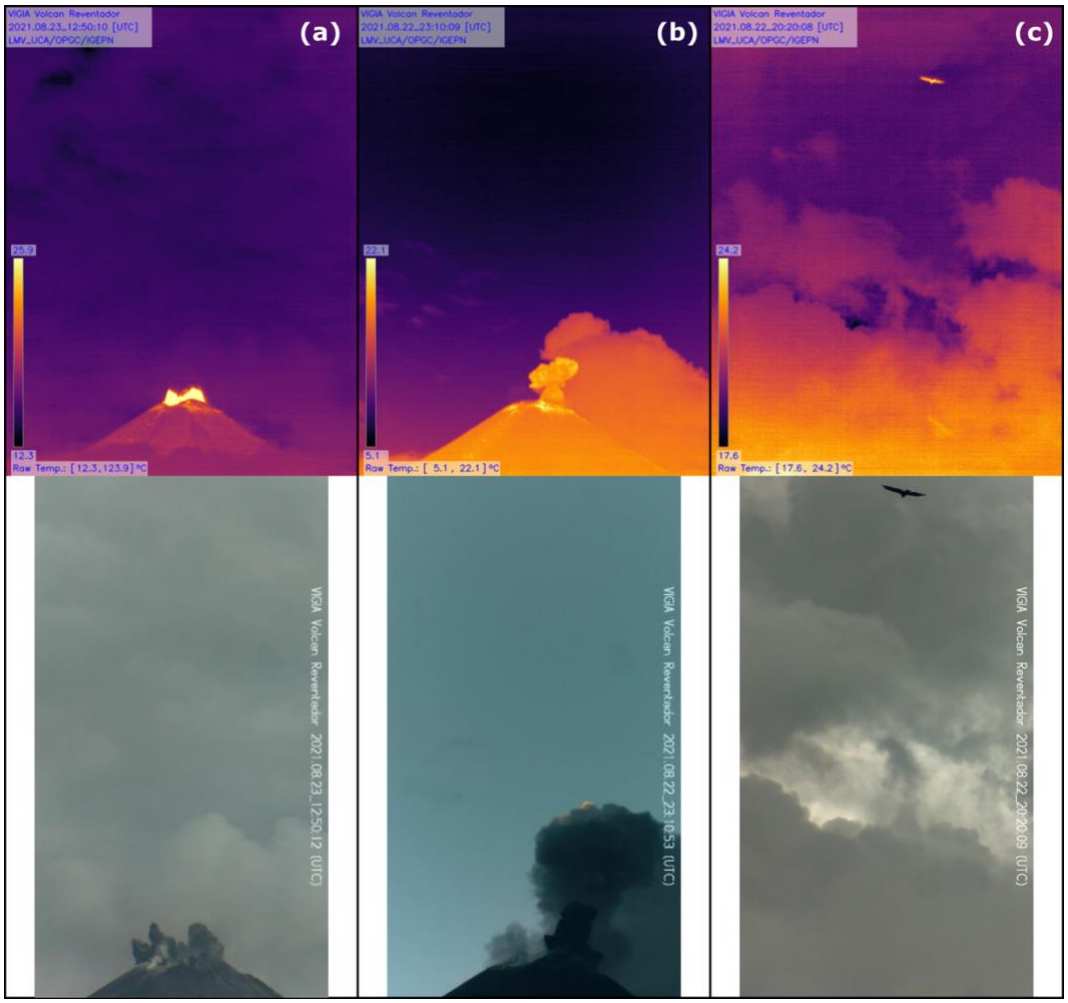

Figure 7 Examples of thermal and visible images captured individually showing different instants of explosions at the Reventador volcano. (a) Beginning of the explosion. (b) A second pulse of the explosion; note that the different illumination of the background plume does not mean a difference in temperature. (c) Many false events triggered by non-volcanic events, a bird in this case, led us to change the triggering system from a simple threshold to a method based on thermal timeseries (see Thermal module).

Daily, the staff of the IGEPN receives a report with the information of the visibility of the volcano during the day, together with the best rated picture, directly to their mobile phones (Figure 7).

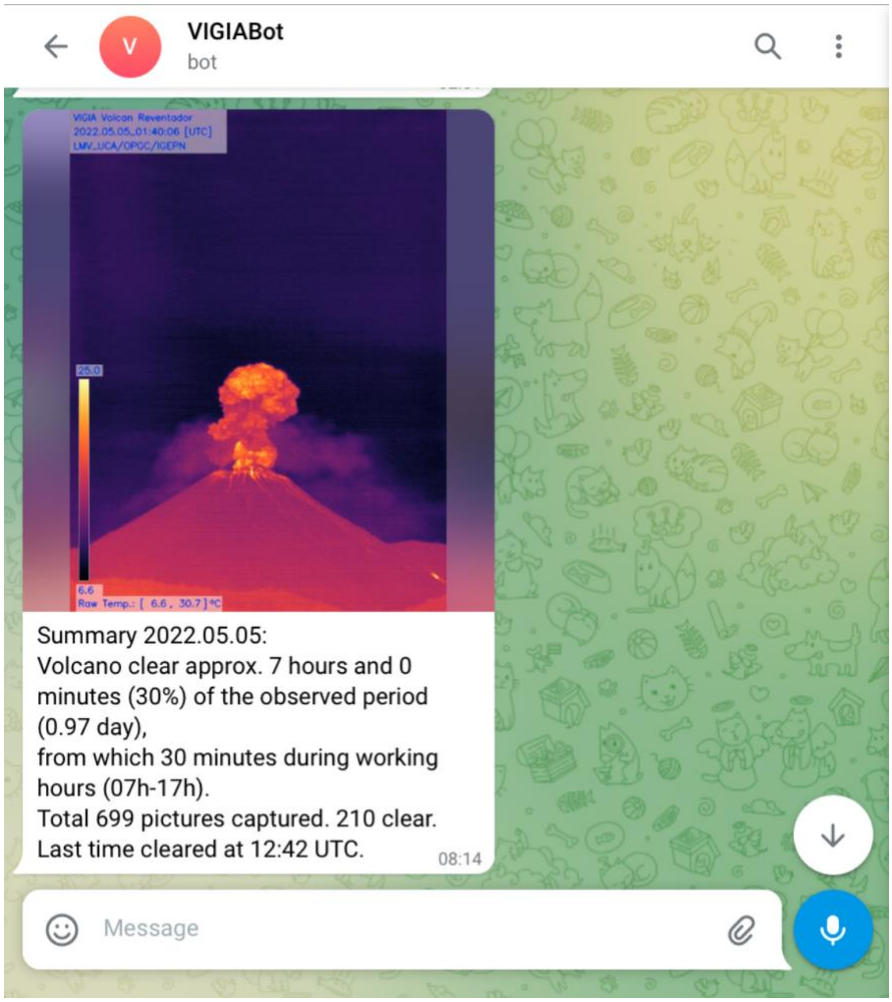

Figure 8 By using a telegram bot, VIGIA sends a daily report with statistics of the day based on the volcano recognition. The picture of the day is the one where the volcano was unclouded and the quality factor is the highest.

Based on the still images recorded and processed, we obtained the portion of each day when the volcano is recognizable by the station, i.e., when cloud cover is low, and measurements are possible. Figure 8 shows these daily intervals, specifying whether these are working hours (between 07h00 and 17h00, local time) during which other observation tasks can be performed, or are intervals during the night. Figure 8 includes the uncertainty, linked to images that were corrupted or not acquired for any reason. We found that the volcano was unclouded 20.3–41.7% of the observed time; and during working hours, the volcano was unclouded 2.4–23.8% of the time. In other words, clear conditions for observation were found to be mostly at night.

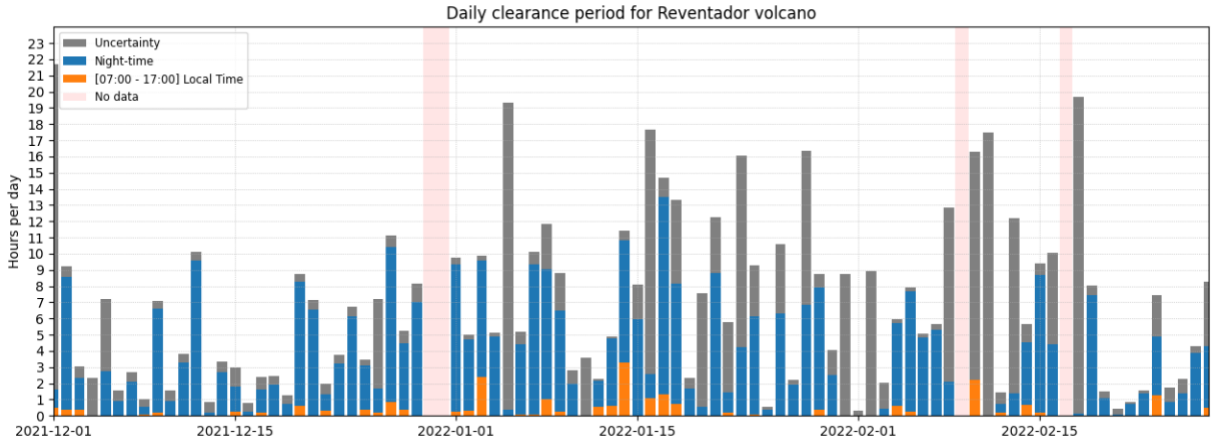

Figure 9 The portion of the day when the volcano is observable by thermal camera (day and night) is represented by stacked blue bars, while the "working" portion of the day (07h00 to 17h00, local time) when the volcano is observable is represented with orange bars. The grey part of the bars represents the uncertainty in the data, which depends on the quantity of images that are corrupted or the instrument did not acquire for any reason.

Thermal imaging depends on the radiation received by the thermal camera. The presence of clouds surrounding the volcano or the observation point impacts directly on the number of images captured, and consequently the number of explosions detected. Observation techniques such as seismicity or infrasound do not encounter this problem although they lack information about the external activity of the volcano (explosions, passive degassing, rock falls, pyroclastic currents, etc.). Unlike VIGIA, most video- and seismic-based monitoring systems count with a module for data processing at the receiving end (observatory), so data processing performed on-site remains minimal. Table 1 shows a comparison between VIGIA and generic seismicity- and video-based monitoring systems. Infrared thermal images with an adequate time stamp hence complement seismic and acoustic observational data to provide an integral description of external manifestations of volcanic activity as shown in Figure 9. For those explosions detected by thermal imaging, we can retrieve more information, such as the plume height, ascent rate, the volume of ejected material, and the size and dispersion direction of the plume (Patrick et al. 2005; Yokoo 2009; Ripepe et al. 2013; Lopez et al. 2015). Moving to a shorter time scale, data recorded as thermal video allows us to analyse and characterise individual explosions (cf. Harris and Ripepe 2007a; Sahetapy-Engel et al. 2008; Capponi et al. 2016b). As an example, Figure 10 shows the comparison of the temperature of the material erupted in one of the explosions that occurred at Reventador volcano on 2022–01–16 with its corresponding seismic waveform recorded by the REVN seismic station, located ~4 km from the current active vent.

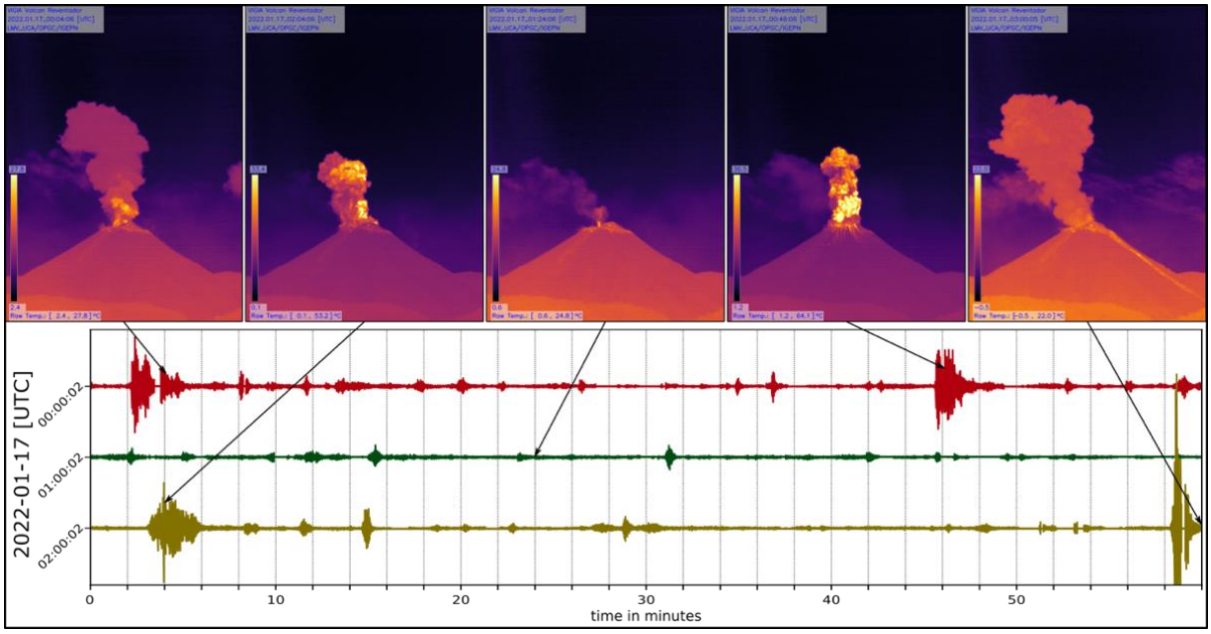

Figure 10 Infrared thermal still images obtained by VIGIA provide visible information of the state of the volcano over time. The lower panel contains an extract of the seismic record from the REVN seismic station located ~4 km from the current active vent of the Reventador volcano. This example from 2022–01–17 shows thermal images with a precise time stamp that complement the information obtained from the seismic record to describe the surficial activity of the volcano.

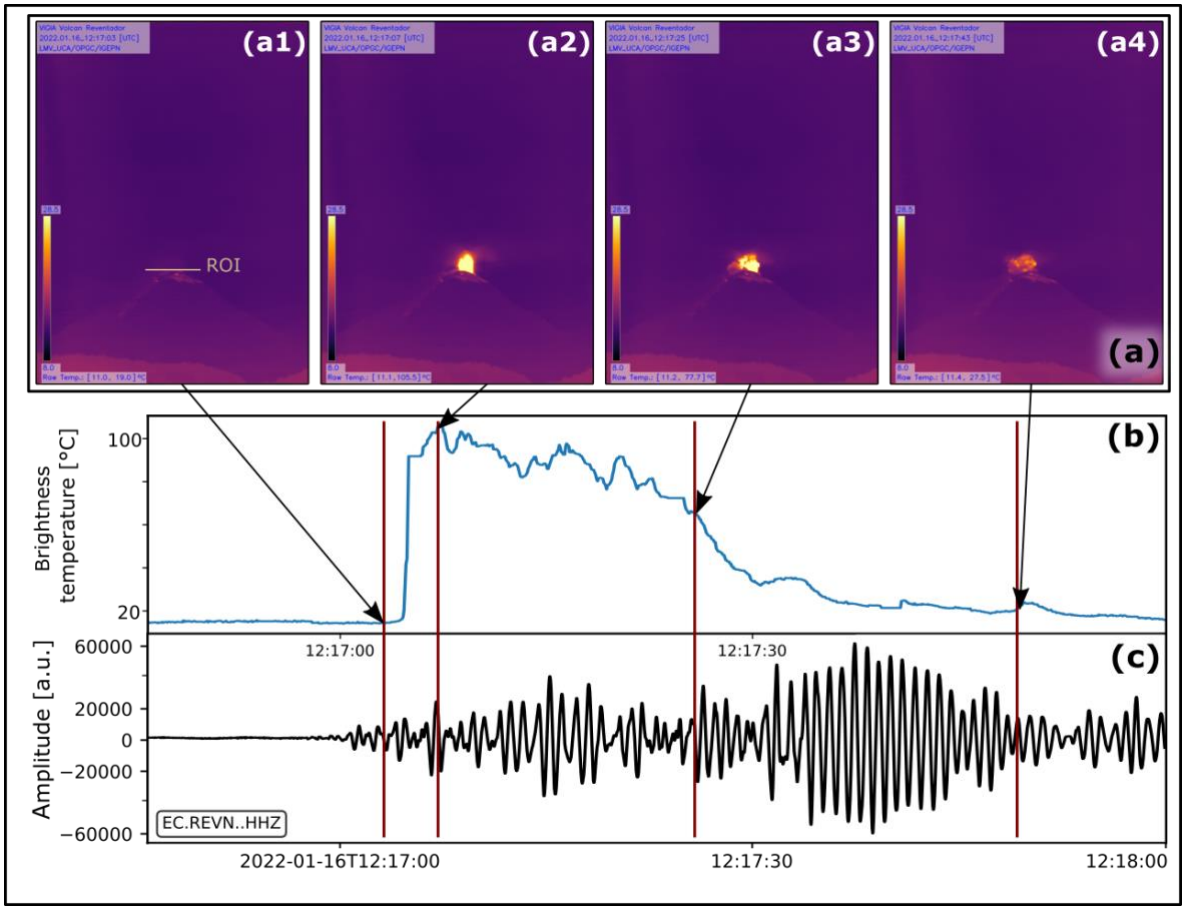

Figure 11 Thermal data recorded as video allow the analysis of explosions on a short timescale. In this example from the Reventador volcano, frames (a) extracted from the thermal video

show the surficial state of the volcano: (a1) before the plume appears over the crater; (a2) at the moment when the temperature measured was maximal; (a3) at the middle of the explosion; and (a4) at the end of the explosion. Panel (b) show the timeseries of the maximal temperature inside the region of interest located just above the crater rim (ROI at (a1)), which can be compared with the record from the REVN seismic station located ~4 km from the active vent, ploted in panel (c).

Table 1. Comparison between VIGIA and generic seismicity- and video-based monitoring systems.

	VIGIA System	**Seismicity-Based Monitoring System**	**Video-Based Monitoring System**
Day/night detection	Yes	Yes	Yes. With limitations
Dependence on meteorological conditions	Yes	No	Yes
Installation complexity	Medium	High	Medium
On-site data processing	High	Medium	Medium
Data volume (per hour)	~20 GB (depends on the number of explosions detected)	~9 MB. Including 3 components, 100 sps, metadata.	~4 GB (depends on the resolution and compression)

One second of thermal video file contains, in the case of VIGIA, 32 images of 640 × 480 pixels, which use 18.75 MB of disk space. This means that one hour of continuous thermal video takes up about 66 GB, and one day will use 1582 GB (1.5 TB). Continuous acquisition of high-resolution thermal video therefore makes little practical sense, especially considering periods where the view of the volcano is impeded by clouds, which, in the case of our study, was about 60% of the time. We therefore configured the system to trigger the recording of thermal videos only when an explosion is detected. The videos are 49 s in duration (four seconds before the trigger plus 45 s after it), which uses around one GB of storage space. During an average day, in terms of volcanic activity and cloud conditions, the system identified 46 explosions, recording 41 GB of thermal video data.

1.5 Summary and Further Work

In the current state (to June 2022), the VIGIA system captures still images in infrared and visible spectrum, which can be used to perform long term studies, for example, studies of morphology changes (e.g., Vallejo Vargas et al. 2019) and of effusion of lava flows (e.g., Harris et al. 2003). The system automatically recognizes when the volcano is unclouded and when an explosion occurs, then it captures high-temporal resolution thermal videos of the explosion; the resulting videos constitute the input material for studies of explosion or plume dynamics (e.g., Bani et al. 2013a; Thivet et al. 2021). VIGIA also records information from temperature, pressure and relative humidity sensors. Daily, it chooses the image of the day and attaches it to the daily report to send it to the IGEPN.

The next stage includes the capability to automatically report dynamic parameters of the explosions, such as maximum plume height and ascent rate. The data provided by VIGIA are already being used as input for the analysis of the long-term explosive activity of the Reventador volcano, which is beyond the scope of this article.

1.6 Conclusions

We have presented VIGIA, a visible and thermal infrared observation system for active volcanoes that follows an edge computing approach whereby the station decides when to acquire high frequency data and transmits statistics and daily reports to the observatory while keeping energy consumption and data volume to a minimum. We have presented the results from the permanent deployment of such a station at the Reventador volcano showing that it successfully identifies adequate observational conditions and automatically triggers the recording of explosions at high resolution; explosions of which the nature and magnitude can be directly compared to seismic information. We have described the hardware and software components of the system extensively (all code scripts available at https://github.com/fvasconez/VIGIA.git (accessed on 10 February 2022)) in the hope that the system can be reproduced, used, and in time, improved by other volcano observatories. An increased and more permanent monitoring of surficial activity at active volcanoes, possible with such systems, should enhance understanding of the volcanic processes at work, as well as forecasting capacities.

Chapter Two: Characterising volcanic explosions

Ash and gas discharge during open vent activity at El Reventador (Ecuador): explosion-style transitions driven by conduit capping

2.1 Introduction

Vulcanian eruptions involve short-lived intermittent explosive events that can continue for periods of years (Mercalli 1907). They are small to moderate in size, feeding eruptive columns typically reaching less than 10 km height, but which can collapse to generate pyroclastic flows (e.g., Marchetti et al. 2009; Yokoo 2009; Hall et al. 2015). Numerous recent volcanic eruptions have been catalogued as Vulcanian including at Sakurajima volcano in Japan since 1955 (Miwa and Toramaru 2013); Fuego volcano in Guatemala in 1978 (Wilson and Self 1980); Soufrière Hills volcano in Montserrat in 1997 (Formenti et al. 2003); Tungurahua volcano in Ecuador in 2013-2014 (Hidalgo et al. 2015; Hall et al. 2015; Battaglia et al. 2019; Gaunt et al. 2020); and El Reventador volcano in Ecuador since 2002 (Lees et al. 2008). Such Vulcanian eruptions can either be caused by phreatomagmatic or purely magmatic processes (cf. Clarke et al. 2015), but the classic model for magmatic Vulcanian eruptions is that they originate from the rupture of a gas-impermeable plug formed in the upper part of a magma-filled conduit (e.g., Fagents and Wilson 1993; Self et al. 1979; Sparks 1997; Woods 1995). Vulcanian eruptions are most commonly found at volcanoes erupting magmas of basaltic andesite to dacitic composition and usually emit only small amounts of ejecta (<1 km^3; Morrissey and Masting 1999). The velocity at which the material is expelled from the vent during Vulcanian explosions has been linked to the amount of gas involved in the event (Self et al. 1979; Wilson and Self 1980; Formenti et al. 2003; Clarke et al. 2015).

Here, our aim is to analyse the ongoing volcanic activity at El Reventador (see General introduction, Figure 12a,b) to propose an explanation for the generation of the Vulcanian explosions and the associated plume dynamics. We present two-hours of quasi-continuous thermal video to describe the evolution of the activity, the duration of each explosion and propose a classification based on explosion characteristics. The flux of SO_2 emitted during the same period was measured by scanning DOAS (Differential Optical Absorption Spectroscopy; Platt and Stutz 2008) while the seismic activity was recorded by broadband seismometers at both proximal (~4 km) and distal (~45 km) locations (REVN and CAYA, Figure 12c). Together, these observations suggest a sequence of four phases of activity reflecting evolving conditions in the shallow conduit. The sequence starts with no degassing and pressure build-up and is followed by destruction of a cap during a Vulcanian explosion. Thereafter, there is a phase of open-vent degassing punctuated by small Strombolian explosions as gas slugs episodically reach the surface. Afterwards, a new plug develops by cooling of the uppermost magma in the conduit, causing gas emissions to decrease until the system becomes fully plugged again; thereafter the cycle recommences.

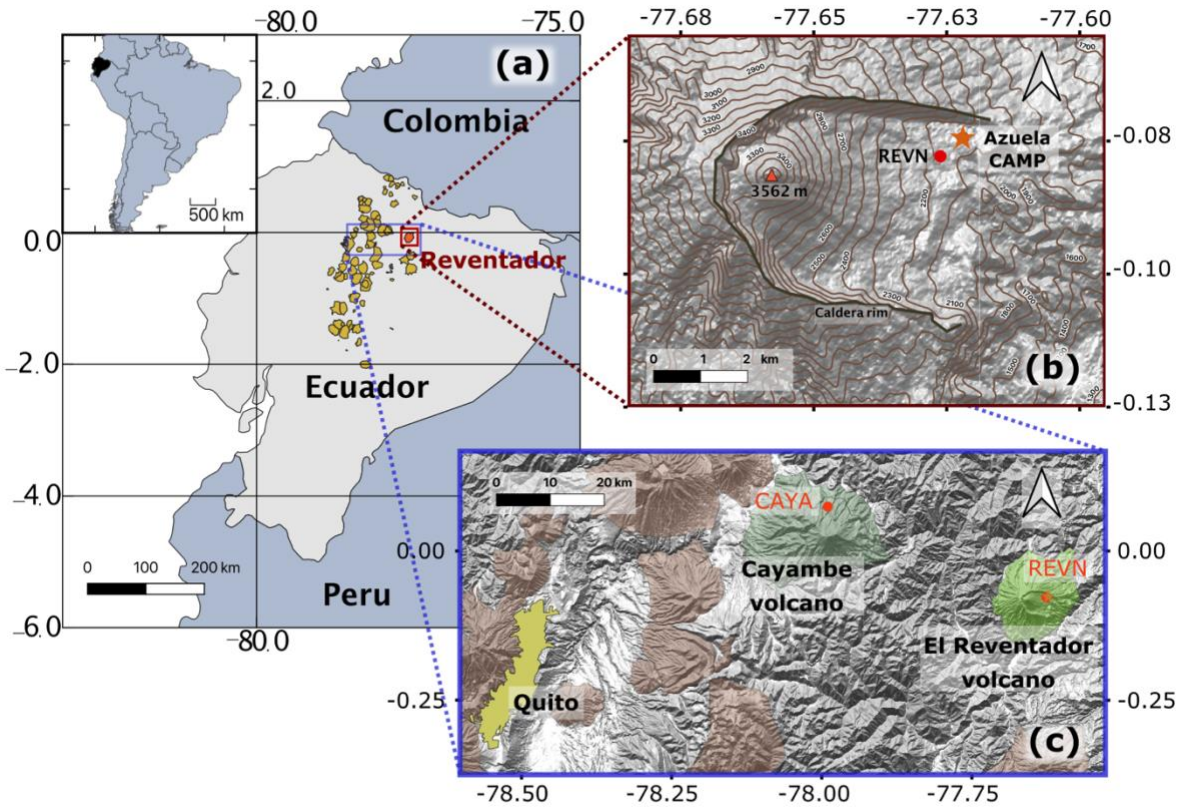

Figure 12 (a) Location of El Reventador in Ecuador where yellow symbols are volcanoes active during the Holocene. Note that El Reventador is located to the east of the eastern side of the cordillera in Ecuador. (b) Enlargement on the current active cone at El Reventador, where "Azuela CAMP" is the site from which measurements were made and "REVN" is the proximal seismic station. (c) Map of the region to the West of El Reventador showing the location of the distal seismic station ("CAYA"), located in the northern flank of Cayambe volcano, and the city of Quito.

2.2 Methodology

The dataset analysed here was acquired during a field campaign in February 2017 and consists of three types of recordings: (1) Thermal infrared video, (2) Scanning DOAS for SO_2 flux, and (3) Seismic data. These we used together with visual observations and major element composition analysis of the emitted ash, which was simultaneously collected with the geophysical data sets (cf. Thivet et al. 2021).

2.2.1 Thermal analysis

Thermal videos were recorded from the Azuela CAMP site, located 4.5 km to the ENE of the active crater (latitude 0.07577S, longitude 77.62473W, altitude 2160 m a.s.l., Figure 12b). We used an Optris PI 640 thermal infrared (8 – 14 µm) camera with a lens that produces a field of view of 15° × 11° and a 640 × 480 pixel image. The pixel size corresponding to a 4.5 km distance to the summit is 1.85 m. Videos of explosive events were captured at a rate of 32 frames per second (fps), with the thermal recording covering a quasi-continuous period of 2 hours, from 23h14 UTC on February 22 to 01h33 UTC on February 23.

To track and define thermal waveforms associated with the explosive events, a region of interest was defined directly above the crater rim (R1, Figure 13) to capture any emission of hot fragments, ash and/or hot gases (Harris and Ripepe 2007a). A second region of interest (R2) was placed 1.85 or 3.7 m vertically above R1 (Figure 13) to determine the ascent velocity from the delay in waveform onset between R1 and R2 (Sahetapy-Engel et al. 2008). Retrieving the kinetic temperature of fragments and hot gasses requires a correction for atmospheric absorption and emission, as well as emissivity effects (Harris 2013). Here, since we are interested in the relative changes of thermal signal instead of the absolute kinetic temperatures, and given minimal atmospheric effects at these altitudes (cf. Harris 2013), we present our data in terms of uncorrected brightness temperatures (cf. Matsushima 2005; Bani et al. 2013). The thermal amplitude is defined as the difference between the peak temperature and background temperature in any waveform (Harris and Thornber 1999; Ripepe et al. 2005). The timestamps for the time series were recorded using the operating computer, set to GPS time.

Durations of ash and/or gas venting were also obtained from these thermal time series. In most cases, the starting and ending points of an explosion are clearly defined (Figure 14). In some cases, however, when there is a period of slow ash dispersal at the end of the event, the definition of the end of the explosion becomes ambiguous. In such a situation, we define the end of the event as the instant when the temperature inside the region R1 drops below the limit set as twice the background temperature (Figure 14).

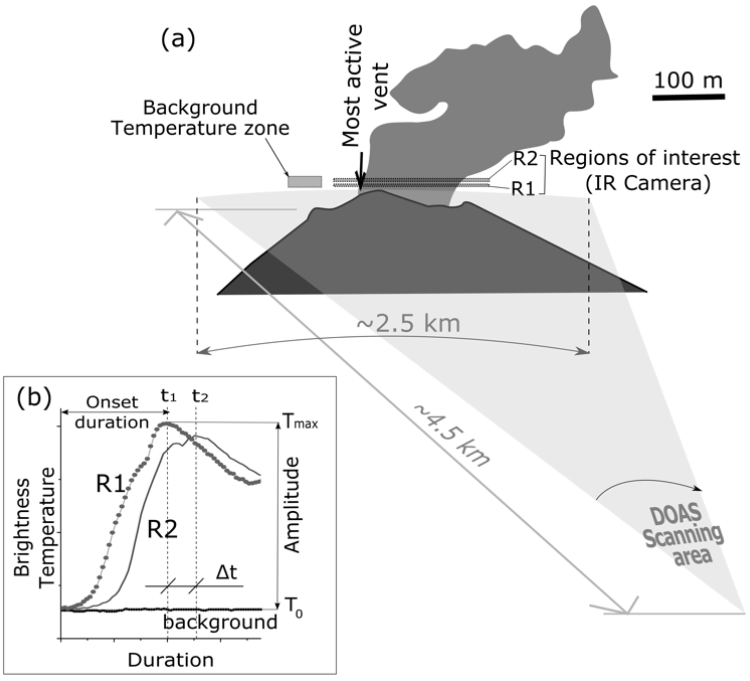

Figure 13 (a) Layout of the measurement setup. The thermal camera and the scanning DOAS instrument were located 4.5 km to the east of the active cone. Two regions of interest (R1 and

R2) are placed directly above the crater to track any fluctuation in the temperature due to hot material exiting the vent. The temperature of the background was also measured in the clear sky region as indicated. Also marked is the horizontal scanning plane covered by the DOAS instrument. (b) Timeseries obtained from R1 and R2. Definition of the time delay between the peak temperature recorded at R1 (t_1) and R2 (t_2) as used to calculate ascent speed, onset time (the time to move from background temperature, T0, to peak temperature, T_{max}), and thermal amplitude (T_{max}-T_0) (after Harris and Ripepe, 2007b). Example is from the onset of explosion 4.

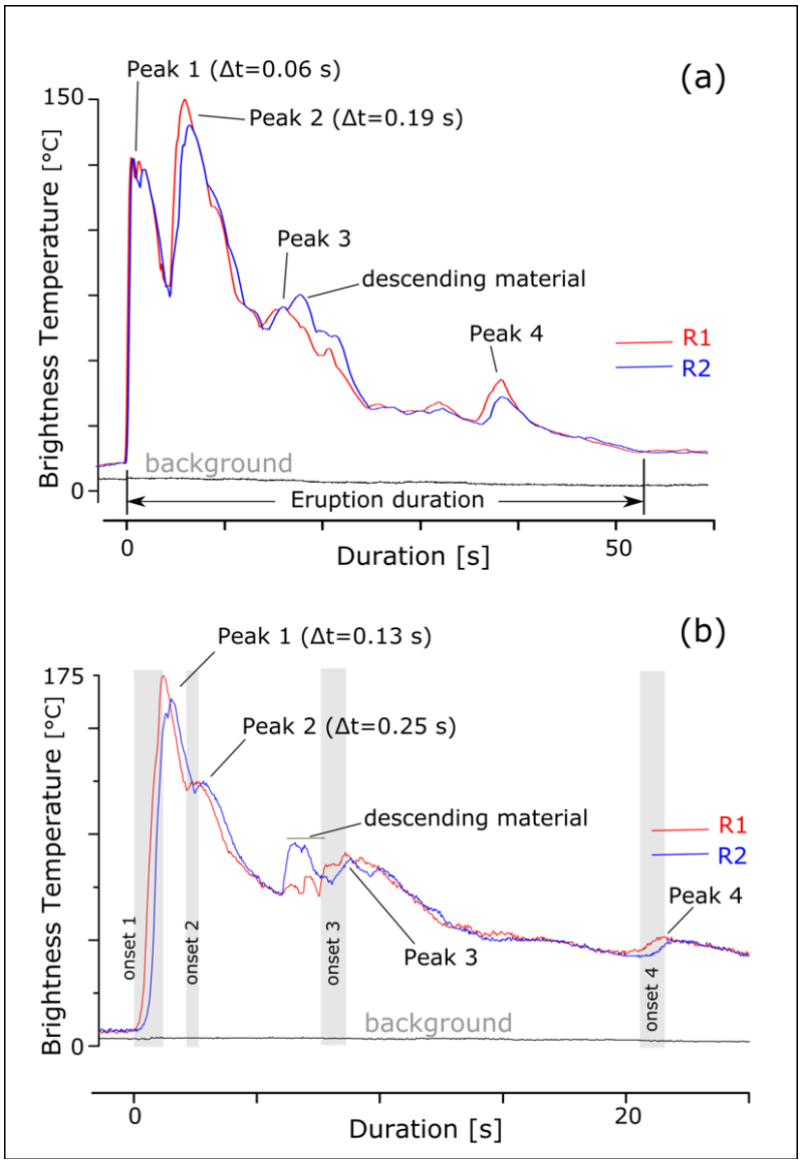

Figure 14 Time series from regions of interest R1 (red line) and R2 (blue line) for explosions (a) 11 and (b) 13. When hot pulses of ash and/or gas transit through R1 and R2, they trigger an impulsive increase in temperature, followed by a slower decrease. Objects first cross R1 and then R2, causing a delay between the two waveforms. Peaks that appear first in R2 before R1 correspond to hot bombs and blocks falling back to the ground. The time delay between a peak at R1 and its corresponding pike in R2 is signaled as Δt (Figure 13).

2.2.2 SO_2 flux

To estimate SO_2 flux we used a scanning DOAS instrument from a fixed position at the Azuela CAMP site (Figure 13). During measurements, the plume rose several hundred meters

vertically above the summit before drifting to the east, enabling both horizontal and vertical scanning of the plume. Thirty-three spectra per scan were collected with a step angle of 0.9°, covering a horizontal scanned length of ~2.5 km in the horizontal configuration (Figure 13a). The angular resolution was maintained when switching to the vertical configuration. The spectrometer used was an Ocean Optics USB2000+ with a spectral range of 290-440 nm and a spectral resolution of 0.5 nm FWHM. The SO_2 column amounts (ppm.m) were retrieved using standard DOAS calibration and analysis procedures (Platt and Stutz 2008). Reference spectra included in the non-linear fit were obtained by convolving high resolution SO_2 (Bogumil et al. 2003) and O_3 (Voigt et al. 2001) cross sections with the instrument line shape. A Fraunhofer reference spectrum and Ring spectrum, calculated in DOASIS (DOAS Intelligent System; Kraus 2006), were also included in the fit. Measurements were made between 13h21 and 14h15, UTC, on February 23, 2017. The plume speed was calculated following the method described above in the paragraph of thermal analysis but also applied to periods of passive degassing. The plume transport speed relative error is conservatively assumed to be around 30–35%, which is towards the higher end of the range of past estimates (e.g., Arellano et al. 2008; Bani 2012; Bani et al. 2013b).

2.2.3 Seismicity

We used two broadband seismic stations from the permanent monitoring network of the IGEPN: REVN located 4 km from the summit of El Reventador and CAYA located 45 km to the west on the northern flank of Cayambe volcano (Figure 12). Both stations are equipped with Trillium Compact 120s sensors with Q330 Kinemetrics digitizers. Data are recorded with a 100 Hz sampling frequency. Station REVN records both explosion quakes and tremors from El Reventador. Instead station CAYA, while normally used to monitor the activity at Cayambe volcano, also records the most energetic explosion-quakes from El Reventador.

2.2.4 Ash composition

Ash fall deposited during the observation period was collected and analyzed for major element bulk composition. To do this, 100 mg of sample was mixed with 300 mg of $LiBO_2$, melted in an induction oven at 1050 °C for 4.5 min using graphite crucibles. The resulting glass beads were then dissolved in a solution of deionized water and nitric acid (200 ml) and finally diluted by a factor of 2000. The solutions were analyzed by ICP-AES (An ULTIMA-C Horiba scientific, Jobin-Yvon spectrometer was used) at the Laboratoire Magmas et Volcans in Clermont-Ferrand (France).

2.3 Results

The activity we observed at El Reventador on 22 and 23 February 2017 was dominated by intermittent explosions that fed ash plumes up to about one kilometer above the summit, before detaching and being pushed to the east by the prevailing wind. The activity reports of IGEPN show a mean of 40 explosions per day and a similar number of long-period (LP) seismic events were recorded by station REVN. A small area of incandescent lava could be seen on the upper part of the northern flank of the cone. Most of the ejected blocks and bombs remained within the summit crater; although, during larger explosions, incandescent blocks were seen rolling down the flanks of the cone (Figure 15).

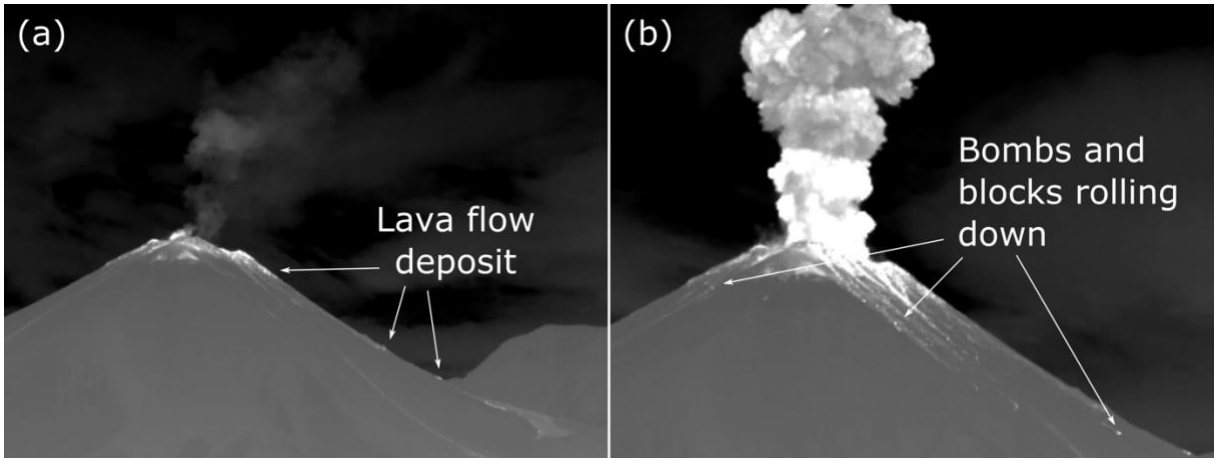

Figure 15 Thermal infrared images of the summit area. (a) A small area of the deposit of a recent lava flow was recognizable on the northern flank. (b) During energetic explosions, most of the ejected blocks and bombs rolled down the flanks of the cone.

2.3.1 Thermal data

Thirteen explosions of variable thermal amplitude were recorded over the 2-hour measurement period. Another 13 less energetic degassing events were also recorded during this observation period. All thermal infrared videos are available in the Electronic Supplementary Material (ESM Video 01-Video 19).

Thermal amplitudes of the explosions varied between 40°C for the less energetic (minor) events (explosion 7) and up to 263 °C for the most energetic (major) events (explosion 3). Minor explosions only lasted for around 10 s, while major explosions persisted for up to 140 s. The 32 Hz acquisition rate of the thermal recording allowed a detailed thermal waveform to be generated for each event, highlighting successive thermal peaks within each explosive discharge. Figure 5 shows an example of a sequence of thermal images acquired during an explosion with the corresponding thermal waveform. In this example, at least 11 thermal peaks are recorded over the 30 s of duration of the event highlighting a series of explosive pulses (cf. Harris et al. 2008). Generally, as in the Figure 5 waveform, the highest thermal amplitude

recorded during any single explosion corresponded to the first or second peak, and amplitudes thereafter declined (cf. Figure 14), consistent with a waning emission.

The time delay between consecutive peaks varies from 0.03 to up to 0.6 s, implying a decrease in velocity with increased delay (Figure 13b). For our travel distance between R1 and R2 of 3.7 m, this gives velocity end members of 3 to 120 m s^{-1}, with an average of 27 m s^{-1}. We see from Figure 3 that the delay between any two peaks increases with time during any individual event, increasing from 0.06 to 0.19 s in Figure 3a and from 0.13 to 0.25 s in Figure 3b. This is consistent with a decrease in emission velocity with time, from 30 to 10 and 20 to 7 m s^{-1} in the two cases, respectively. The decay in thermal amplitude is also consistent with an event that decays in energy with time.

On the basis of thermal waveform (i.e., their thermal amplitude and duration), we classified the recorded emissions into three types (Figure 17).

- Type A (Figure 17a), is characterized by the highest thermal amplitudes (263 °C), longest durations (140 s) and highest plumes (> 800 m).
- Type B (Figure 17b), is characterized by moderate thermal amplitudes (175 °C), durations of around 25 s and plume heights reaching up to 400 m.
- Type C (Figure 17c) is characterized by the lowest thermal amplitudes (100 °C), durations of about 15 s and plume heights of up to 300 m.

This all implies a decrease in energy between each event type. We find that each event type tends to occur in a specific sequence (Figure 18a). Type B and C events tend to occur together, with Type B punctuating clusters of repeated, at the rate of 0.2-0.7 Hz, Type C events (Figure 18b) Such sequences are typically followed by explosion free periods (Figure 18c), which are terminated by single, discrete Type A events (Figure 18d). Explosion free periods show the existence of very low amplitude (10 °C) single peaked waveforms of 12 – 20 s in duration and which are associated with exhalations of gas (Figure 18c). Within the sequence of Figure 7e, three individual events of around 30 s in duration occurred with one-minute delays, with decreasing thermal amplitudes.

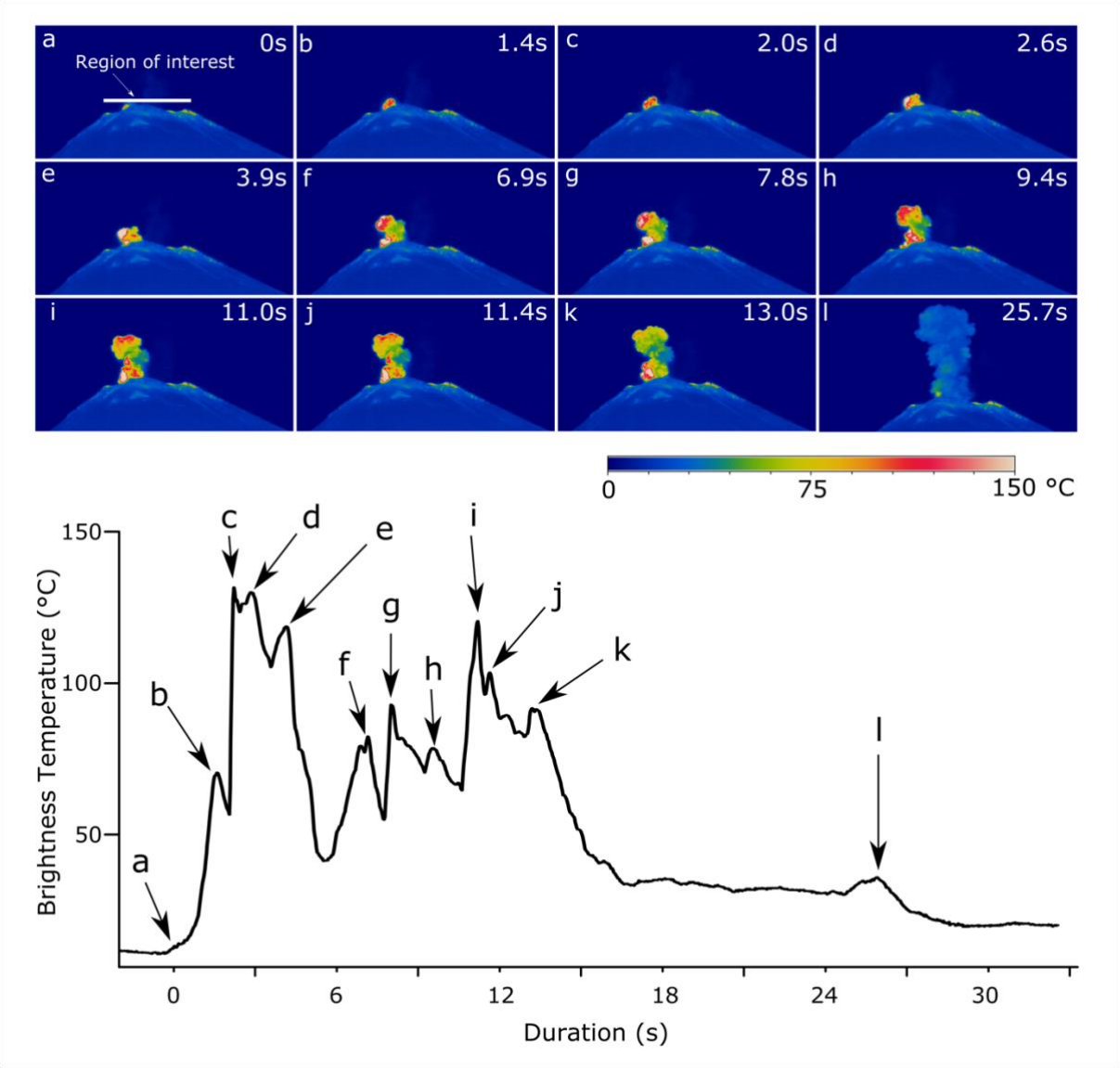

Figure 16 Sequence of thermal images acquired during explosion 2 and the corresponding thermal waveform for the Region of Interest labelled in (a). Labelled letters on the waveform related to the location of thermal video frames (a) through (l). The eruption lasted 30s with 11 peaks each associated with a burst of material passing through the ROI (cf. Harris et al. 2008).

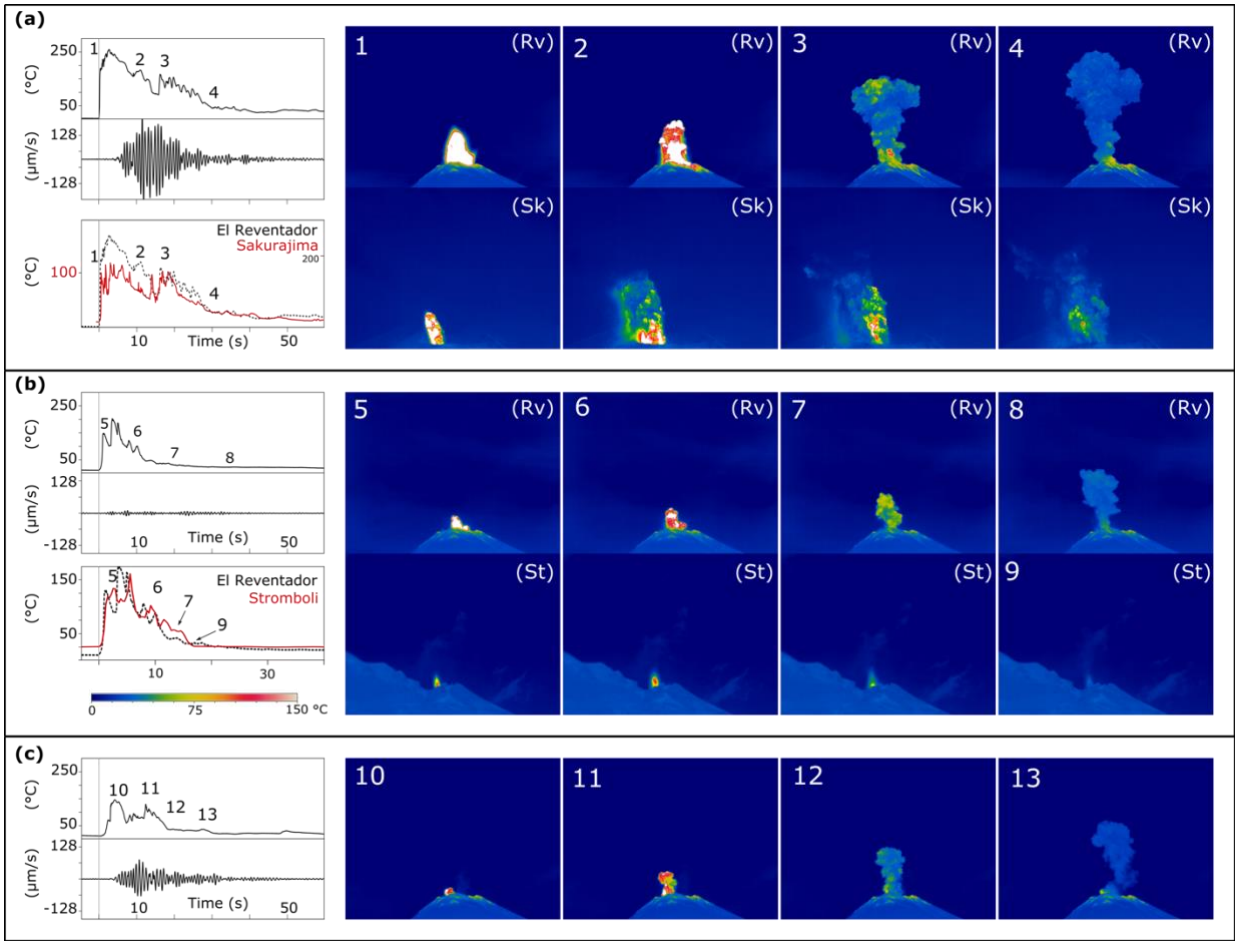

Figure 17 Thermal and seismic waveforms for (a) Type A eruptions of Phase 4, (b) Type B eruptions of Phase 2, and (c) Type C eruptions of Phase 1. Thermal images in the right-hand panels correspond to the times shown as numbers (1-13). The thermal waveforms and duration of the Type A explosions in Phase 2 are similar to those of Sakurajima volcano (as plotted in red in a; data from A. Harris: Sakurajima eruption of 2013-07-27). The corresponding thermal images at Sakurajima, taken at similar time intervals as the Reventador ("Rv") are marked "Sk". In the case of Type A eruptions during Phase 4 (a), the thermal waveform and duration is comparable with those recorded at Stromboli volcano ("St") (as plotted in red in a; data from A. Harris: eruption at Stromboli recorded on 2008-06-03). The full videos with corresponding seismic and thermal waveforms from El Reventador can be found in the ESM.

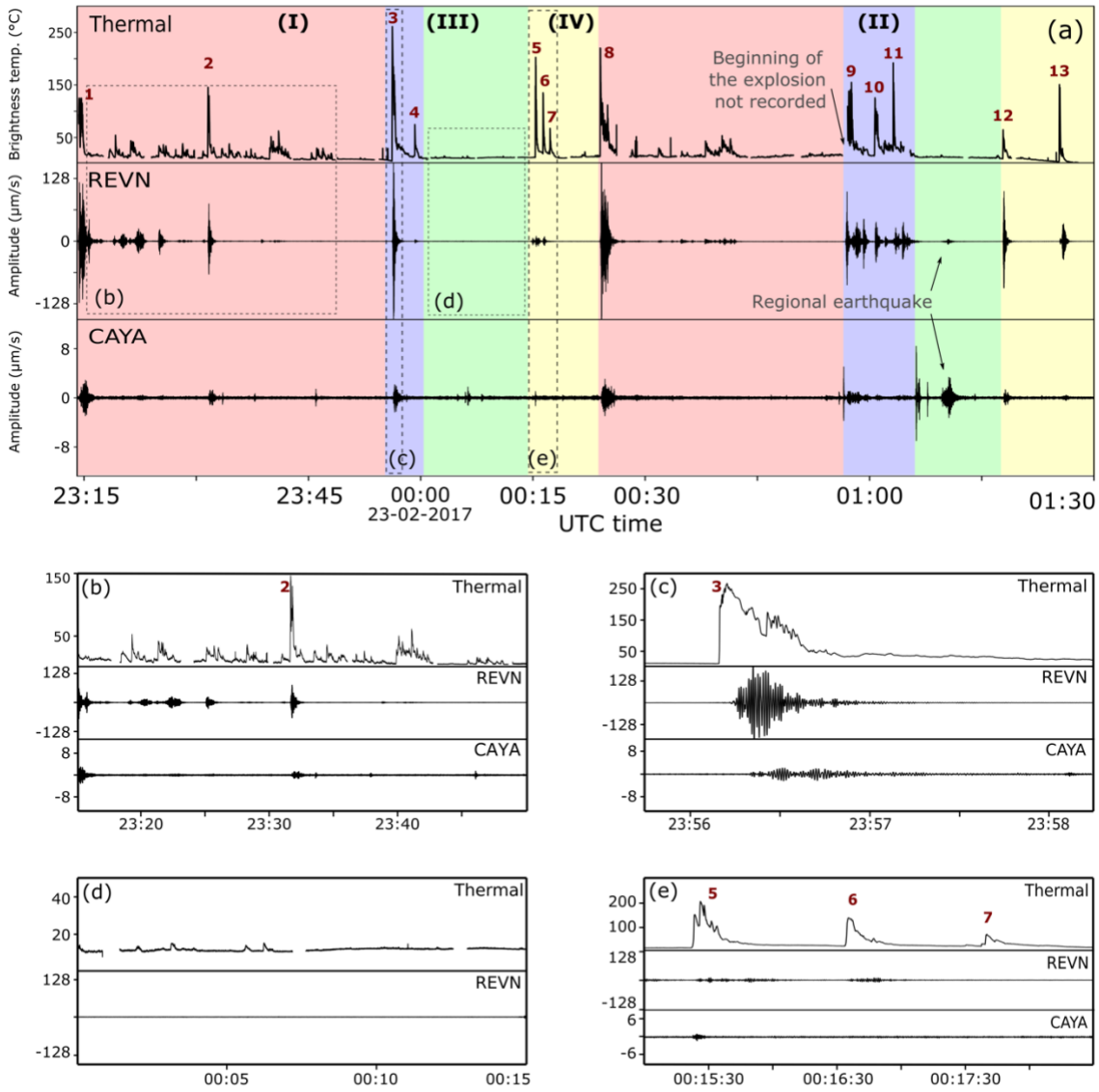

Figure 18 (a)Temperature time series from region of interest R1 (Fig. 2) and the corresponding seismic signals from REVN and CAYA (Fig. 1). The main explosions are numbered from 1 to 13. Four distinct behavior, outlined with different background colors, can be distinguished from the thermal recording, including (b) a nearly continuous occurrence of Type B and C events, (c) Type A and B events (explosions 3, 9, 10, 11), (d) the low amplitude passive degassing phase; and (e) successive Type A and B event (explosions 5, 6, 7, 12, 13). Phases I, II, III, and IV occurred successively and repeated themselves once over the two hours recording, each sequence of phases lasting around one hour and 15 minutes.

2.3.2 SO_2 flux

Figure 8a shows the fluctuation of SO_2 column amount obtained with DOAS. Sunrise was at about 06h30 (local time), even though light conditions at 08h00 were not optimal for DOAS measurements, there was sufficient light intensity to perform scanning considering that our system has the capacity to modify automatically the integration time to allow acquisition of spectra with light intensity within an acceptable range. During our measurements, clouds started to develop progressively, first around and over the summit then directly above the

scanner, as well as inside the caldera and between our observation site and the vent, forcing us at first to change the scanning orientation from horizontal to vertical, and finally to end the measurements. This also caused some periods of unreliable data (Figure 19a). A mean plume velocity of 5.6 m s^{-1} was obtained using the thermal infrared camera video, allowing us to convert to SO_2 flux for approximately one hour of data as reported in Table 1. Fluxes fluctuated between 0.8 and 1.5 kg s^{-1} with a mean SO_2 emission rate of 1.1 ± 0.7 kg s^{-1} (Figure 19b). The daily SO_2 emission rate from El Reventador was about 95 ± 60 tons per day during our observation.

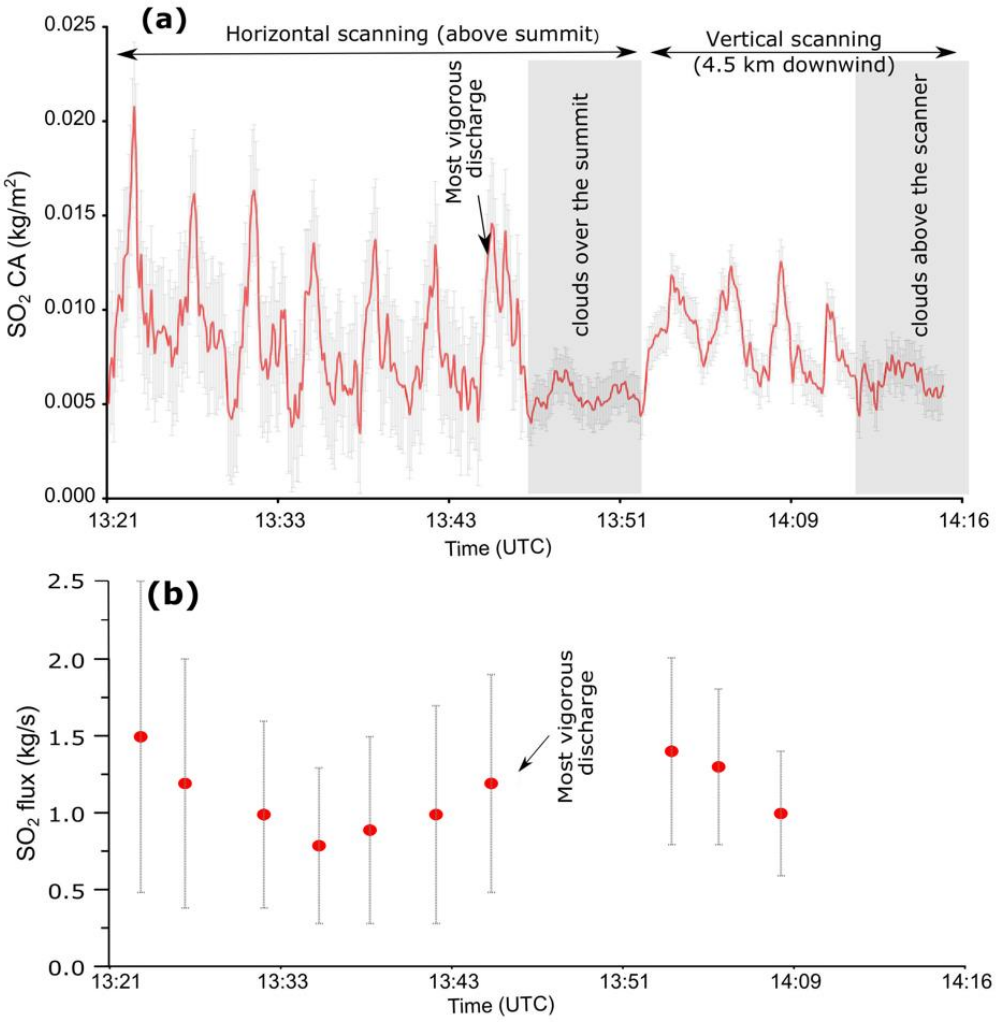

Figure 19 (a) SO_2 column amount (CA) as derived from continuous scanning. The occurrence of clouds that triggered the shift from horizontal scanning to vertical scanning geometry, as well as the termination of scanning, is highlighted in gray. (b) The SO_2 flux calculated for each scan shows a cyclic trend despite the wide margin of errors.

Table 1. Results of SO_2 measurements performed on 23 February 2017 using scanning DOAS.

Scan	Start time (UTC)	End time (UTC)	Projected distance (m)	Number of spectra in the plume	Average column amount (g/m^2)	SO_2 flux (kg/s)
S1	13:21	13:24	1790	23	0.15	1.5 ± 1.0
S2	13:24	13:27	1400	18	0.14	1.2 ± 0.8
S3	13:31	13:33	1326	17	0.13	1.0 ± 0.6
S4	13:34	13:36	1170	15	0.12	0.8 ± 0.5
S5	13:38	13:41	1320	17	0.12	0.9 ± 0.6
S6	13:41	13:44	1560	20	0.11	1.0 ± 0.7
S7	13:44	13:47	1400	18	0.15	1.2 ± 0.7
S8	13:47	13:50	Clouds over the summit			
S9	13:50	13:52				
S10	14:02	14:04	552	24	0.35	1.4 ± 0.6
S11	14:05	14:07	276	12	0.35	1.3 ± 0.5
S12	14:07	14:10	460	20	0.32	1.0 ± 0.4
S13	14:10	14:12	Clouds above the scanner			
S14	14:12	14:15				
						Mean SO_2 flux estimation: 1.1 ± 0.7 kg/s

2.3.3 Seismicity

Using recordings from station REVN (Figure 12), we identified nine signals that can be considered as explosion quakes, these are coloured in blue in Figure 9. These explosion quakes are also clearly identified in the recordings of the station CAYA. Ten transient signals observed at CAYA are unrelated to the activity at El Reventador and are coloured in red in Figure 9. These seismic signals correspond to volcano-tectonic events or ice quakes originating from Cayambe itself. In addition, three episodes of harmonic tremor were identified at REVN, coloured green in Figure 9. Finally, both stations recorded a regional earthquake whose hypocentre was located in northern Peru by IGEPN (Figure 18, Figure 20).

The harmonic tremor episodes lasted a few minutes and always appeared after an explosion quake. All Type A events (explosions 5, 6, 7, 12 and 13) were recorded as low frequency waveforms by the proximal seismic station (REVN) but not all of them appear in the distal (CAYA) seismic recordings (Figure 20). Thermally, these explosions are associated with the highest energy events and have variable thermal amplitudes. However, theses amplitudes are not directly correlated to the amplitude of corresponding seismic signals.

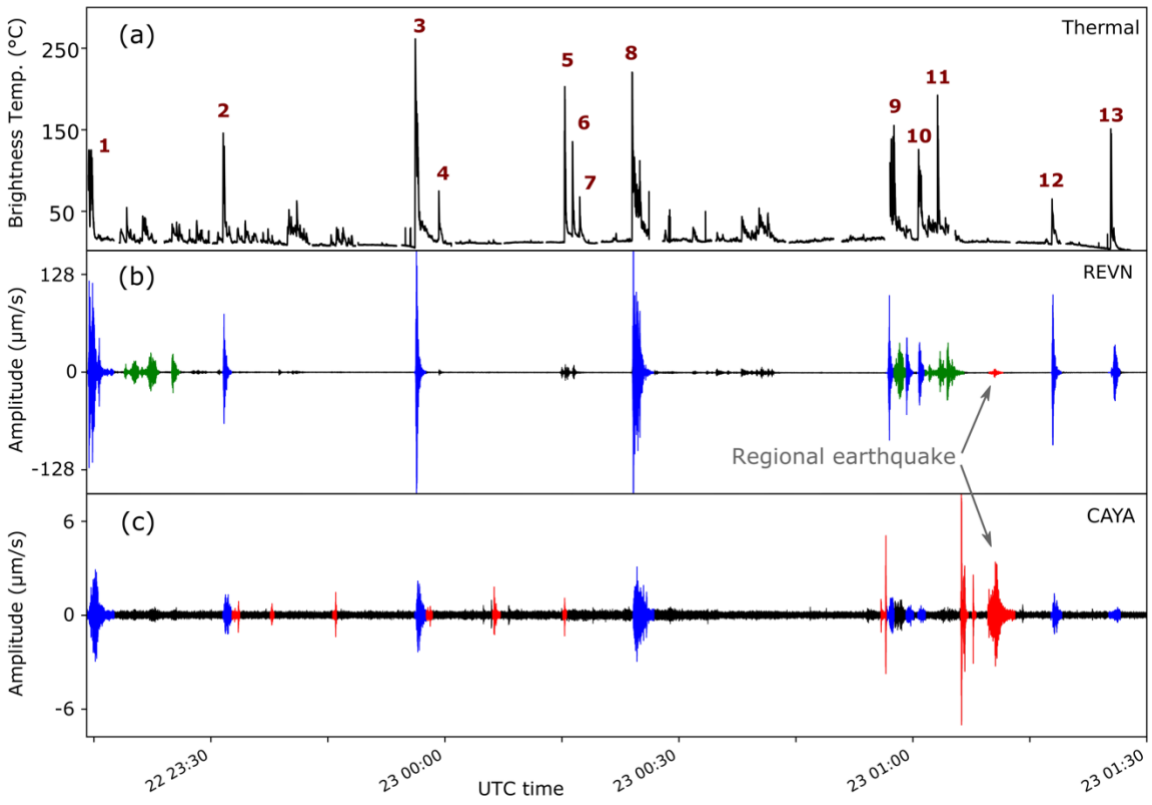

Figure 20 (a) Timeseries of brightness temperature from thermal infrared imagery on which the thirteen Type A and B explosions are identified. (b) Seismic signals from station REVN, located 4 km to the east of the active crater. (c) Seismic signals from station CAYA, located 45 km to the northwest of El Reventador. Most of the explosions that can be identified at the proximal seismic station appear at the distal station as well (marked in blue). The seismic events coloured in red are not related to El Reventador activity; they are volcano-tectonic events or ice quakes from Cayambe and a regional earthquake. Harmonic tremor episodes are highlighted in green; and are all preceded by an explosion. The sequence of explosions 5, 6 and 7 produced high thermal amplitudes but low seismicity. Instead, explosions 12 and 13 produced low thermal amplitudes but moderate seismic amplitudes.

2.3.4 Bulk Ash composition

The ash is of andesitic composition with SiO_2 contents around 58 wt. % (Table 2). The bulk ash composition falls in the trend displayed by whole rocks of El Reventador as reported by Samaniego et al. (2008) (Figure 21).

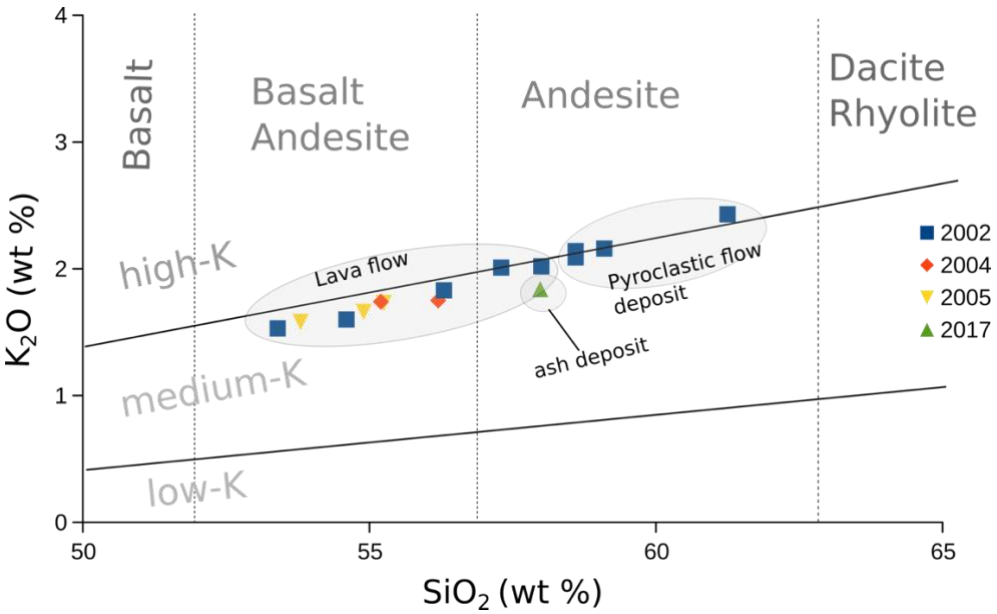

Figure 21 K_2O versus SiO_2 classification diagram (Peccerillo and Taylor 1976) showing the composition of lavas extruded from El Reventador volcano between 2002 and 2005 (Samaniego et al. 2008) and the ash sample collected during our observation period.

Table 2. Bulk composition of ash samples collected following a Vulcanian explosion at El Reventador on 22 February 2017.

SiO_2 (wt%)	Al_2O_3 (wt%)	Fe_2O_3 (wt%)	MgO (wt%)	CaO (wt%)	Na_2O (wt%)	K_2O (wt%)	TiO_2 (wt%)	MnO (wt%)	P_2O_5 (wt%)	Ba (wt%)	Sr (wt%)	Total	H_2O (wt%)
57.98	17.67	6.93	3.76	6.73	3.57	1.84	0.88	0.11	0.37	0.14	0.10	100.08	0.24

2.4 Discussion

Based on coupled patterns in the thermal and seismic waveforms, as well as trends in the SO_2 flux time series, we can group our data into four successive phases (Figure 18a). We emphasize that the dynamics presented in this work is representative of our period of observation and must then be extrapolated with caution, but we believe it gives a useful guide to the dynamics driving El Reventador's open-vent persistent explosive activity.

Phase 1 consists of about 30 minutes of quasi-continuous, minor bursts of gas and ash as seen in the thermal time series as a series of Type C and B events (Figure 18a; ESM Video 03). These events appear with variable amplitudes in the proximal seismic station but are barely recorded by the distal seismic station (Figure 18b).

Phase 2 consists of a single or series of Type A and B explosion(s) that last around two minutes (Figure 18c; ESM Video 07). These events are clearly distinct from explosions seen in phase 1 as they expel an appreciable quantity of ballistics covering the upper part of the edifice and occasionally generate minor rock falls and pyroclastic density currents (cf. ESM Video 07 and ESM Video 03). Seismicity with high amplitude mirrors the high thermal

amplitude signal (Figure 18c). The duration, the waveform and thermal amplitude of the explosions occurring in this phase (Figure 17a) are similar to those of ash venting occurring at Santiaguito volcano (Johnson et al. 2004; Sahetapy-Engel et al. 2008; Marchetti et al. 2009) and Vulcanian explosions at Sakurajima volcano (Yokoo 2009). Figure 6b shows the comparison between a Type A explosion of Phase 2 at El Reventador and one of Sakurajima's Vulcanian explosion recorded in July 2013 (A. Harris, unpublished data), where the duration and shape of the waveform are similar. We thus interpret these event types to be similar in terms of source, emission and ascent dynamics. We thereby label them "Vulcanian" and assume they are related to stick-slip of a highly viscous plug as at Santiaguito (cf. Bluth and Rose 2004; Sahetapy-Engel et al. 2008) or, more likely, failure of a high viscosity cap in the true Vulcanian sense (Johnson and Lees 2000; Hall et al. 2015)

Phase 3 consists of 10 to 15 minutes of passive degassing (Figure 18d; ESM Videos 08 and 09). During this phase no explosions are recorded, either in the thermal or seismic records (n.b., signals registered at the CAYA station are not associated with El Reventador).

Finally, phase 4 consists of a period of about 10 minutes in which we record a series of Type B explosions (Figure 18e; ESM Videos 10, 18 and 19). The seismic amplitude of these events is very small when compared to the seismic amplitude associated with the explosions recorded in phases 1 and 2 (Figure 17) and is the only case where seismic and thermal signals are decoupled. The waveform of the thermal signal and the duration of the individual explosions in this phase (Figure 17) are comparable to those observed in explosions at Stromboli (e.g. Harris and Ripepe 2007a; Harris et al. 2012; Patrick et al. 2005) and Villarrica (Marchetti et al. 2009), as shown in Figure 6c. We thus interpret these event types to be similar in terms of source, emission and ascent dynamics. We thereby label them "Strombolian" and assume they are related to bubble bursting at a relatively low viscosity surface (Shinohara 2005; Patrick et al. 2007) or at-least one that is thinly capped (Gurioli et al. 2014).

Activity developed through these four phases twice during the two-hour observation period. Although the SO_2 flux measurements could not be obtained concurrently (DOAS measurements rely on good sunlight while thermal measurements are best performed at night), they also oscillate over a timescale of about one hour thus following the same timescale of trend observed in the thermal and seismic recordings by visual observations.

Phase 1 characteristics can be interpreted as a conduit which is mostly plugged, or in the process of plug development. Degassing occurs as short bursts of "ash venting" associated with thermal and seismic signals and decreases over time, potentially indicating progressive sealing of the system. Ash venting may be the result of stick-slip events impacting the developing plug (cf. Neuberg 2000; Lensky et al. 2008). Such process can lead to a decrease

in the permeability of the upper part of the conduit and, subsequently, to an increase in the pressurization of the system. The progressive decrease of the SO_2 flux, as evidenced in this work, further supports this observation. Phase 1 would hence correspond to the formation of a gas-impermeable cap in the upper part of the conduit (Del Bello et al. 2015; Capponi et al. 2016a), probably caused by cooling and degassing of the shallowest portion of the magma column, which induces a rheological stiffening and increases magma viscosity (Gurioli et al. 2014). The energetic Type A explosion(s) characterizing phase 2 (Figure 17a), can be interpreted as the culmination of pressure accumulation in the conduit, an accumulation which is finally released by one or a series of energetic explosions (Figure 18a) destroying the cap. This model is consistent with the ejection of ballistics, the high amplitudes in both the thermal and seismic signals and the similarity with waveforms recorded during “Vulcanian” events at other systems (cf. Figure 17). During phase 3, which is explosion-free, unhindered degassing occurs, and is interpreted as a period of purely open vent (uncapped) activity. Finally, in phase 4, with the system still in an open-vent configuration, gas slugs can travel through the upper part of the conduit and burst at the free surface producing intermittent “Strombolian” explosions. The thermal amplitude of some of these explosions is not mirrored by the seismic amplitude, possibly because of a source at a shallower level than those with appreciable seismic amplitude at both proximal and distal stations (Figure 18e). Our thermal, seismic and, to a lesser extent, SO_2 flux observations therefore highlight cyclic transitions at El Reventador between plugged and open vent configurations (Figure 22).

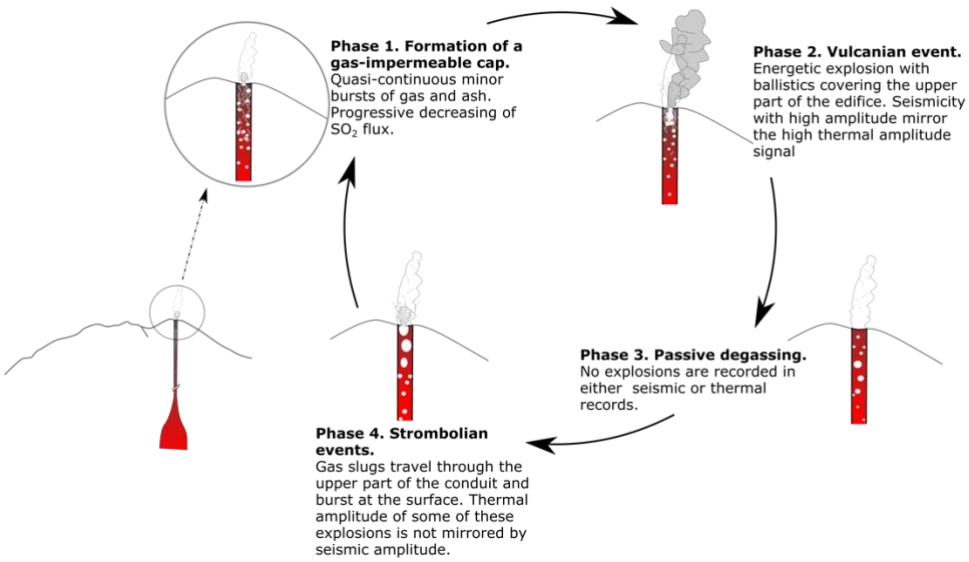

Figure 22 In this work, the dynamics of El Reventador's activity can be characterised by four distinct phases: the formation of a gas-impermeable cap, the phase of Vulcanian explosions, a period of passive degassing and a phase of Strombolian explosions. This last phase gradually fades away as the permeability in the vent decreases and the impermeable cap starts to form.

2.5 Conclusion

Our analysis of thermal, seismic, and SO_2 flux measurements at El Reventador clearly highlights the temporal succession of different types of explosive and degassing activity that can be classified into four phases. Phase 1 is characterized by frequent, nearly continuous, explosions of small thermal and seismic amplitude diminishing with time, indicating the progressive self-sealing of the conduit. This restricts the gas flow and builds up pressure in the conduit. Phase 2 is characterized by one or several large explosions, associated with high thermal and seismic amplitudes and durations, indicating the destruction of the impermeable cap created during phase 1. Phase 3 is characterized by passive, unhindered degassing indicating entirely open vent conditions while phase 4 sees the episodic bursting of presumably isolated gas slugs at the surface. The entire sequence is repeated twice in a two-hour observation period suggesting a cyclic oscillation between plugged and open vent configurations at El Reventador. The similarity with thermal and seismic waveforms from other classic Strombolian and Vulcanian (VEI 2 through 4) systems suggests the operation of common and globally applicable degassing and explosive processes that cause caps to develop and decay, thereby driving changes in eruption style.

Chapter Three: Plume ascent dynamics

The dynamics of eruptive plumes tracked by high resolution thermal infrared imaging

3.1 Introduction

Volcanic explosions release large amounts of energy in short periods of time, producing plumes that are a mixture of volcanic gas and clasts. Many attempts have been made to understand the dynamics of volcanic plumes (e.g., Morton et al. 1956; Patrick 2007; Cerminara et al. 2015), as well as their genesis and the spatial distribution of the material ejected (e.g., Sparks et al. 1992; Bonadonna and Phillips 2003; Parra et al. 2016). Studies aiming to describe the dynamics of volcanic plumes are based on observation, emphasizing imagery techniques that work in different ranges of the electromagnetic spectrum, such as pictures and video in the visible range (e.g., Wilson and Self 1980; Formenti et al. 2003; Bernard 2018), in the infrared (e.g., Harris and Ripepe 2007; Spampinato et al. 2011; Valade et al. 2014), in the ultraviolet (e.g., Kern et al. 2013; Peters et al. 2015; McGonigle et al. 2017), or radar using light (LiDAR, c.f. Platt et al. 2015) and radio waves (e.g., Weill et al. 1992; Donnadieu et al. 2005; Gouhier and Donnadieu 2008). Volcanic plumes are composed of an initial jet part, where the plume ascent is driven by its momentum, a thermal region where the dynamics is governed by convection and buoyancy, and an umbrella region where the material spreads laterally (e.g., Sparks 1986; Woods 1988). Morton et al. (1956) studied the behaviour of convective plumes and proposed a model in which the plume rises by buoyancy in a stratified atmosphere considering the mixing and heating of the ambient air. The simplicity and robustness of his model converted it into one of the most widely used models to this day to describe a series of explosive events ranging from geysers to Plinian eruptions (e.g., Mastin 1995; Woods 1988). Subsequent authors have proposed models for describing the formation and decompression of the jet in the plume (e.g., Woods 1995; Woods and Bower 1995) and many others to describe the umbrella region and long scale spread of ash and gases in the atmosphere (Sparks 1986; Wilson and Walker 1987).

Strombolian and Vulcanian eruptions, although much smaller than Plinian events, occur with high frequency, so their comprehension is of great importance in risk mitigation. When applying the theoretical models described above, some aspects of scale have to be taken into account, for example the assumption that gas expansion during a volcanic explosion is isothermal is valid when a large amount of heat is available, as is the case in sustained eruptions, otherwise, the heat exchange between solids and gas is so low that the gas expansion is likely to occur adiabatically (Mastin 1995; Parfitt and Wilson 2008). In the case of steady explosive eruptions, for instance Plinian eruptions, the height of the plume generated depends on the vertical temperature gradient in the surrounding air (Settle 1978). In transient eruptions, by contrast, the height of the plume depends on the total mass of erupted material, or the rate of mass release. This second case occurs when the explosions are not far enough

apart in time that the pyroclastic cloud cannot disperse before the next explosion occurs (Parfitt and Wilson 2008).

In this work we analyse the thermal data recorded during Strombolian to Vulcanian explosions at Reventador volcano by measuring the dynamic parameters of the plumes generated and compare the results with theoretical models, providing statistical information that allows us to better understand their applicability to smaller eruptive plumes. We also describe the evolution of the explosive activity of Reventador during the period between 2017 and 2023 and analyse the possible causes of the changes.

3.2 Plume model

The theoretical model we use as the basis to describe the plume in this study is the one proposed by Woods (1988), considering the plume as a multi-phasic mixture of ash particles and gas that incorporates the surrounding air as it rises. The plume velocity is considered positive upwards, there is no ash fallout during the ascent of the plume and the ballistics are not part of the plume. It is assumed that at least 90% of the solid particles in the plume are smaller than 5 mm in diameter, which traduces as a thermal equilibrium between solids and gas through a horizontal profile. Horizontally, the properties of the plume are represented by an averaged value following a top-hat function (Woods 1995b; Cerminara et al. 2015). The solid phase is uncompressible and chemically inert (c.f. Mastin 1995), which makes addable the volumes of the solids (Vs) and the gases (Vg) in any instant. In the model, the umbrella region is considered part of the convective region, the plume is therefore composed of a jet region and a convective region. Table 1 details the nomenclature used in this work. For a detailed description of the model, see Woods (1988).

Table 3. Nomenclature used in this document.

Notation (The 0 subscript denotes the parameters evaluated in the vent zone)	
α	Atmospheric density
β	Plume bulk density
ρ_s	Standard density of a mercury column; 1.24 kg m^{-3}
σ	Density of the solid pyroclastics; 1 300 kg m^{-3}
θ	Temperature of the plume
θ_a	Temperature of surrounding air
h	Height of the upper limit of the plume
h_b	Height of transition to buoyant regime
L	Radius of the plume
m_s	Mass of solid phase
m_g	Mass of gas phase
m_β	Bulk mass
n	Gas mass fraction
n_c	Solids content
P	Atmospheric pressure

P_s	Atmospheric pressure at sea level; 101 300 Pa
R	Universal gas constant; 8.314 x 10^3 N m $kmol^{-1}$ K^{-1}
R_a	Specific gas constant for the air; 285 J kg^{-1} K^{-1}
R_m	Specific gas constant for the volcanic gas; 462 J kg^{-1} K^{-1}
U	Bulk vertical velocity of the plume
V_s	Volume of solid phase in the plume
V_g	Volume of gas phase in the plume
V_β	Bulk volume of the plume

The bulk density (β) of the plume is variable with height and it is expressed by equation (3) of Woods (1988) as follows

$$\frac{1}{\beta} = \frac{1-n}{\sigma} + \frac{n\,R_g\,\theta}{P} \quad (1)$$

In this model, the bulk density is combined with the gas mass fraction (n) and the specific gas constant (R_g) as

$$n = 1 + (n_0 - 1)\frac{L_0^2\,U_0\,\beta_0}{L^2\,U\,\beta} \quad (2)$$

$$R_g = R_a + (R_{g0} - R_a)\left(\frac{1-n}{n}\right)\left(\frac{n_0}{1-n_0}\right) \quad (3)$$

The value of n is also variable along the height of the plume, since it increases as ambient air is introduced into the plume. At the moment of jet decompression out of the vent, the value of the gas mass fraction n_0 has been estimated in the range between 0.01 and 0.06 for silicic magmas (Wilson and Self 1980; Woods and Bower 1995). However, values up to 0.38 were estimated when there is a gas accumulation under a rock cap at the top of the conduit (Parfitt and Wilson 2008). The pressure of the gas inside the plume is considered the same as that of the surrounding air (Woods and Bower 1995), depending only on the altitude. The point where the plume passes from a momentum-dominated to a buoyancy regime, when the plume has a height h_b, the bulk density of the plume equals the surrounding air density.

3.3 Methodology

In this work we used 32 frames-per-second (fps) infrared thermal video from volcanic explosions at Reventador volcano to estimate for each explosion the exit velocity, u; the height h of the plume front; the total volume V of the plume; the mass of the ash expulsed, m_r; and the mass of the gas released, m_g. We first take a detailed look at the dynamic of the eruptive plume revealed by high frequency imaging then look at the eruption parameters of a large number of eruptions over several years of observations.

3.3.1 Data acquisition

The thermal videos were recorded using an Optris PI 640 camera in individual measuring campaigns (see Table 4) and using the VIGIA imaging system (see Chapter One). During individual campaigns, thermal videos were recorded from two locations: the Azuela camp site and the Mirador site. Due to the distance to the crater, in the data recorded from Azuela the pixel size is 1.852 m while in those from the Mirador site, the pixel size is 3.113 m. In this dataset we have included the thermal videos analysed in Chapter Two. In all cases the optics used produced a field of view of 15°x11° and we used a GPS receiver connected directly to the computer in every recording session to keep the internal clock of the instruments synchronized with universal time, i.e., all time stamps in this document are in UTC unless explicitly stated otherwise.

Table 4. Thermal videos were recorded in five sessions during field measuring campaigns. *Videos from the campaign of February 2017 correspond to those included in chapter two

Date	Observation point	Latitude	Longitude	Altitude	Distance from the crater	Explosions recorded
2017.02.23-24*	Azuela	-0.0735	-77.617617	2119	4.50	13
2019.11.07-08	Mirador	-0.102511	-77.592626	1413	7.35	9
2020.02.07	Mirador	-0.102511	-77.592626	1413	7.35	3
2020.10.25-28	Mirador	-0.102511	-77.592626	1413	7.35	23
2020.10.27	Azuela	-0.0735	-77.617617	2119	4.50	11
2021.08.20-2023.01.01	VIGIA	-0.10198	-77.595592	1493	7.15	41

VIGIA system is a thermal and visible image-based instrument permanently deployed aiming to acquire thermal data from volcanic explosions, its technical and operational data were descripted in chapter one. In contrast to the individual campaigns, VIGIA captures videos in portrait layout, and is located 7.15 km from the active crater, obtaining a corresponding pixel size of 2.867 m. It has been operating regularly since August 2021.

In order to illustrate the proposed treatment of explosions, we have chosen a typical explosion of the Reventador volcano (E003), which is representative in terms of contrast with the background, duration, plume height and intensity. Having checked the dynamics of the plume generated in this explosion, we applied the methodology to the full data set and reviewed the variations.

3.3.2 Exit velocity

We calculated the exit velocity as the instantaneous velocity of the extruded material as close as possible to the crater (Sparks 1986). Following the method of (Harris and Ripepe

2007b), we placed a region of interest (ROI) on the visible crater rim to generate a thermal timeseries tracking the changes of temperature due to the transit of pyroclastics and gas. A second ROI directly above the first one allows to measure the time it takes the expulsed material to traverse from the first to the second ROI. This lag was calculated as the difference between the points of maximum gradient in the lower ROI and its corresponding in the upper ROI (Figure 23). The vertical distance was obtained from the pixel size information for each case. The fact that the camera is aiming upwards produces a geometrical distortion that needs to be corrected (cf. Formenti et al. 2003; Harris 2013). We applied the correction to the vertical distance as described in the Appendix A. In the case of VIGIA and the measurements from Mirador, the difference between the measured distance and the actual distance is less than 5%, while the measurements from Azuela have a distortion of ~7.5%.

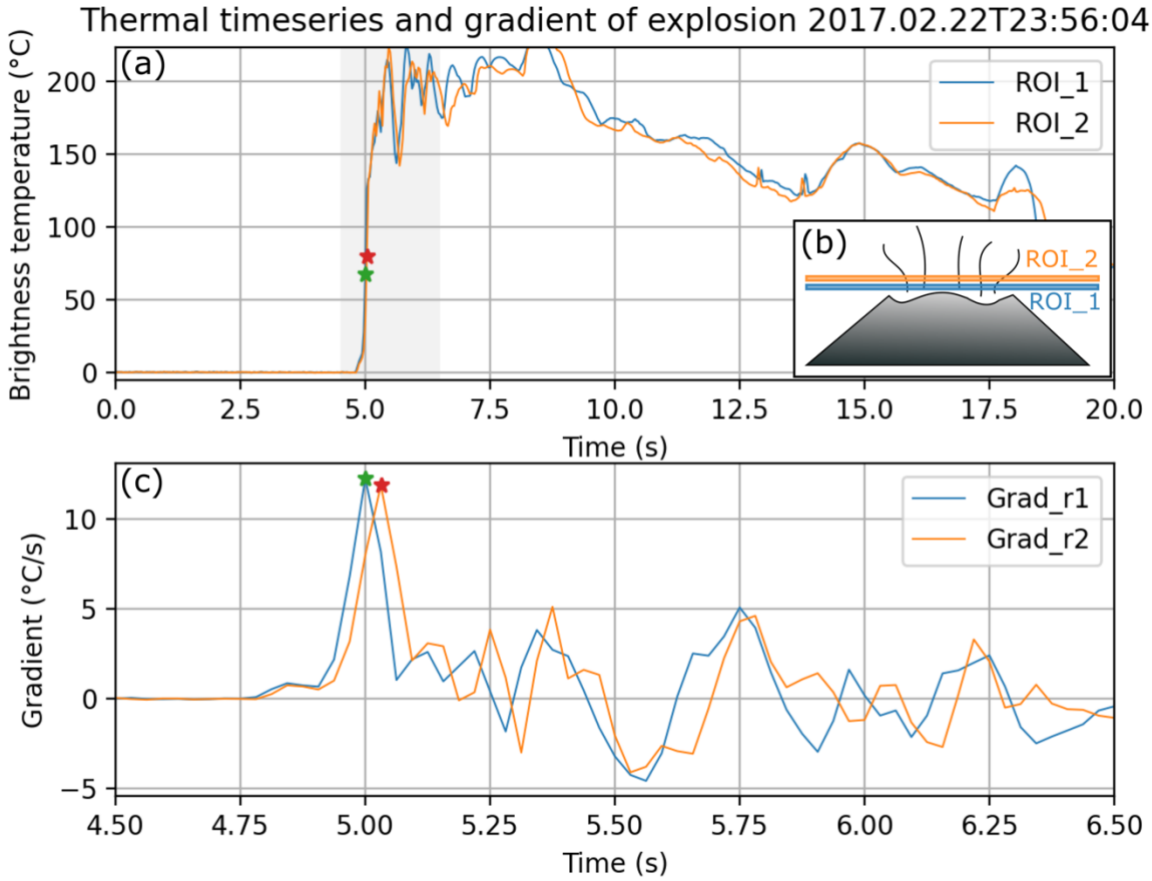

Figure 23. We are using (a) the timeseries corresponding to a region of interest on the top of the visible crater rim (ROI_1), and another (ROI_2) on the top of the earlier as shown in the panel (b). The gradient calculated for both timeseries is shown in (c) and is used for the calculation of the lag, the horizontal difference between the peaks signalled with stars, which is proportional to the inverse of the exit velocity. The gradient showed in panel (b) correspond to the shaded zone of panel (a)

3.3.3 Height

In order to track the vertical displacement of the plume, we constructed a stacked image of the vertical temperature distribution. In analogy to the column projection proposed by Pang and Liu (2001), we compiled a column with the maximum temperatures of each row in a given frame an then stacked horizontally the compiled columns for each frame of the video. The resulting stacked image (Figure 24) represents the temporal evolution of the temperature across the columns of the thermal video. For example, the height of the plume at each instant is represented in the upper border, pointed by the green arrows in Figure 24. We applied the Canny edge detector (Canny 1986), as implemented in OpenCV, to directly extract the temporal evolution of the plume height from the stacked image. We used the pixel size information and the correction described in Appendix A to report the height measured with respect to the summit. The derivative (tangent) of the height provided the instantaneous velocity of the plume front.

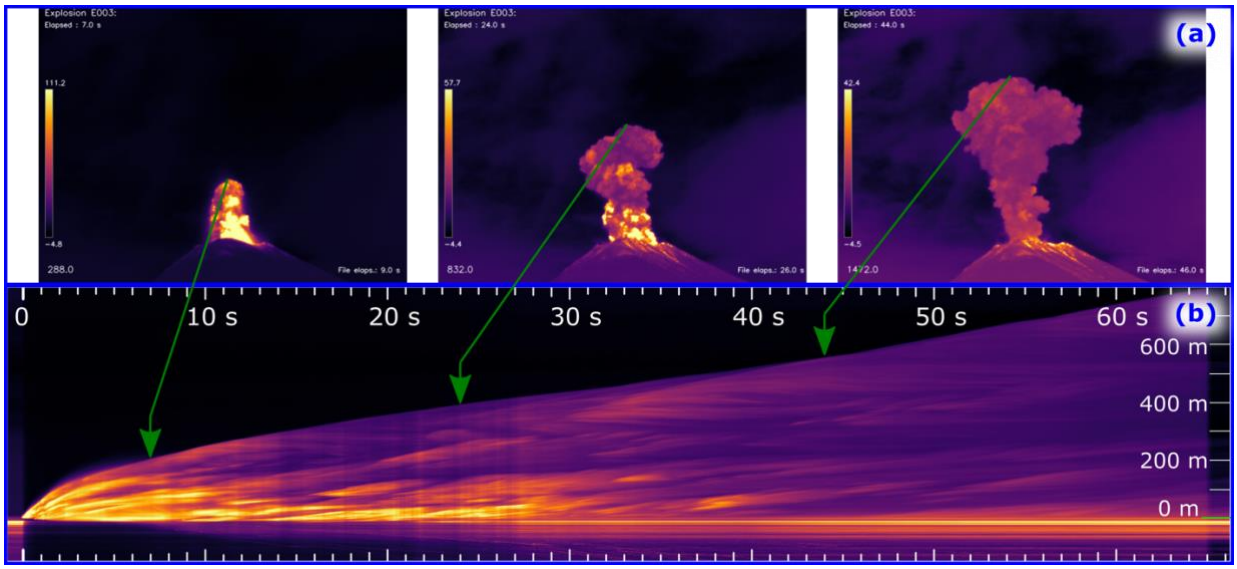

Figure 24. Each column of this image contains the maximum temperature of each row of an individual frame of the thermal video. Panel (a) shows captures of the frames at three different instants, that are represented by vertical lines of the image in panel (b). Then, the image represents the temporal evolution of the plume generated in the explosion E003. The horizontal axe of the figure contains the time while the vertical axis shows the height in meters above the summit. The green arrows show the temporal evolution of the plume front height.

3.3.4 Plume volume

The bulk volume of the plume changes with time and with height. We calculated the volume of the erupted material before the incorporation of air to the plume and, in a second instance, when the plume is in the convection zone. Firstly, we defined individual slices of the plume in each frame as the portion of the plume contained inside the ROI_1 (see Figure 25).

The volume of individual slices, that have disc shape due to the radial symmetry assumed (cf. Valade et al. 2014), were summed up through the duration of the explosion. Subsequently, a second ROI (ROI_2 in Figure 25) located nearly 100 m upwards allowed us to calculate the volume in the convective region, providing the entrainment coefficient, which is the ratio of horizontal to vertical expansion $\Delta L/\Delta h$ (Sparks 1986)

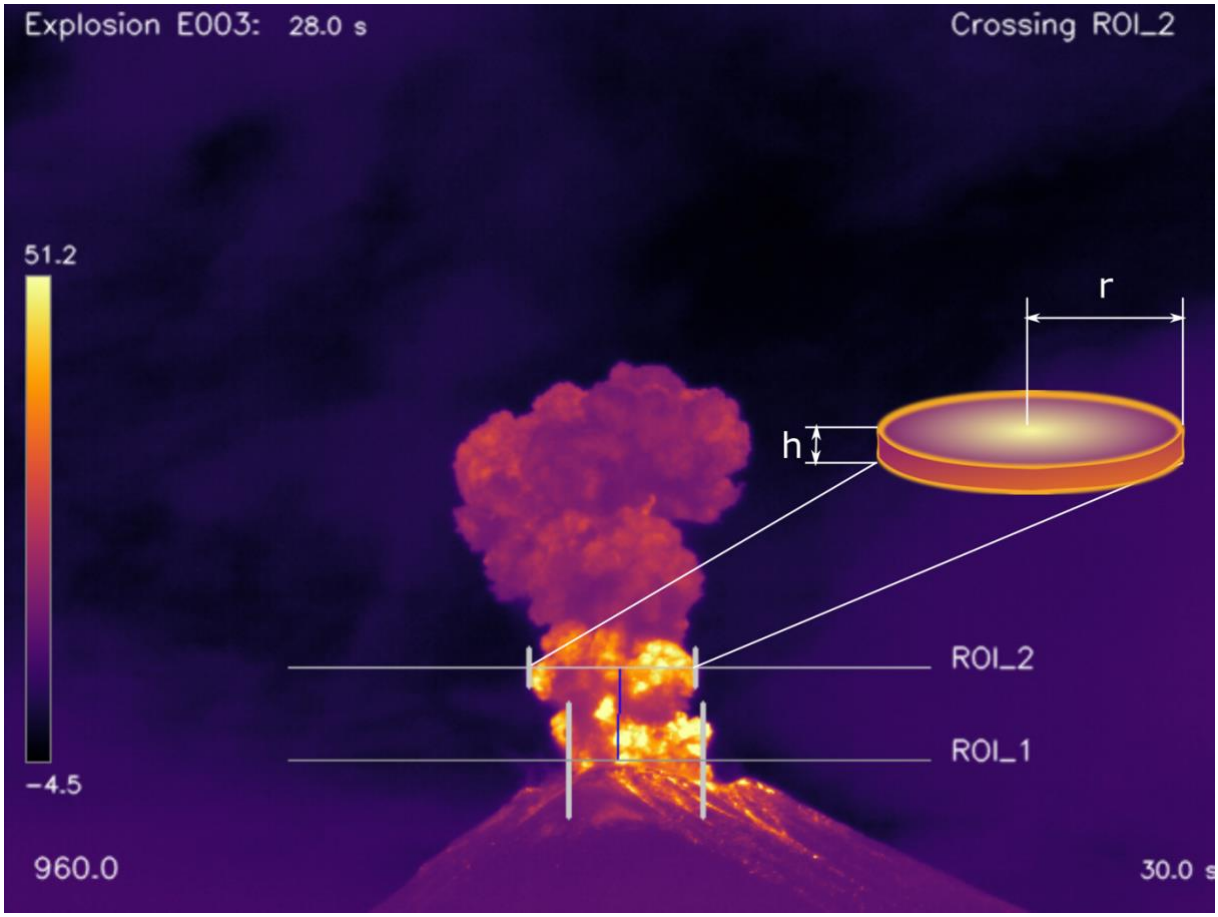

Figure 25. The portion of the plume contained within a ROI is considered as the diameter of a disc, assuming radial symmetry. The thickness of the disc is the pixel size, as the ROI is one-pixel thick. The vertical blue line in the figure crosses the centres of mas of the two ROIs.

3.3.5 Ash and gas mass

At a given height, the maximum temperature measured in a horizontal profile is considered to be the plume temperature, since outer layers of cold material are likely to mask the actual innermost temperature (cf. Cerminara et al. 2015; Matsushima 2005). From the plume model described in section 1.1, we calculated the bulk density in the vent zone (β_0) using equation (1) needing the gas mass fraction at the vent as input.

$$\frac{1}{\beta_0} = \frac{1 - n_0}{\sigma} + \frac{n_0 R_m \theta_0}{P_0} \quad (4)$$

As the bulk density of the plume equals the atmospheric density at the regime transition point, the fraction of solids in the plume n_c can be calculated as (Sparks 1986)

$$n_c = 1 - \frac{\theta_a}{\theta} \quad (5)$$

Then, combining equations (1) and (3) we obtained the value of n_0. The density of the solids in the plume is 1300 kg m^{-3} (cf. Bernard et al. 2016; Bernard 2013); the temperature was obtained by correcting the brightness temperature with the radiation absorption of the atmosphere (Harris 2013; see Appendix B) and the atmospheric pressure was calculated as

$$P = P_s e^{-\frac{\rho_s}{P_s} g h} \quad (6)$$

3.4 Results and Discussion

3.4.1 A detailed look at the plume ascent dynamics

Plumes generated in different explosions show a variety of maximum plume heights, ascent velocities, and ejected masses. However, the fundamental processes governing the rise of the plumes are the same. We have observed the explosion E003 (Figure 26) closely to describe the dynamics of its ascent. The plume generated in this explosion is completely identifiable, i.e., there are no clouds, ash or obstacles that prevent us from observing it in its full size during the first 65 s, until the leading edge reaches the border of the field of view. The complete duration of the explosion was 144 s. This explosion occurred at 23h56 (18h56 local time), at this time in Ecuador the sun is already set, which significatively reduces the incidence of direct solar radiation on surfaces. At the beginning of the explosion, the jet section is observable, which detaches from ballistics after a few seconds (Figure 26a-c). During these first seconds, the highest temperature is measured at the base of the jet and the column changes its shape from elongated to mushroom shaped (Figure 26b-c). As the column rises, portions of warmer material sporadically appear at the outer lateral part at different heights (Figure 26d-h), then gradually cool down to the temperature of the rest of the column. The plume height evolution is shown in Figure 27a, and the plume front velocity change over time and height in Figure 27b-c. As mentioned before, the column overpassed the edge of the field of view (Figure 26i), so we cannot report its final height accurately, but only know that it reached a height greater than 800 m above the summit. The maximum velocity measured during this explosion was 59.3 m s^{-1}, when the jet first appears (Figure 26a). As the explosive event

progresses the velocity asymptotically takes the value of 10.8 m s^{-1}. This velocity was reached 42 s after the explosion started (Figure 26h) and its height was 540 m at that instant.

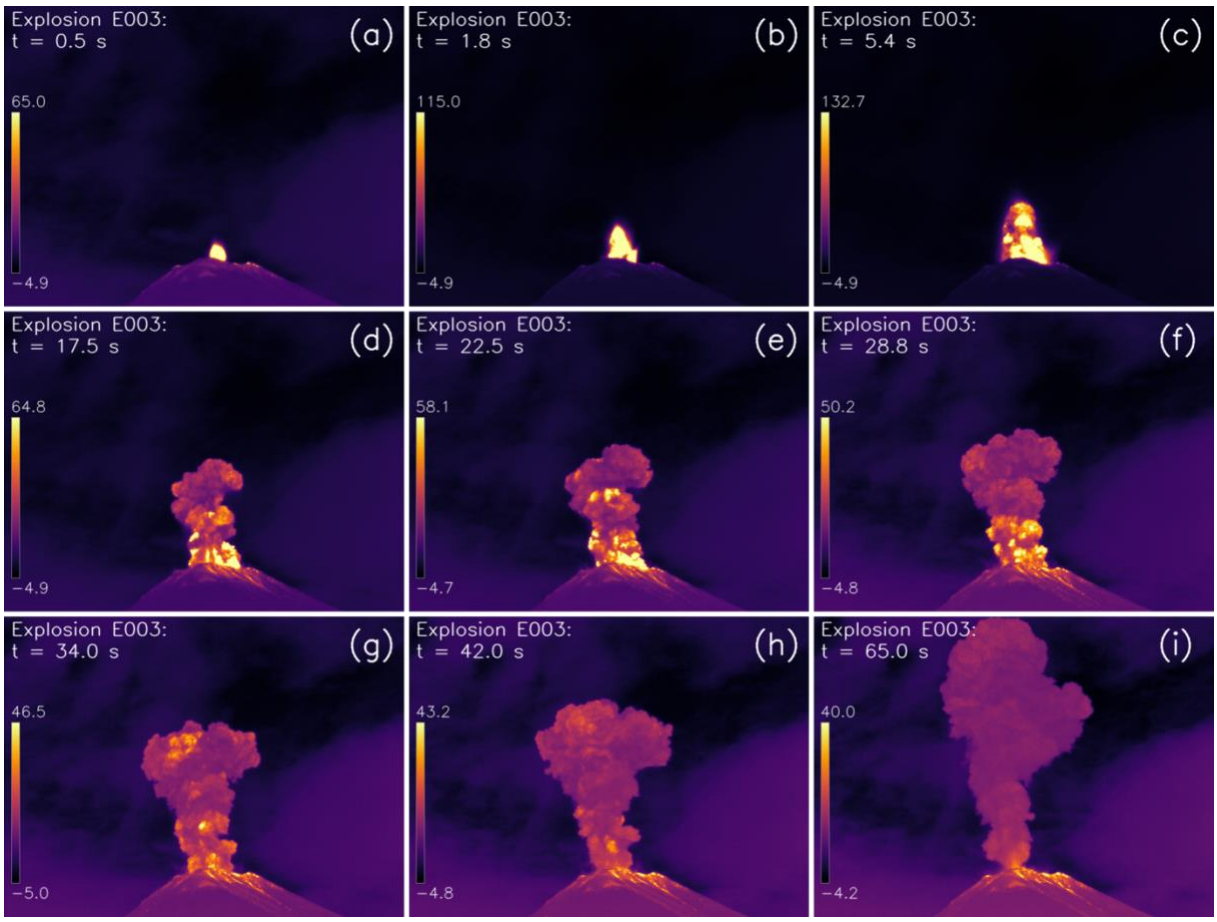

Figure 26. Evolution of the explosion E003. Each panel shows its colour scale and elapsed time since the beginning of the explosion.

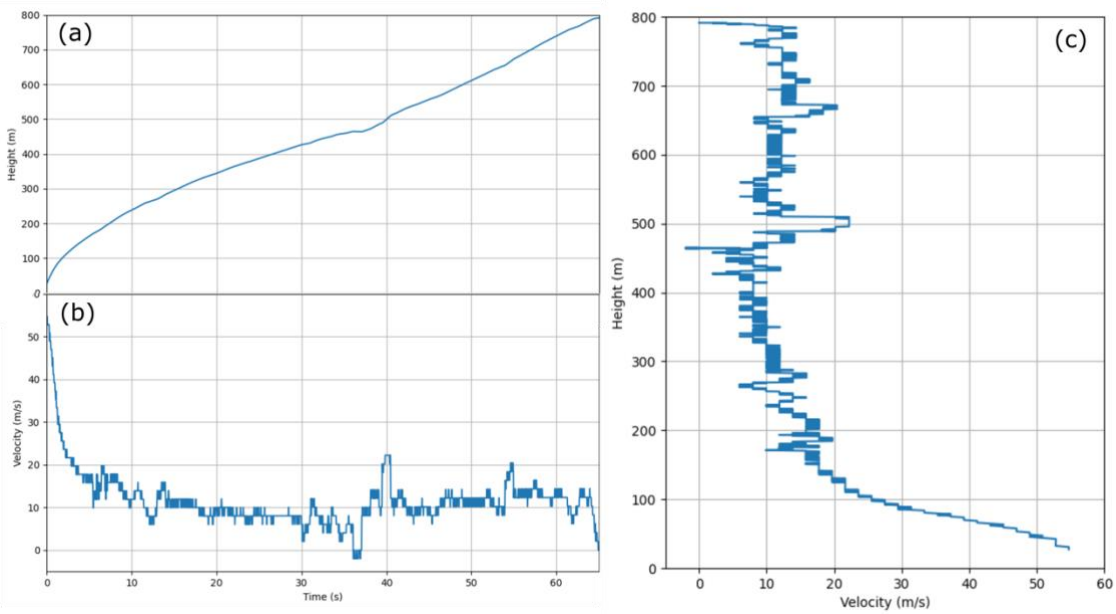

Figure 27. (a) The temporal evolution of the plume height and (b) plume front velocity corresponding to the explosion E003. Panel (c) shows the front velocity as a function of the height for the same explosion.

Looking in detail at the plume ascent shown in Figure 27a, variations in the slope of the height-versus-time curve are observed shortly before second 40, when the plume height is about 450 m above the summit. Possible causes for this variation are a change in the horizontal direction of the plume, or a change in the rate of ascent. The corresponding video shows no appreciable bending of the plume around this time, so the first option is discarded. Instead, the variations in the velocity of the front appear to be due to a secondary plume generated after the start of the eruption, but which rises faster and catches up with the primary plume. This is also reflected in the velocity of the front (Figure 27b,c), with slight oscillations accompanied by a general acceleration of the plume from second 37 onwards. Panels (g) to (i) in Figure 26 show a portion of the plume reaching the leading front and overpassing its height. Following the development of the plume in Figure 26, the portions of secondary plumes generated by pulses after the first burst appear in the lateral surface of the column clearly visible in Figure 26d-f (cf. Johnson et al. 2004). This behaviour was observed previously at Santiaguito volcano (Bluth and Rose 2004), in Guatemala, and were associated to a complex ring distribution of small vents that activate consecutively (Sahetapy-Engel and Harris 2009). The stacked image of the plume (Figure 28) also shows the effect of consecutive bursts, partially delimited in dashed lines. The cyan arrows in this figure represent the instantaneous velocity of the secondary plumes. Note that the exit velocity of the newly formed thermals decreases with time. Brightness temperature of the crater zone also decreases with time; combining this result with the relation between the plume temperature and the solids content fraction expressed in equation (5), we can infer that there is less gas available after each secondary burst. However,

the cases where the newly formed plume overtakes the already emerged plume cannot be explained by this reasoning. In these cases, the vents where both explosions originated may have independent gas storage systems beneath the vent or a larger amount of gas, e.g. a larger gas slug, may reach the surface after the first burst.

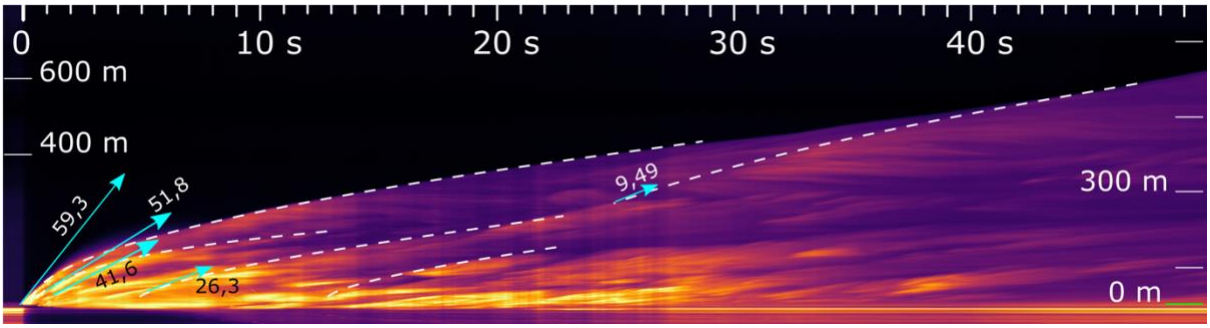

Figure 28. The main plume is composed of secondary plumes generated at subsequent bursts. The height of some secondary plumes is partially delimited by dashed lines and the instantaneous velocity represented with cyan arrows. The velocity, written next to the arrows, is expressed in m s^{-1} in all cases.

The entrainment coefficient accounts for the amount of air that is incorporated into the plume as it rises in the atmosphere, and is calculated as the shape ratio, measured horizontally versus vertically. In the jet zone, the plume is more elongated than wide, so the entrainment coefficient has low values. In the case of the E003 explosion, the first 10 s correspond to the initial jet zone (Figure 27a,b), then, the plume starts to ascend by buoyancy. Eventually, the lately generated thermals (cf. Patrick 2007) reach the front of the plume, returning the entrainment coefficient to low values. In this sense, the complex sequence of pulses makes the incorporation of air into the column also a complex process.

3.4.2 A statistical look at Reventador's eruptive behaviour

We analysed 80 explosions at Reventador volcano recorded on 74 thermal videos. The duration of these explosions varies between 16 and 375 s, averaging at 91 s. We measured exit velocities in the range 4.6 to 99 m s^{-1}, with a mean value of 30 m s^{-1}. The maximum height of the plumes was measured between 100 m and 1 280 m above the summit. The volume occupied by the ejected material, varies from 0.3 x 10^6 to 250 x 10^6 m^3 and we calculated the mass of the material between 2.2 x 10^6 and 125 x 10^6 kg for the solid phases, and between 0.3 x 10^6 to 8.5 x 10^6 kg for the gas phases. The reader can find a summary of the resulting dynamic parameters for the complete set of explosions in Appendix C.

Figure 29 shows the maximum plume heights, volume and ejected mass variations compared to those of the exit velocity (Figure 29-1), initial gas mass fraction (n_0) (Figure 29-2), and maximum corrected temperature at eruption onset (Figure 29-3). Distribution of the

explosions at Figure 29C1 suggested a separation in two groups, G1 and G2, shown with different colours in Figure 29. The coloured marks in all the panels of Figure 29 represent the same grouping.

1

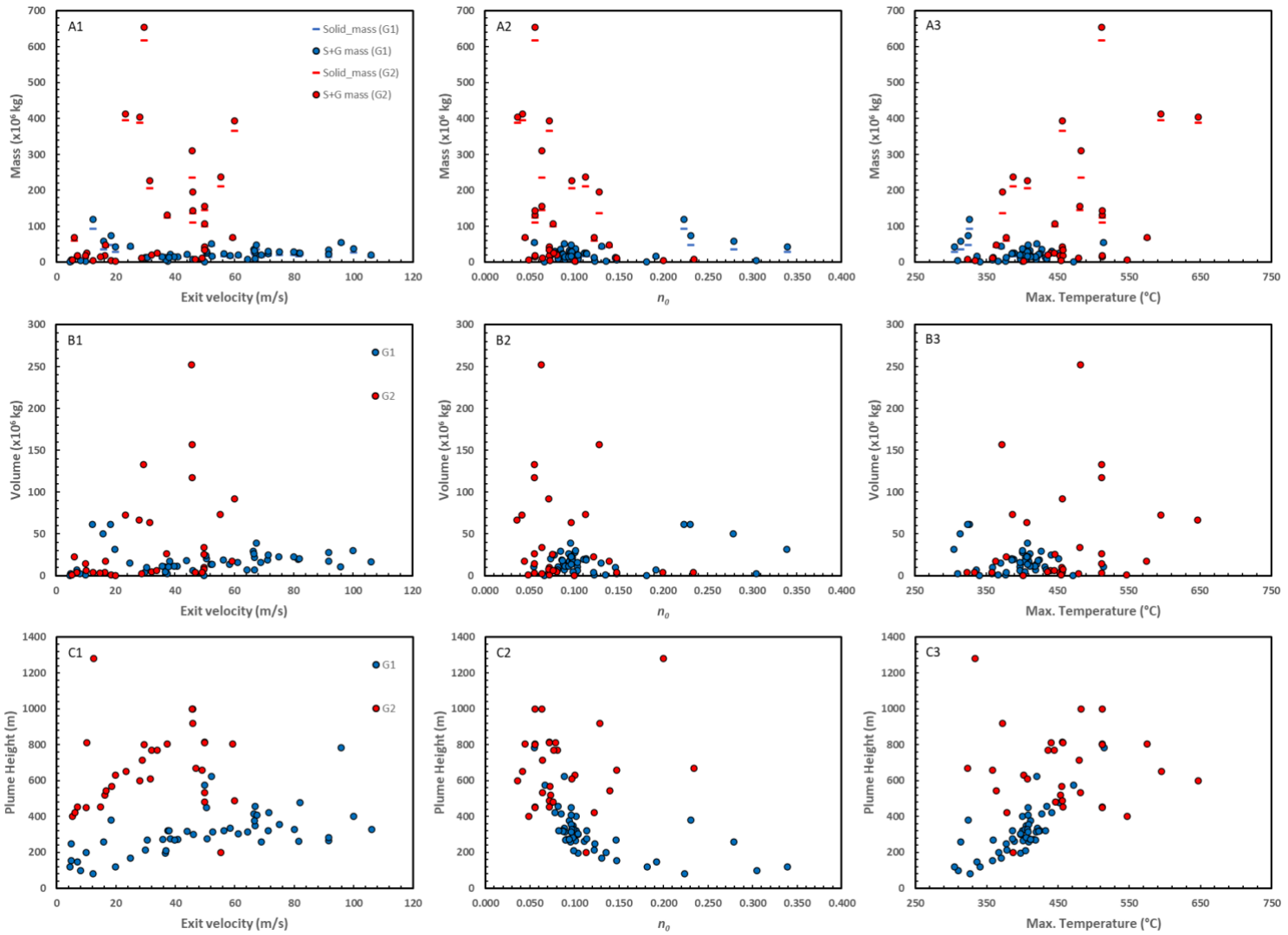

Figure 29. (A)Expulsed mass, (B) volume and (C) maximum plume height as functions of (1) exit velocity, (2) initial gas mass fraction (n_0) and (3) corrected maximum temperature at eruption onset.

The explosions belonging to the group G2 raised higher than those of group G1, regardless of the exit velocity. Still about the dependency on the exit velocity, the ejected mass of the explosions belonging to group G1 remain in a more limited and lower range than those of explosions of group G2. Explosions belonging to the first group show higher exit velocities than those from the second group. In general, temperatures recorded during explosions belonging to G2 are higher than those recorded in explosions of G1. And the variation of the maximum height of the plume, the bulk volume and the expulsed mass extends over a wider range for G2 explosions than those of G1. By the contrary, explosion of group G2 occur with lower values of n_0 (Figure 29-2), meaning that the content of solids is higher in these eruptions. This is also reflected in the expulsed mass; explosions of G2 present the higher values of mass in all cases (Figure 29d-f). The group G2 contains explosions catalogued as Type A in chapter two, which were related to Vulcanian activity.

For both groups, the maximum height reached by the plume is higher at lower values of n_0. This is consistent with the idea that a lower initial gas fraction means relatively more solid material in the mixture, which contributes more heat during ascent than gas would, ultimately allowing the plume to rise higher. Similarly, when higher temperatures are observed during the explosion onset, the plume will rise higher than explosions showing lower temperatures (Figure 29b). In addition, explosions showing initial high temperature are those where a higher amount of mass was measured.

	θ_0	U_0	V_β	h_{max}	U_b	t_b	h_b	n_0	ms	mg	m_β
θ_0	1,0000	0,1104	0,2008	0,4686	0,2252	0,5398	0,5512	-0,8097	0,4706	0,0643	0,4445
U_0	0,1104	1,0000	0,0696	0,0063	0,3581	-0,0833	0,2011	-0,3179	-0,0456	0,0611	-0,0355
V_β	0,2008	0,0696	1,0000	0,3610	0,1676	0,2239	0,4366	-0,0809	0,6835	0,9804	0,7433
h_{max}	0,4686	0,0063	0,3610	1,0000	0,2443	0,4646	0,5084	-0,3629	0,3245	0,2954	0,3346
U_b	0,2252	0,3581	0,1676	0,2443	1,0000	-0,0100	0,3651	-0,3083	-0,0552	0,1295	-0,0368
t_b	0,5398	-0,0833	0,2239	0,4646	-0,0100	1,0000	0,7637	-0,3729	0,4369	0,1761	0,4258
h_b	0,5512	0,2011	0,4366	0,5084	0,3651	0,7637	1,0000	-0,4428	0,4648	0,3922	0,4756
n_0	-0,8097	-0,3179	-0,0809	-0,3629	-0,3083	-0,3729	-0,4428	1,0000	-0,2440	0,0352	-0,2228
ms	0,4706	-0,0456	0,6835	0,3245	-0,0552	0,4369	0,4648	-0,2440	1,0000	0,6060	0,9961
mg	0,0643	0,0611	0,9804	0,2954	0,1295	0,1761	0,3922	0,0352	0,6060	1,0000	0,6735
m_β	0,4445	-0,0355	0,7433	0,3346	-0,0368	0,4258	0,4756	-0,2228	0,9961	0,6735	1,0000

Figure 30. Pearson correlation matrix for the parameters of the explosions of the Reventador volcano.

Figure 30 shows the correlations between the dynamical parameters of the Reventador volcano explosions as quantified by Pearson correlation coefficients. More specifically, the parameters compared are maximum (corrected) temperature, exit velocity, bulk volume, maximum height of the front, buoyancy velocity, time to reach the buoyancy regime, height at

which the regime changed from gas-thrust to buoyancy, initial gas mass fraction, solid phase mass, gas mass and bulk mass of the plume (see Table 3). For each pair of parameters, a blue bar drawn to the right indicates a positive correlation while a red bar drawn to the left shows negative correlation. For example, we can see the evident correlations between the bulk and the solid phase masses, and a slightly lower correlation between the bulk and gas masses this decreasing reflects the idea that the gas mass is very little compared to the solids mass (e.g. Sparks 1986; Woods and Bower 1995). It is noticeable from Figure 30 that the gas mass fraction at the beginning of the explosion changes inversely with the other variables, presenting the strongest correlation with the maximum temperature. Another pair of positively correlated parameters are gas mass with the bulk volume, which supports the supposition that the solid phase volume is depreciable compared to the volume of the gas phase (Wilson 1976; Woods 1988).

Some differences in the correlations appear when separating the explosions into the groups G1 and G2 proposed above (Figure 31). For example, the correlation between the maximum (corrected) temperature (θ_0) and the maximum height (h_{max}) of the plume is appreciable for group G2 (Figure 31), but it is weak in the general case (Figure 30) and it even gets negative for group G1 (cf. Figure 29).

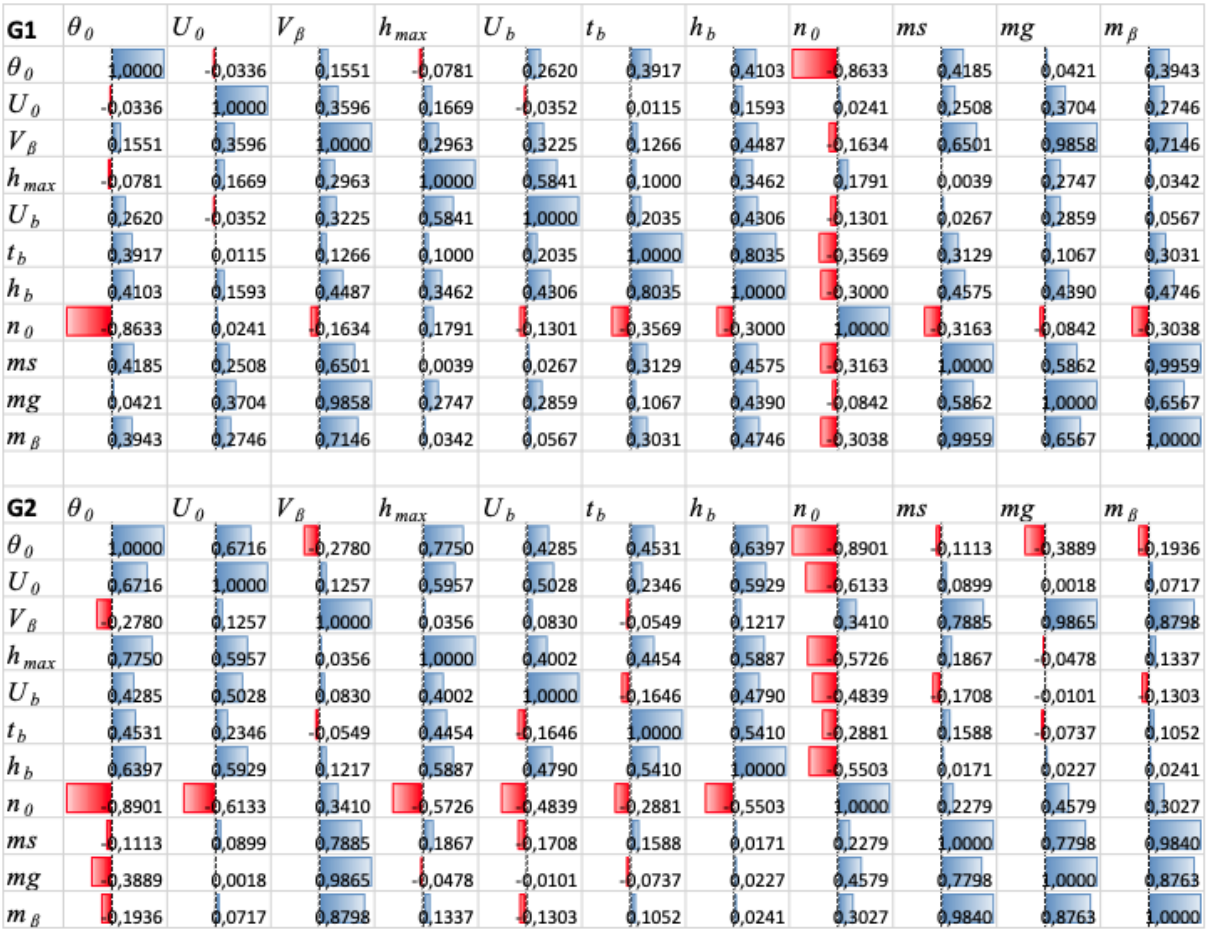

G1	θ_0	U_0	V_β	h_{max}	U_b	t_b	h_b	n_0	ms	mg	m_β
θ_0	1,0000	-0,0336	0,1551	-0,0781	0,2620	0,3917	0,4103	-0,8633	0,4185	0,0421	0,3943
U_0	-0,0336	1,0000	0,3596	0,1669	-0,0352	0,0115	0,1593	0,0241	0,2508	0,3704	0,2746
V_β	0,1551	0,3596	1,0000	0,2963	0,3225	0,1266	0,4487	-0,1634	0,6501	0,9858	0,7146
h_{max}	-0,0781	0,1669	0,2963	1,0000	0,5841	0,1000	0,3462	0,1791	0,0039	0,2747	0,0342
U_b	0,2620	-0,0352	0,3225	0,5841	1,0000	0,2035	0,4306	-0,1301	0,0267	0,2859	0,0567
t_b	0,3917	0,0115	0,1266	0,1000	0,2035	1,0000	0,8035	-0,3569	0,3129	0,1067	0,3031
h_b	0,4103	0,1593	0,4487	0,3462	0,4306	0,8035	1,0000	-0,3000	0,4575	0,4390	0,4746
n_0	-0,8633	0,0241	-0,1634	0,1791	-0,1301	-0,3569	-0,3000	1,0000	-0,3163	-0,0842	-0,3038
ms	0,4185	0,2508	0,6501	0,0039	0,0267	0,3129	0,4575	-0,3163	1,0000	0,5862	0,9959
mg	0,0421	0,3704	0,9858	0,2747	0,2859	0,1067	0,4390	-0,0842	0,5862	1,0000	0,6567
m_β	0,3943	0,2746	0,7146	0,0342	0,0567	0,3031	0,4746	-0,3038	0,9959	0,6567	1,0000

G2	θ_0	U_0	V_β	h_{max}	U_b	t_b	h_b	n_0	ms	mg	m_β
θ_0	1,0000	0,6716	-0,2780	0,7750	0,4285	0,4531	0,6397	-0,8901	-0,1113	-0,3889	-0,1936
U_0	0,6716	1,0000	0,1257	0,5957	0,5028	0,2346	0,5929	-0,6133	0,0899	0,0018	0,0717
V_β	-0,2780	0,1257	1,0000	0,0356	0,0830	-0,0549	0,1217	0,3410	0,7885	0,9865	0,8798
h_{max}	0,7750	0,5957	0,0356	1,0000	0,4002	0,4454	0,5887	-0,5726	0,1867	-0,0478	0,1337
U_b	0,4285	0,5028	0,0830	0,4002	1,0000	-0,1646	0,4790	-0,4839	-0,1708	-0,0101	-0,1303
t_b	0,4531	0,2346	-0,0549	0,4454	-0,1646	1,0000	0,5410	-0,2881	0,1588	-0,0737	0,1052
h_b	0,6397	0,5929	0,1217	0,5887	0,4790	0,5410	1,0000	-0,5503	0,0171	0,0227	0,0241
n_0	-0,8901	-0,6133	0,3410	-0,5726	-0,4839	-0,2881	-0,5503	1,0000	0,2279	0,4579	0,3027
ms	-0,1113	0,0899	0,7885	0,1867	-0,1708	0,1588	0,0171	0,2279	1,0000	0,7798	0,9840
mg	-0,3889	0,0018	0,9865	-0,0478	-0,0101	-0,0737	0,0227	0,4579	0,7798	1,0000	0,8763
m_β	-0,1936	0,0717	0,8798	0,1337	-0,1303	0,1052	0,0241	0,3027	0,9840	0,8763	1,0000

Figure 31. Pearson coefficient-based correlation matrix for dynamical parameters of explosions of the Reventador volcano separated in groups G1 and G2.

3.5 Conclusions

We have analysed a set of 80 Strombolian to Vulcanian explosions from Reventador volcano between 2017 and 2023. We used one explosion (E003) as a case study to describe in detail the dynamics of the plume generated. We observed that the plume is composed by a set of individual plumes formed during secondary bursts occurring in different small vents. The sum of the effects of individual explosions in the sequence can be roughly described by the theoretical model. We also measured the exit velocity, maximum temperature, velocity of the leading front, volume and entrainment coefficient of the plumes generated; and calculated, applying theoretical models, the initial gas mass fraction, the initial density and the mass of solids and gas expulsed during the explosions.

We observed in the dataset that the explosions can be separated into two groups. One of these groups contains smaller explosions catalogued as Strombolian. The second group includes Vulcanian explosions and those classified as Type A at chapter two.

General conclusions and perspectives

From the study of Strombolian and Vulcanian explosions we can draw some important conclusions. Strombolian and vulcanian explosions can occur in the same volcano changing in style in short periods of time (on the order of minutes to hours).

It is possible to characterise volcanic explosions recorded on thermal video, to classify them and to determine the dynamics of the plume generated. We have determined the characteristics of the explosions of the Reventador volcano and compared them to those of Stromboli, Santiaguito and Sakurajima volcanoes.

Short-term volcanic activity can manifest itself in phases that follow each other in a matter of minutes to hours. In the case of the Reventador volcano in February 2017, volcanic activity presented four phases that repeated twice in a 2-hour period.

The physical conditions of the shallow vent zone determine the dynamics of the ash and gas column generated during a volcanic explosion. These conditions include pressure, related to the amount of gas present; temperature; vent radius; degree of fragmentation, determining the gas versus solids mass ratio; among others.

Volcanic explosions are usually composed of a sequence of secondary outbursts that produce volcanic plumes that add up to each other. These secondary explosions may originate in different parts of the vent or in adjacent vents.

We used thermal infrared video of explosions and applied computer vision and other automated algorithms to detect, characterise and measure volcanic explosions. A set of computer scripts containing routines to perform these actions are openly available with the expectation that volcano observatories will adopt them and adjust them to their needs. In the same spirit, we published the information about the construction and functioning of the VIGIA instrument. The VIGIA instrument is already part of the volcano monitoring network of Instituto Geofísico of Escuela Politécnica Nacional, IGEPN, in Ecuador. There are some features that can be added to VIGIA in the relative short term, such as the publication of a webpage that allows the general public to interact with the cameras, obtaining personalised images of the monitored volcano. Other features and functions will require more dedicated work, and the interaction of more instruments, such as stereo reconstructions of volcanic plumes and synchronisation with seismic and acoustic (infrasound) signals.

Appendix

Appendix A: Vertical geometric correction

For a measuring setup where the camera is pointing upwards (cf. Harris 2013), the geometry can be represented as the Figure. The angle θ is the elevation angle of the camera; h is the real vertical distance, in our case it is the actual height of the plume; h' is the projection of the vertical distance in the image plane (DE).

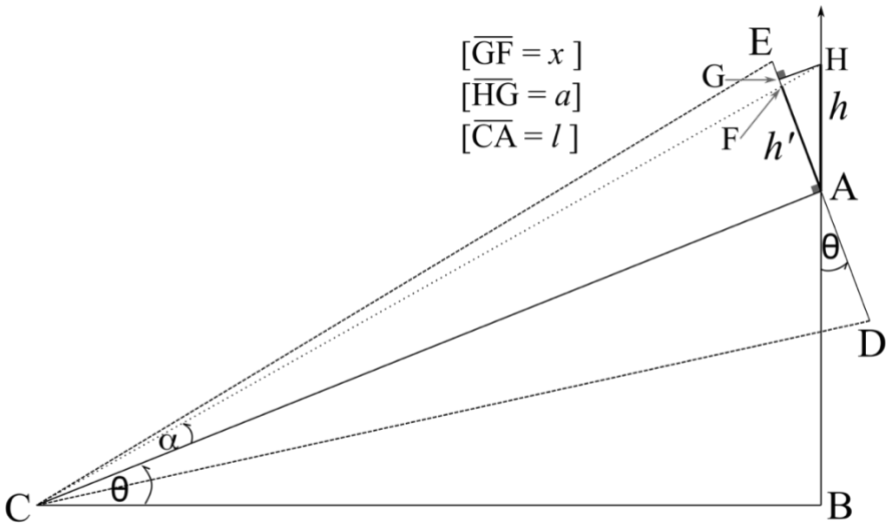

We will need the value of h when we know the value of *h'*. Then we can start pointing the fact that, in the right triangle AGH

$$h' + x = h\,cos\theta \quad \text{(A1)}$$

$$a = h\,sin\theta \quad \text{(A2)}$$

Now, since the segment CA is parallel to HG, the internal alternate angles ACF and FHG are congruent and have the value of α. In the triangles ACF and FHG, we will find, correspondingly, that

$$\frac{h'}{l} = \frac{x}{a} \quad \text{(A3)}$$

Then, replacing (A3) in (A1)

$$h' + \frac{a}{l}h' = h\,cos\theta \quad \text{(A4)}$$

And then, replacing (A2) in (A4)

$$h = \frac{1}{\frac{cos\theta}{h'} - \frac{sin\theta}{l}} \tag{A5}$$

Which provides the actual height of the plume, *h*, when knowing the projection in the image plane, *h'*; the distance between the camera and the centre of the plane, *l*; and the camera elevation angle, θ. The Figure shows the geometrical distortion produced in the 640-pixel vertical resolution image of a camera pointing upwards, due to different locations from the objective (elevation angle fixed to 15°), and due to the elevation angle (distance to the objective fixed to 7000 m).

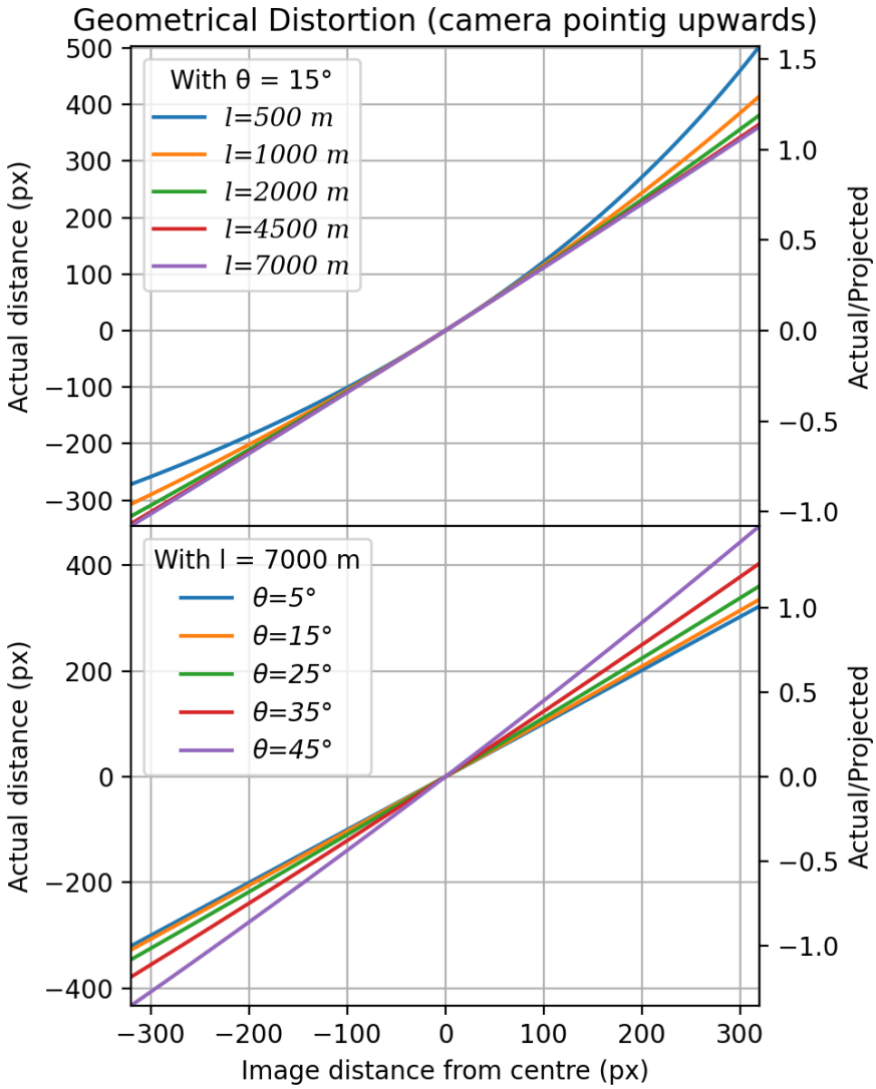

Appendix B: Temperature correction

Theoretical basis of radiometry[2] was proposed by Planck in his blackbody radiation law, which expresses the electromagnetic radiation emitted by an ideal body at a given wavelength. The Stefan-Boltzmann law allows the calculation of the radiant flux of the blackbody (Harris 2013; Kuenzer and Dech 2013) as

$$T_{RadBB} = \sigma\, T_{Kin}^4 \qquad \text{(B1)}$$

Where σ is the Stefan-Boltzmann constant (5.67 x 10^{-8} W m^{-2} K^{-4}) and T_{Kin} is the absolute kinetic temperature. When applying this idea to real radiators, it is necessary to introduce the concept of emissivity (ε), which is the fraction of the blackbody radiation at a given wavelength that can radiate from a real object. Then, for a real radiator we have that

$$T_{Rad} = \varepsilon^{1/4}\, T_{Kin} \qquad \text{(B2)}$$

Note that the emissivity depends on the wavelength, however, in this approximation we are using an averaged value for the electromagnetic band of interest (i.e., 8-14 μm). In contrast, the radiation for a given wavelength λ that the sensor of the thermal camera receives is (Harris 2013)

$$R_{in} = (\varepsilon\, \tau\, L_S) + L_R + L_U \qquad \text{(B3)}$$

In which τ is the atmospheric transmissivity; L_S is the spectral radiance emitted by the surface to be measured; L_R is the spectral radiance reflected by the surface and L_U is the spectral radiance emitted by the atmosphere (upwelling radiance). All these parameters are wavelength dependent. Transmissivity is related to the amount of radiation absorbed by the atmosphere absorbs and also depends on the altitude and the distance between the measured surface and the sensor.

Our interest is to find L_S, which is equivalent to knowing the real temperature of the measured surface. The re-arranged equation B3 states that

$$L_S = \frac{R_{in} - L_R - L_U}{\varepsilon\, \tau} \qquad \text{(B4)}$$

The values of τ, L_U, and L_R can be estimated using a model of the atmosphere based on MODTRAN (MODerate resolution atmospheric TRANsmission). Harris (2013) provides a look-up table with data for a standard US atmosphere (with rural aerosol profile and 23 km visibility) at different altitudes and ranges. For instance, in the case of Reventador, the altitude is above 3500 m and the distance between the sensor and the crater is about 5000 m (for measurements from Azuela camp site). Then, the transmissivity is 0.8248 and the up-welling

[2] For more details, see Section 0.2

radiance is 2.18 x 10^6 W m^{-2} m^{-1}. The value of the emissivity is taken as the mean of that reported for Fuego, Sakurajima and Santiaguito volcanoes (Williams and Ramsey 2019).

Appendix C: Summary of dynamical parameters of explosions at Reventador

Table C1. Parameters measured during explosion of Reventador volcano from 2017 to 2023

Explosion	Starting Date	Starting Time	Duration (s)	Max. Temp. (°C)	Exit Velocity (m s^{-1}	Volume (m^3)	Max. height (m)	Buoyancy velocity (m s^{-1})	Time to bouyancy (s)	Height of buoyancy (m)	n_0	Mass of solids (kg)	Mass of gas (kg)
2	20170222	23:31:30	65	453,3	16,35	4 358 118	520	8,1	18,2	200	0,073	17 126 447	1 356 353
3	20170223	23:56:09	128	575,0	59,3	17 822 987	804	10,8	42	540	0,045	65 787 698	3 069 831
4	20170223	23:59:11	34	377,3	4,9	914 455	250	7,8	3	25	0,123	2 441 931	342 316
5	20170223	00:15:18	59	512,3	14,8	3 038 202	452	7,8	22	222	0,056	14 129 492	836 243
6	20170223	00:16:17	42	457,1	7,1	4 169 414	454	7,9	16	186	0,072	16 599 388	1 286 915
7	20170223	00:17:14	31	366,7	9,9	915 174	200	7,9	11	107	0,136	2 245 707	352 534
8	20170223	00:23:59	130	512,4	37,3	26 707 000	804	13	34	240	0,056	124 231 499	7 349 408
9	20170223	00:57:04	120	479,5	28,8	2 376 345	714	10,8	29,6	270	0,064	10 149 528	699 034
10	20170223	01:00:38	74	455,0	18,47	972 950	570	10,4	34	154	0,073	3 845 971	301 690
11	20170224	01:03:08	61	547,2	5,3	1 278 843	400	6,5	27	150	0,049	6 400 132	329 470
12	20170225	01:17:47	36	378,0	29,9	4 379 931	215	5,2	16	106	0,122	11 759 117	1 636 381
13	20170226	01:25:19	45	378,0	6,1	22 685 382	421	5,1	23	120	0,122	60 904 541	8 475 459
14	20191107	22:16:28	68,7	358,3	5	2 532 884	155	2,48	6,5	0	0,148	5 758 367	998 685
15	20191107	22:19:47	36,6	309,8	8,1	2 532 884	100	2,38	7,6	4,5	0,305	2 638 891	1 155 956
16	20191107	22:24:29	65,9	326,4	12,25	61 749 131	80	2,5	12	56	0,224	92 873 925	26 740 165
17	20191107	22:27:14	117,96	407,5	31,5	63 742 565	610	8,5	10,6	155	0,097	205 678 684	22 080 810
18	20191107	22:51:50	183,125	595,0	23,3	72 976 543	650	6,4	40,7	375	0,042	395 786 548	17 290 210
19	20191107	23:39:48	126,8	647,0	28,1	67 044 497	600	9,1	24	300	0,036	389 333 457	14 600 055
20	20191107	23:42:50	374,6	511,8	29,5	133 180 700	800	6,4	47	500	0,056	618 213 469	36 681 311
21	20191107	23:52:26	87	305,2	19,9	31 536 705	120	3	5	36	0,339	28 479 849	14 613 996
22	20191108	00:12:38	150	456,7	60	91 844 451	490	4	20	220	0,072	365 164 433	28 377 711
23	20200207	03:33:15	69,00	387,3	55,3	73 465 065	200	2,5	4,2	52	0,113	210 473 811	26 783 111

24	20200207	04:11:31	109,00	456,4	49,8	9 828 659	815	5,3	35,5	270	0,072	39 029 507	3 038 552
25	20200207	04:20:25	75,84	436,2	32,1	5 151 116	770	5,13	6,2	55	0,081	18 981 368	1 666 348
26	20200207	04:31:25	64,75	358,3	49,1	4 078 152	660	5,14	7,3	53	0,148	9 271 178	1 607 965
27	20200207	04:32:31	67,97	323,6	46,8	3 820 890	670	5,4	7,4	48	0,234	5 456 225	1 669 262
28	20201025	20:34:05	62,5	402,0	19,92	572 994	632	2,6	49	267	0,101	1 793 898	201 244
29	20201025	20:55:31	67	445,3	33,9	6 139 438	770	5,2	24	172	0,077	23 434 453	1 945 376
30	20201025	21:00:26	72	472,2	49,8	350 348	575	5,15	12	128	0,067	1 464 527	104 659
31	20201025	21:43:13	84,5	481,2	49,8	33 950 159	535	2,5	15,46	110	0,064	145 723 340	9 952 135
32	20201025	21:57:08	78,6	446,3	49,8	25 944 144	480	5,3	11,6	70	0,076	99 425 126	8 201 495
33	20201025	22:31:11	87	420,7	52,15	13 646 777	625	5,2	18	105	0,089	47 005 768	4 578 726
34	20201025	22:36:15	35,8	370,5	24,9	15 430 690	170	2,5	0	0	0,131	39 079 378	5 883 137
35	20201025	22:57:37	78,6	514,4	95,8	11 169 215	785	5,2	28	195	0,055	52 195 994	3 061 746
36	20201026	06:37:31	141,4	363,9	16,6	17 494 005	545	2,6	4,5	31	0,140	41 880 090	6 791 620
37	20201026	20:37:14	128,8	457,5	49,8	7 911 886	810	5,2	7,6	38	0,072	31 548 217	2 439 814
38	20201026	20:43:31	22,3	336,6	7,1	7 351 353	146	5,1	0	0	0,192	12 985 950	3 086 174
39	20201026	21:17:42	101,9	440,2	10,2	6 371 828	810	5,12	0	0	0,079	23 853 905	2 042 577
40	20201026	21:23:28	15,9	340,8	4,6	736 627	120	5,1	3,5	11	0,181	1 377 503	305 400
41	20210819	12:07:36	88,8	512,5	9,89	14 571 457	450	4,3	4,6	112	0,056	13 758 024	4 009 049
42	20211020	09:47:07	243,75	512,5	45,9	117 370 379	1000	10,7	14	260	0,056	110 817 322	32 292 164
43	20211022	08:50:34	278,4	482,8	45,6	252 333 908	1000	14	12,4	230	0,063	236 324 226	73 712 516
44	20220602	08:08:06	92	333,8	12,39	4 040 259	1280	13	7,8	200	0,200	3 232 703	1 710 682
45	20220602	09:52:34	107,3	372,6	45,9	156 862 262	920	8,9	40,2	600	0,128	136 729 184	59 467 211
46	20220707	12:24:09	56	314,1	15,9	50 147 532	260	4,8	11,8	108	0,279	36 164 405	22 575 909
47	20220707	12:42:47	42	359,1	30,5	10 021 049	270	13	0,88	14	0,146	8 553 060	3 941 883
48	20220816	08:38:37	46,75	324,4	18,35	61 583 969	380	9,2	6,3	80	0,231	47 358 801	26 834 202
49	20221223	10:44:30	30	397,6	36,64	10 772 458	195	5,4	10,7	94	0,104	9 650 109	3 825 469
50	20221223	12:29:03	30	401,0	91,7	27 695 224	266	7,2	3,9	85	0,102	24 882 759	9 749 915

51	20221223	22:34:58	30	389,1	81,6	19 654 559	262	5	18,14	46	0,111	17 467 525	7 132 501
52	20221223	23:51:35	30	400,7	37,5	2 679 357	320	5,7	20,38	253	0,102	2 406 609	943 992
53	20221224	00:10:43	30	421,2	58,4	14 177 169	335	7,2	20	265	0,088	12 922 831	4 750 755
54	20221224	00:36:25	30	409,4	68,9	16 218 573	260	6,2	14	156	0,096	14 666 654	5 592 384
55	20221224	04:09:14	30	427,6	66,5	29 207 844	415	10,7	15	269	0,085	26 724 755	9 640 962
56	20221224	04:19:52	30	386,6	50,7	20 286 331	277	6,9	12,5	200	0,114	17 982 325	7 409 872
57	20221224	04:25:20	30	386,1	56,4	19 212 392	320	8,6	9	165	0,114	17 021 008	7 027 167
58	20221224	05:13:01	30	410,2	38,3	17 681 277	275	8,2	9,2	114	0,095	15 999 164	6 084 252
59	20221227	00:03:34	30	424,6	71,3	19 257 352	320	9,5	3,3	80,6	0,087	17 590 497	6 400 477
60	20221227	00:09:21	30	405,3	91,7	17 351 176	282	9,2	9,1	103	0,098	15 642 825	6 043 416
61	20221227	00:24:49	30	397,7	46	6 063 379	300	9,8	6,8	92,5	0,104	5 432 151	2 152 632
62	20221227	00:42:37	30	452,2	82	20 756 498	478	16,6	9,7	284	0,074	19 223 848	6 476 403
63	20221228	04:13:00	30	419,5	64,3	6 791 397	316	8,8	12	165	0,089	6 184 079	2 284 902
64	20221228	03:53:41	30	441,5	71,4	25 189 447	422	10,1	11	235	0,078	23 217 510	8 049 901
65	20221228	04:17:42	30	416,4	40,8	11 960 767	272	6,83	8,8	140	0,091	10 869 100	4 054 532
66	20221228	04:42:23	30	404,6	36,8	5 168 807	210	6,2	5,4	62	0,099	4 657 253	1 803 569
67	20221228	05:44:32	30	423,1	44	18 125 686	317	8,7	10,4	155	0,087	16 541 171	6 046 771
68	20221228	06:45:55	30	418,7	39,7	11 631 917	270,4	10,1	16,6	146	0,090	10 586 107	3 921 301
69	20221228	06:49:11	30	432,7	37,9	10 682 677	322	9,17	12,16	166	0,082	9 802 238	3 484 253
70	20221228	06:57:56	30	412,0	35,7	11 604 067	273,4	10,2	13,6	128,8	0,094	10 513 412	3 975 733
71	20230101	01:01:49	30	405,6	66,8	22 250 921	350	7,3	11,7	217	0,098	20 064 857	7 743 975
72	20230101	01:11:59	30	400,7	100	30 117 257	400	9,3	8,7	205	0,102	27 051 539	10 610 923
73	20230101	01:25:34	30	408,6	50,5	24 088 899	450	10,9	5,6	170	0,096	21 770 470	8 323 268
74	20230101	01:41:29	30	411,3	66,7	26 217 015	376	13,5	5	92	0,094	23 740 672	8 998 416
75	20230101	02:06:37	30	434,5	66,8	7 426 204	457	11,6	7,7	180	0,082	6 820 551	2 412 182
76	20230101	03:00:51	30	408,8	75	22 744 970	357	9,3	6,6	153	0,096	20 559 088	7 854 870
77	20230101	03:38:35	30	404,0	106	16 625 872	330	14	4,1	150,5	0,099	14 972 910	5 810 379

78	20230101	04:33:04	30	408,3	67,4	38 816 564	410	11,2	5,2	175	0,096	35 075 227	13 418 917
79	20230101	04:41:32	30	397,4	61,2	15 896 744	305	7,3	6,05	115	0,104	14 237 879	5 648 172
80	20230101	05:04:19	30	407,2	80	22 793 644	330	8,1	10	201	0,097	20 578 916	7 902 149
81	20230101	05:25:07	30	407,8	52,5	13 659 058	314,3	8,1	10,8	130	0,097	12 337 764	4 728 030

Bibliography

Almeida M, Gaunt H, Ramón P (2019) Ecuador's El Reventador Volcano Continually Remakes Itself. Eos 100:. https://doi.org/10.1029/2019EO117105

Andò B, Pecora E (2006) An advanced video-based system for monitoring active volcanoes. Comput Geosci 32:85–91. https://doi.org/10.1016/j.cageo.2005.05.004

Arellano SR, Hall M, Samaniego P, et al (2008) Degassing patterns of Tungurahua volcano (Ecuador) during the 1999–2006 eruptive period, inferred from remote spectroscopic measurements of SO2 emissions. J Volcanol Geotherm Res 176:151–162. https://doi.org/10.1016/j.jvolgeores.2008.07.007

Arnold DWD, Biggs J, Anderson K, et al (2017) Decaying Lava Extrusion Rate at El Reventador Volcano, Ecuador, Measured Using High-Resolution Satellite Radar: DECAYING LAVA EXTRUSION AT EL REVENTADOR. J Geophys Res Solid Earth 122:9966–9988. https://doi.org/10.1002/2017JB014580

Aster R, MacIntosh W, Kyle P, et al (2004) Real-time data received from Mount Erebus Volcano, Antarctica. Eos Trans Am Geophys Union 85:97. https://doi.org/10.1029/2004EO100001

Bani P (2012) First estimate of volcanic SO2 budget for Vanuatu island arc. J Volcanol Geotherm Res 11

Bani P, Harris AJL, Shinohara H, Donnadieu F (2013a) Magma dynamics feeding Yasur's explosive activity observed using thermal infrared remote sensing: YASUR THERMAL SENSING. Geophys Res Lett 40:3830–3835. https://doi.org/10.1002/grl.50722

Bani P, Surono, Hendrasto M, et al (2013b) Sulfur dioxide emissions from Papandayan and Bromo, two Indonesian volcanoes. Nat Hazards Earth Syst Sci 13:2399–2407. https://doi.org/10.5194/nhess-13-2399-2013

Battaglia J, Hidalgo S, Bernard B, et al (2019) Autopsy of an eruptive phase of Tungurahua volcano (Ecuador) through coupling of seismo-acoustic and SO2 recordings with ash characteristics. Earth Planet Sci Lett 511:223–232. https://doi.org/10.1016/j.epsl.2019.01.042

Bernard B (2018) Rapid hazard assessment of volcanic ballistic projectiles using long-exposure photographs: insights from the 2010 eruptions at Tungurahua volcano, Ecuador. Volcanica 1:49–61. https://doi.org/10.30909/vol.01.01.4961

Bernard B (2013) Homemade ashmeter: a low-cost, high-efficiency solution to improve tephra field-data collection for contemporary explosive eruptions. J Appl Volcanol 2:1. https://doi.org/10.1186/2191-5040-2-1

Bernard B, Battaglia J, Proaño A, et al (2016) Relationship between volcanic ash fallouts and seismic tremor: quantitative assessment of the 2015 eruptive period at Cotopaxi volcano, Ecuador. Bull Volcanol 78:1–11. https://doi.org/10.1007/s00445-016-1077-5

Blackburn EA, Wilson L, Sparks RSJ (1976) Mechanisms and dynamics of strombolian activity. J Geol Soc 132:429–440. https://doi.org/10.1144/gsjgs.132.4.0429

Bluth GJS, Rose WI (2004) Observations of eruptive activity at Santiaguito volcano, Guatemala. J Volcanol Geotherm Res 136:297–302. https://doi.org/10.1016/j.jvolgeores.2004.06.001

Bogumil K, Orphal J, Homann T, et al (2003) Measurements of molecular absorption spectra with the SCIAMACHY pre-flight model: instrument characterization and reference data for atmospheric remote-sensing in the 230–2380 nm region. J Photochem Photobiol Chem 157:167–184. https://doi.org/10.1016/S1010-6030(03)00062-5

Bonadonna C, Phillips JC (2003) Sedimentation from strong volcanic plumes: SEDIMENTATION FROM VOLCANIC PLUMES. J Geophys Res Solid Earth 108:. https://doi.org/10.1029/2002JB002034

Brivio PA, Tomasoni R (1980) Thermal infrared continuous ground measurements in severe environment: A working data collection system. Proc 14th Int Symp Remote Sens Environ III:1731–1740

Calvari S, Di Traglia F, Ganci G, et al (2020) Overflows and Pyroclastic Density Currents in March-April 2020 at Stromboli Volcano Detected by Remote Sensing and Seismic Monitoring Data. Remote Sens 12:3010. https://doi.org/10.3390/rs12183010

Calvari S, Giudicepietro F, Di Traglia F, et al (2021) Variable Magnitude and Intensity of Strombolian Explosions: Focus on the Eruptive Processes for a First Classification Scheme for Stromboli Volcano (Italy). Remote Sens 13:944. https://doi.org/10.3390/rs13050944

Calvari S, Intrieri E, Di Traglia F, et al (2016) Monitoring crater-wall collapse at active volcanoes: a study of the 12 January 2013 event at Stromboli. Bull Volcanol 78:39. https://doi.org/10.1007/s00445-016-1033-4

Calvari S, Salerno GG, Spampinato L, et al (2011) An unloading foam model to constrain Etna's 11-13 January 2011 lava fountaining episode: THE 11-13 JAN 2011 ETNA'S LAVA FOUNTAIN. J Geophys Res Solid Earth 116:n/a-n/a. https://doi.org/10.1029/2011JB008407

Canny J (1986) A Computational Approach to Edge Detection. IEEE Trans Pattern Anal Mach Intell PAMI-8:679–698. https://doi.org/10.1109/TPAMI.1986.4767851

Capponi A, James MR, Lane SJ (2016a) Gas slug ascent in a stratified magma: Implications of flow organisation and instability for Strombolian eruption dynamics. Earth Planet Sci Lett 435:159–170. https://doi.org/10.1016/j.epsl.2015.12.028

Capponi A, Taddeucci J, Scarlato P, Palladino DM (2016b) Recycled ejecta modulating Strombolian explosions. Bull Volcanol 78:13. https://doi.org/10.1007/s00445-016-1001-z

Carter AJ, Ramsey MS, Belousov AB (2007) Detection of a new summit crater on Bezymianny Volcano lava dome: satellite and field-based thermal data. Bull Volcanol 69:811–815. https://doi.org/10.1007/s00445-007-0113-x

Cerminara M, Esposti Ongaro T, Valade S, Harris AJL (2015) Volcanic plume vent conditions retrieved from infrared images: A forward and inverse modeling approach. J Volcanol Geotherm Res 300:129–147. https://doi.org/10.1016/j.jvolgeores.2014.12.015

Chouet B, Hamisevicz N, McGetchin TR (1974) Photoballistics of volcanic jet activity at Stromboli, Italy. J Geophys Res 79:4961–4976. https://doi.org/10.1029/JB079i032p04961

Clarke AB, Esposti Ongaro T, Belousov A (2015) Vulcanian Eruptions. In: The Encyclopedia of Volcanoes. Elsevier, pp 505–518

Costa A, Macedonio G, Folch A (2006) A three-dimensional Eulerian model for transport and deposition of volcanic ashes. Earth Planet Sci Lett 241:634–647. https://doi.org/10.1016/j.epsl.2005.11.019

Davidson MW (2014) Pioneers in Optics: Johann Wilhelm Ritter and Ernest Rutherford. Microsc Today 22:48–51. https://doi.org/10.1017/S1551929514000029

Del Bello E, Lane SJ, James MR, et al (2015) Viscous plugging can enhance and modulate explosivity of strombolian eruptions. Earth Planet Sci Lett 423:210–218. https://doi.org/10.1016/j.epsl.2015.04.034

Delle Donne D, Lacanna G, Marchetti E, et al (2006) Monitoring Explosive Volcanic Activity Using Thermal Images, Stromboli Volcano, Italy. In: AGU Fall Meeting Abstracts. pp V43B-1795

Di Traglia F, Calvari S, D'Auria L, et al (2018) The 2014 Effusive Eruption at Stromboli: New Insights from In Situ and Remote-Sensing Measurements. Remote Sens 10:2035. https://doi.org/10.3390/rs10122035

Donnadieu F, Dubosclard G, Cordesses R, et al (2005) Remotely monitoring volcanic activity with ground-based Doppler radar. Eos Trans Am Geophys Union 86:201. https://doi.org/10.1029/2005EO210001

Dürig T, Gudmundsson MT, Dioguardi F, et al (2018) REFIR- A multi-parameter system for near real-time estimates of plume-height and mass eruption rate during explosive eruptions. J Volcanol Geotherm Res 360:61–83. https://doi.org/10.1016/j.jvolgeores.2018.07.003

DWSNET OÜ (2022) DWService. https://www.dwservice.net. Accessed 10 Feb 2022

Evocortex IRImager Direct SDK. In: Libirimager IRImagerDirect SDK. http://documentation.evocortex.com/libirimager2/html/index.html. Accessed 10 Feb 2022

Eychenne J, Le Pennec J-L, Troncoso L, et al (2012) Causes and consequences of bimodal grain-size distribution of tephra fall deposited during the August 2006 Tungurahua eruption (Ecuador). Bull Volcanol 74:187–205. https://doi.org/10.1007/s00445-011-0517-5

Fagents SA, Gregg TKP, Lopes RMC (2009) Modeling volcanic processes: The physics and mathematics of volcanism

Fagents SA, Wilson L (1993) Explosive volcanic eruptions-VII. The ranges of pyroclasts ejected in transient volcanic explosions. Geophys J Int 113:359–370. https://doi.org/10.1111/j.1365-246X.1993.tb00892.x

FLIR Systems (2004) ThermoVision A20 M Operator's manual

Formenti Y, Druitt TH, Kelfoun K (2003) Characterisation of the 1997 Vulcanian explosions of Soufrière Hills Volcano, Montserrat, by video analysis. Bull Volcanol 65:587–605. https://doi.org/10.1007/s00445-003-0288-8

Gaunt HE, Burgisser A, Mothes PA, et al (2020) Triggering of the powerful 14 July 2013 Vulcanian explosion at Tungurahua Volcano, Ecuador. J Volcanol Geotherm Res 392:106762. https://doi.org/10.1016/j.jvolgeores.2019.106762

Gonnermann HM, Manga M (2003) Explosive volcanism may not be an inevitable consequence of magma fragmentation. Nature 426:432–435. https://doi.org/10.1038/nature02138

Gouhier M, Donnadieu F (2008) Mass estimations of ejecta from Strombolian explosions by inversion of Doppler radar measurements. J Geophys Res 113:B10202. https://doi.org/10.1029/2007JB005383

Gurioli L, Colo' L, Bollasina AJ, et al (2014) Dynamics of Strombolian explosions: Inferences from field and laboratory studies of erupted bombs from Stromboli volcano: DYNAMICS OF STROMBOLIAN EXPLOSIONS. J Geophys Res Solid Earth 119:319–345. https://doi.org/10.1002/2013JB010355

Hall M, Ramón P, Mothes P, et al (2004) Volcanic eruptions with little warning: the case of Volcán Reventador's Surprise November 3, 2002 Eruption, Ecuador. Rev Geológica Chile 31:349–358. https://doi.org/10.4067/S0716-02082004000200010

Hall ML, Steele AL, Bernard B, et al (2015) Sequential plug formation, disintegration by Vulcanian explosions, and the generation of granular Pyroclastic Density Currents at Tungurahua volcano (2013–2014), Ecuador. J Volcanol Geotherm Res 306:90–103. https://doi.org/10.1016/j.jvolgeores.2015.09.009

Harris A (2013) Thermal Remote Sensing of Active Volcanoes: A User's Manual. Cambridge University Press

Harris A, Pirie D, Horton K, et al (2005) DUCKS: Low cost thermal monitoring units for near-vent deployment. J Volcanol Geotherm Res 143:335–360. https://doi.org/10.1016/j.jvolgeores.2004.12.007

Harris A, Ripepe M (2007a) Synergy of multiple geophysical approaches to unravel explosive eruption conduit and source dynamics – A case study from Stromboli. Geochemistry 67:1–35. https://doi.org/10.1016/j.chemer.2007.01.003

Harris A, Ripepe M (2007b) Temperature and dynamics of degassing at Stromboli. J Geophys Res 112:B03205. https://doi.org/10.1029/2006JB004393

Harris A, Ripepe M (2007c) Temperature and dynamics of degassing at Stromboli. J Geophys Res 112:B03205. https://doi.org/10.1029/2006JB004393

Harris AJ, Rose WI, Flynn LP (2003) Temporal trends in lava dome extrusion at Santiaguito 1922–2000. Bull Volcanol 65:77–89. https://doi.org/10.1007/s00445-002-0243-0

Harris AJL, Dehn J, Calvari S (2007) Lava effusion rate definition and measurement: a review. Bull Volcanol 70:1–22. https://doi.org/10.1007/s00445-007-0120-y

Harris AJL, Ripepe M, Calvari S, et al (2008) The 5 April 2003 Explosion of Stromboli: Timing of Eruption Dynamics Using Thermal Data. In: The Stromboli Volcano: An Integrated Study of the 2002–2003 Eruption. American Geophysical Union (AGU), pp 305–316

Harris AJL, Ripepe M, Hughes EA (2012) Detailed analysis of particle launch velocities, size distributions and gas densities during normal explosions at Stromboli. J Volcanol Geotherm Res 231–232:109–131. https://doi.org/10.1016/j.jvolgeores.2012.02.012

Harris AJL, Thornber CR (1999) Complex effusive events at K¯ılauea as documented by the GOES satellite and remote video cameras. Bull Volcanol 61:14

Herschel W (1800) Experiments on the refrangibility of the invisible rays of the sun. Philos Trans R Soc Lond 90:284–292. https://doi.org/10.1098/rstl.1800.0015

Hidalgo S, Battaglia J, Arellano S, et al (2015) SO2 degassing at Tungurahua volcano (Ecuador) between 2007 and 2013: Transition from continuous to episodic activity. J Volcanol Geotherm Res 298:1–14. https://doi.org/10.1016/j.jvolgeores.2015.03.022

INECEL (Instituto Ecuatoriano de Electrificación) (1987) Proyecto Hidroeléctrico Coca-Codo Sinclair - Estudios de Factibilidad. Ministerio de Energía y Minería

Instituto Geofísico EPN (2010) Informe de la actividad del volcán El Reventador durante el año 2009. Instituto Geofísico de la Escuela Politécnica Nacional

Instituto Geofísico EPN (2018) Informe Especial N°2 del volcán El Reventador – 2018. Instituto Geofísico de la Escuela Politécnica Nacional

Instituto Geofísico EPN (2019) Informe anual del volcán El Reventador – 2018. Instituto Geofísico de la Escuela Politécnica Nacional

Ishii K, Yokoo A, Kagiyama T, et al (2019) Gas flow dynamics in the conduit of Strombolian explosions inferred from seismo-acoustic observations at Aso volcano, Japan. Earth Planets Space 71:13. https://doi.org/10.1186/s40623-019-0992-z

Jaggar TA (1917a) Thermal gradient of Kilauea Lava Lake. J Wash Acad Sci 7:397–405

Jaggar TA (1917b) Volcanologic investigations at Kilauea. Am J Sci 44:160–220

James MR, Robson S, Pinkerton H, Ball M (2006) Oblique photogrammetry with visible and thermal images of active lava flows. Bull Volcanol 69:105–108. https://doi.org/10.1007/s00445-006-0062-9

Jaupart C, Vergniolle S (1988) Laboratory models of Hawaiian and Strombolian eruptions. Nature 331:58–60. https://doi.org/10.1038/331058a0

Johnson JB, Harris AJL, Sahetapy-Engel STM, et al (2004) Explosion dynamics of pyroclastic eruptions at Santiaguito Volcano: DYNAMICS OF SANTIAGUITO PYROCLASTIC ERUPTIONS. Geophys Res Lett 31:n/a-n/a. https://doi.org/10.1029/2003GL019079

Johnson JB, Lees JM (2000) Plugs and chugs—seismic and acoustic observations of degassing explosions at Karymsky, Russia and Sangay, Ecuador. J Volcanol Geotherm Res 101:67–82. https://doi.org/10.1016/S0377-0273(00)00164-5

Johnson JB, Lees JM, Gerst A, et al (2008) Long-period earthquakes and co-eruptive dome inflation seen with particle image velocimetry. Nature 456:377–381. https://doi.org/10.1038/nature07429

Kelfoun K, Santoso AB, Latchimy T, et al (2021) Growth and collapse of the 2018–2019 lava dome of Merapi volcano. Bull Volcanol 83:8. https://doi.org/10.1007/s00445-020-01428-x

Kelfoun K, Vallejo Vargas S (2015) VolcFlow capabilities and potential development for the simulation of lava flows. Geol Soc Lond Spec Publ. https://doi.org/10.1144/SP426.8

Kern C, Werner C, Elias T, et al (2013) Applying UV cameras for SO2 detection to distant or optically thick volcanic plumes. J Volcanol Geotherm Res 262:80–89. https://doi.org/10.1016/j.jvolgeores.2013.06.009

Kirchhoff G (1860) On the relation between the radiating and absorbing powers of different bodies for light and heat. The London, Edinburg, and Dublin Philosophical Magazine and Journal of Science XX:1–21

Kraus S (2006) DOASIS a framework design for DOAS. PhD Thesis, Technische Informatik, Univ.\ Mannheim

Kuenzer C, Dech S (eds) (2013) Thermal Infrared Remote Sensing: Sensors, Methods, Applications. Springer Netherlands, Dordrecht

Lees JM, Johnson JB, Ruiz M, et al (2008) Reventador Volcano 2005: Eruptive activity inferred from seismo-acoustic observation. J Volcanol Geotherm Res 176:179–190. https://doi.org/10.1016/j.jvolgeores.2007.10.006

Lensky NG, Sparks RSJ, Navon O, Lyakhovsky V (2008) Cyclic activity at Soufrière Hills Volcano, Montserrat: degassing-induced pressurization and stick-slip extrusion. Geol Soc Lond Spec Publ 307:169–188. https://doi.org/10.1144/SP307.10

Lodato L, Spampinato L, Harris AJL, et al (2008) Use of Forward Looking InfraRed thermal cameras at active volcanoes. In: Conception, verification and application of innovative techniques to study active volcanoes. Instituto Nazionale di Geofisica e Vulcanologia, pp 427–434

Lopez T, Thomas HE, Prata AJ, et al (2015) Volcanic plume characteristics determined using an infrared imaging camera. J Volcanol Geotherm Res 300:148–166. https://doi.org/10.1016/j.jvolgeores.2014.12.009

Marchetti E, Ripepe M, Harris AJL, Delle Donne D (2009) Tracing the differences between Vulcanian and Strombolian explosions using infrasonic and thermal radiation energy. Earth Planet Sci Lett 279:273–281. https://doi.org/10.1016/j.epsl.2009.01.004

Mastin LG (1995) Thermodynamics of gas and steam-blast eruptions. Bull Volcanol 57:85–98

Matsushima N (2005) H2O emission rate by the volcanic plume during the 2000-2002 Miyakejima volcanic activity: 2000-2002 MIYAKEJIMA VOLCANIC ACTIVITY. Geophys Res Lett 32:n/a-n/a. https://doi.org/10.1029/2005GL023217

Maxwell JC (1865) A dynamical theory of the electromagnetic field. Philos Trans R Soc Lond 155:459–512. https://doi.org/10.1098/rstl.1865.0008

McGonigle AJS, Pering TD, Wilkes TC, et al (2017) Ultraviolet Imaging of Volcanic Plumes: A New Paradigm in Volcanology. Geosciences 7:68. https://doi.org/10.3390/geosciences7030068

Mercalli G (1907) Vulcani attivi della terra: morfologia–dinamismo–prodotti–distribuzione geografica–cause... Ulrico Hoepli. Editore libraio della Real Casa, Milano

Miwa T, Toramaru A (2013) Conduit process in vulcanian eruptions at Sakurajima volcano, Japan: Inference from comparison of volcanic ash with pressure wave and seismic data. Bull Volcanol 75:685. https://doi.org/10.1007/s00445-012-0685-y

Morrissey M, Masting L (1999) Vulcanian eruptions. In: Encyclopedia of Volcanoes, 1st edn. San Diego, California, USA, pp 463–475

Morton BR, Taylor GIS, Turner JS (1956) Turbulent gravitational convection from maintained and instantaneous sources. Proc R Soc Lond Ser Math Phys Sci 234:1–23

Mothes PA, Ruiz MC, Viracucha EG, et al (2017) Geophysical Footprints of Cotopaxi's Unrest and Minor Eruptions in 2015: An Opportunity to Test Scientific and Community Preparedness. In: Gottsmann J, Neuberg J, Scheu B (eds) Volcanic Unrest : From Science to Society. Springer International Publishing, Cham, pp 241–270

Mothes PA, Yepes HA, Hall ML, et al (2015) The scientific–community interface over the fifteen-year eruptive episode of Tungurahua Volcano, Ecuador. J Appl Volcanol 4:9. https://doi.org/10.1186/s13617-015-0025-y

Moxham RM (1971) Thermal surveillance of volcanoes. UNESCO

Moxham RM, Boynton GR, Cote CE (1972) Satellite telemetry of fumarole temperatures, Mount Rainier, Washington. Bull Volcanol 36:191–199. https://doi.org/10.1007/BF02596990

Naranjo MF, Ebmeier SK, Vallejo S, et al (2016) Mapping and measuring lava volumes from 2002 to 2009 at El Reventador Volcano, Ecuador, from field measurements and satellite remote sensing. J Appl Volcanol 5:8. https://doi.org/10.1186/s13617-016-0048-z

Neuberg J (2000) Characteristics and causes of shallow seismicity in andesite volcanoes. Philos Trans R Soc Lond Ser Math Phys Eng Sci 358:1533–1546. https://doi.org/10.1098/rsta.2000.0602

Newhall CG, Punongbayan RS (1995) Pinatubo! Bull Volcanol 57:147–152. https://doi.org/10.1007/BF00250403

Newhall CG, Self S (1982) The volcanic explosivity index (VEI) an estimate of explosive magnitude for historical volcanism. J Geophys Res 87:1231. https://doi.org/10.1029/JC087iC02p01231

Newton I (1672) A letter of Mr. Isaac Newton, Professor of the Mathematicks in the University of Cambridge; containing his new theory about light and colors: sent by the author to the publisher from Cambridge, Febr. 6. 1671/72; in order to be communicated to the R. Society. Philos Trans R Soc Lond 6:3075–3087. https://doi.org/10.1098/rstl.1671.0072

Oppenheimer C, Yirgu G (2002) Thermal imaging of an active lava lake: Erta 'Ale volcano, Ethiopia. Int J Remote Sens 23:4777–4782. https://doi.org/10.1080/01431160110114637

Ortiz HD, Matoza RS, Garapaty C, et al (2020) Multi-year regional infrasound detection of Tungurahua, El Reventador, and Sangay volcanoes in Ecuador from 2006 to 2013. Acoustics Virtually Everywhere, p 022003

Pailot-Bonnétat S, Harris AJL, Calvari S, et al (2020) Plume Height Time-Series Retrieval Using Shadow in Single Spatial Resolution Satellite Images. Remote Sens 12:3951. https://doi.org/10.3390/rs12233951

Pang GKH, Liu HHS (2001) LED location beacon system based on processing of digital images. IEEE Trans Intell Transp Syst 2:135–150. https://doi.org/10.1109/6979.954547

Parfitt EA, Wilson L (2008) Fundamentals of physical volcanology. Blackwell, Oxford

Parra R, Bernard B, Narváez D, et al (2016) Eruption Source Parameters for forecasting ash dispersion and deposition from vulcanian eruptions at Tungurahua volcano: Insights from field data from

the July 2013 eruption. J Volcanol Geotherm Res 309:1–13. https://doi.org/10.1016/j.jvolgeores.2015.11.001

Patrick MR (2007) Dynamics of Strombolian ash plumes from thermal video: Motion, morphology, and air entrainment. J Geophys Res Solid Earth 112:. https://doi.org/10.1029/2006JB004387

Patrick MR, Hams A, Jonathan Dehn Luke Flynn William Gersch Robert Wright C (2005) Strombolian Eruption Dynamics From Thermal (FLIR) Video Imagery

Patrick MR, Harris AJL, Ripepe M, et al (2007) Strombolian explosive styles and source conditions: insights from thermal (FLIR) video. Bull Volcanol 69:769–784. https://doi.org/10.1007/s00445-006-0107-0

Patrick MR, Orr T, Antolik L, et al (2014) Continuous monitoring of Hawaiian volcanoes with thermal cameras. J Appl Volcanol 3:1. https://doi.org/10.1186/2191-5040-3-1

Patrick MR, Swanson D, Orr T (2016) Automated tracking of lava lake level using thermal images at Kīlauea Volcano, Hawai'i. J Appl Volcanol 5:6. https://doi.org/10.1186/s13617-016-0047-0

Peccerillo A, Taylor SR (1976) Geochemistry of eocene calc-alkaline volcanic rocks from the Kastamonu area, Northern Turkey. Contrib Mineral Petrol 58:63–81. https://doi.org/10.1007/BF00384745

Peters N, Hoffmann A, Barnie T, et al (2015) Use of motion estimation algorithms for improved flux measurements using SO 2 cameras. J Volcanol Geotherm Res 300:58–69. https://doi.org/10.1016/j.jvolgeores.2014.08.031

Planck M, Masius M (1914) The theory of heat radiation. P. Blakiston's son & Co., Philadelphia

Platt U, Lübcke P, Kuhn J, et al (2015) Quantitative imaging of volcanic plumes — Results, needs, and future trends. J Volcanol Geotherm Res 300:7–21. https://doi.org/10.1016/j.jvolgeores.2014.10.006

Platt U, Stutz J (2008) Differential optical absorption spectroscopy: principles and applications ; with 55 tables. Springer, Berlin

Ramon P, Vallejo S, Mothes P, et al (2021) Instituto Geofísico – Escuela Politécnica Nacional, the Ecuadorian Seismology and Volcanology Service. Volcanica 4:93–112. https://doi.org/10.30909/vol.04.S1.93112

Ramsey MS, Harris AJL (2013) Volcanology 2020: How will thermal remote sensing of volcanic surface activity evolve over the next decade? J Volcanol Geotherm Res 249:217–233. https://doi.org/10.1016/j.jvolgeores.2012.05.011

Ripepe M, Bonadonna C, Folch A, et al (2013) Ash-plume dynamics and eruption source parameters by infrasound and thermal imagery: The 2010 Eyjafjallajökull eruption. Earth Planet Sci Lett 366:112–121. https://doi.org/10.1016/j.epsl.2013.02.005

Ripepe M, Harris AJL, Marchetti E (2005) Coupled thermal oscillations in explosive activity at different craters of Stromboli volcano: COUPLED THERMAL OSCILLATIONS AT DIFFERENT CRATERS. Geophys Res Lett 32:. https://doi.org/10.1029/2005GL022711

Sahetapy-Engel ST, Harris AJL (2009) Thermal-image-derived dynamics of vertical ash plumes at Santiaguito volcano, Guatemala. Bull Volcanol 71:827–830. https://doi.org/10.1007/s00445-009-0284-8

Sahetapy-Engel ST, Harris AJL, Marchetti E (2008) Thermal, seismic and infrasound observations of persistent explosive activity and conduit dynamics at Santiaguito lava dome, Guatemala. J Volcanol Geotherm Res 173:1–14. https://doi.org/10.1016/j.jvolgeores.2007.11.026

Saltykovskii AYa (2012) The eruption of Eyjafjallajökull (Iceland) in Spring 2010 and its possible consequences. Izv Atmospheric Ocean Phys 48:683–695. https://doi.org/10.1134/S0001433812070067

Samaniego P, Eissen J-P, Le Pennec J-L, et al (2008) Pre-eruptive physical conditions of El Reventador volcano (Ecuador) inferred from the petrology of the 2002 and 2004–05 eruptions. J Volcanol Geotherm Res 176:82–93. https://doi.org/10.1016/j.jvolgeores.2008.03.004

Scollo S, Prestifilippo M, Pecora E, et al (2014) Eruption column height estimation of the 2011-2013 Etna lava fountains. Ann Geophys 57:3. https://doi.org/10.4401/ag-6396

Self S, Wilson L, Nairn IA (1979) Vulcanian eruption mechanisms. Nature 277:440–443. https://doi.org/10.1038/277440a0

Shinohara H (2005) Volcanic gases emitted during mild Strombolian activity of Villarrica volcano, Chile. Geophys Res Lett 32:L20308. https://doi.org/10.1029/2005GL024131

Siebert L, Simkin T, Kimberly P (2011) Volcanoes of the World: Third Edition. University of California Press

Spampinato L, Calvari S, Oppenheimer C, Boschi E (2011) Volcano surveillance using infrared cameras. Earth-Sci Rev 106:63–91. https://doi.org/10.1016/j.earscirev.2011.01.003

Sparks RSJ (1986) The dimensions and dynamics of volcanic eruption columns. Bull Volcanol 48:3–15. https://doi.org/10.1007/BF01073509

Sparks RSJ (1997) Causes and consequences of pressurisation in lava dome eruptions. Earth Planet Sci Lett 150:177–189. https://doi.org/10.1016/S0012-821X(97)00109-X

Sparks RSJ, Bursik MI, Ablay GJ, et al (1992) Sedimentation of tephra by volcanic plumes. Part 2: controls on thickness and grain-size variations of tephra fall deposits. Bull Volcanol 54:685–695. https://doi.org/10.1007/BF00430779

Stone J, Barclay J, Simmons P, et al (2014) Risk reduction through community-based monitoring: the vigías of Tungurahua, Ecuador. J Appl Volcanol 3:11. https://doi.org/10.1186/s13617-014-0011-9

Thivet S, Harris AJL, Gurioli L, et al (2021) Multi-Parametric Field Experiment Links Explosive Activity and Persistent Degassing at Stromboli. Front Earth Sci 9:669661. https://doi.org/10.3389/feart.2021.669661

Thornber CR (1997) HVO/RTVS-1: A prototype remote video telemetry system for monitoring the Kilauea East Rift Zone eruption. USGS

Valade SA, Harris AJL, Cerminara M (2014) Plume Ascent Tracker: Interactive Matlab software for analysis of ascending plumes in image data. Comput Geosci 66:132–144. https://doi.org/10.1016/j.cageo.2013.12.015

Vallejo Vargas S, Hernandez S, Battaglia J, et al (2019) Partial summit collapse at El Reventador volcano (Ecuador) and its subsequent activity observed in thermal imaging, seismo-acoustic signals and SO2 degasification. In: AGU Fall Meeting Abstracts

Voigt S, Orphal J, Bogumil K, Burrows JP (2001) The temperature dependence (203–293 K) of the absorption cross sections of O3 in the 230–850 nm region measured by Fourier-transform spectroscopy. J Photochem Photobiol Chem 143:1–9. https://doi.org/10.1016/S1010-6030(01)00480-4

Weill A, Brandeis G, Vergniolle S, et al (1992) Acoustic sounder measurements of the vertical velocity of volcanic jets at Stromboli Volcano. Geophys Res Lett 19:2357–2360. https://doi.org/10.1029/92GL02502

Weiser P, Liebe O, Mähler A, et al (2021) AnyDesk

Williams DB, Ramsey MS (2019) On the Applicability of Laboratory Thermal Infrared Emissivity Spectra for Deconvolving Satellite Data of Opaque Volcanic Ash Plumes. Remote Sens 11:2318. https://doi.org/10.3390/rs11192318

Wilson L (1976) Explosive Volcanic Eruptions--III. Plinian Eruption Columns. Geophys J Int 45:543–556. https://doi.org/10.1111/j.1365-246X.1976.tb06909.x

Wilson L (1980) Relationships between pressure, volatile content and ejecta velocity in three types of volcanic explosions. J Volcanol Geotherm Res 8:297–313. https://doi.org/10.1016/0377-0273

Wilson L, Self S (1980) Volcanic explosion clouds: Density, temperature, and particle content estimates from cloud motion. J Geophys Res 85:2567. https://doi.org/10.1029/JB085iB05p02567

Wilson L, Sparks RSJ, Huang TC, Watkins ND (1978) The control of volcanic column heights by eruption energetics and dynamics. J Geophys Res Solid Earth 83:1829–1836. https://doi.org/10.1029/jb083ib04p01829

Wilson L, Walker GPL (1987) Explosive volcanic eruptions - VI. Ejecta dispersal in plinian eruptions: the control of eruption conditions and atmospheric properties. Geophys J Int 89:657–679. https://doi.org/10.1111/j.1365-246X.1987.tb05186.x

Wood K, Thomas H, Watson M, et al (2019) Measurement of three dimensional volcanic plume properties using multiple ground based infrared cameras. ISPRS J Photogramm Remote Sens 154:163–175. https://doi.org/10.1016/j.isprsjprs.2019.06.002

Woods AW (1988) The fluid dynamics and thermodynamics of eruption columns. Bull Volcanol 50:169–193. https://doi.org/10.1007/BF01079681

Woods AW (1995a) A model of vulcanian explosions. Nucl Eng Des 155:345–357. https://doi.org/10.1016/0029-5493(94)00881-X

Woods AW (1995b) The dynamics of explosive volcanic eruptions. Rev Geophys 33:495–530. https://doi.org/10.1029/95RG02096

Woods AW, Bower SM (1995) The decompression of volcanic jets in a crater during explosive volcanic eruptions. Earth Planet Sci Lett 131:189–205. https://doi.org/10.1016/0012-821X(95)00012-2

Yokoo A (2009) Continuous thermal monitoring of the 2008 eruptions at Showa crater of Sakurajima volcano, Japan. Earth Planets Space 61:1345–1350. https://doi.org/10.1186/BF03352987

Zettwoog P, Tazieff H (1972) Instrumentation for measuring and recording mass and energy transfer from volcanoes to atmosphere. Bull Volcanol 36:1–19. https://doi.org/10.1007/BF02596979

Zies EG (1941) Temperatures of volcanoes, fumaroles, and hotsprings. In: Temperature: Its Measurement and Control inScience and Industry. Reinhold Publishing Corporation, New York, pp 372–380